Title
NONLINEAR OPTICAL EFFECTS IN LIQUID CRYSTALS

Author
Hanson, Eric Gregory.

Publication Date
1976-12-01

LBL-6022
c. 1

NONLINEAR OPTICAL EFFECTS IN LIQUID CRYSTALS

Eric Gregory Hanson
(Ph. D. thesis)

December 1976

Prepared for the U. S. Energy Research and
Development Administration under Contract W-7405-ENG-48

NONLINEAR OPTICAL EFFECTS IN LIQUID CRYSTALS

Eric Gregory Hanson

ABSTRACT

We show that various characteristic parameters of nematic liquid crystals can be determined by a combination of linear and nonlinear optical measurements. We have made such measurements on seven homologous compounds of the p,p'-di-n-alkoxy-azoxybenzene series, allowing us to determine the variations in these parameters with increasing alkyl chain length.

In the isotropic phase, we measured the temperature dependence of the optical Kerr constant and the orientational relaxation time. The critical behavior near the nematic-isotropic transition agrees well with the predictions from the Landau-de Gennes model. We have deduced the expansion coefficients of the three lowest order terms in the Landau free energy. Knowing these coefficients, we show that the Landau expansion converges quickly in the isotropic phase, but in the nematic phase it either diverges or converges slowly. In addition, these results suggest that the mean-field theory of Maier and Saupe is not a good approximation for a quantitative description of the isotropic-nematic transition.

In the nematic phase, we have measured the temperature dependence of the refractive indices and linear birefringence of the same seven compounds. Using the Vuks' model of local field corrections, we have deduced from our results both the microscopic and the macroscopic order parameters. The former agree well with those determined by Pines et al. from NMR measurements. We show that increasing alkyl chain length increases the average molecular polarizability much faster than the polar-

izability anisotropy. Our results clearly show that the alkyl chains do contribute to the polarizability anisotropy, but the dominant contribution is from the molecular core.

We also show that it is possible to use a single liquid crystalline material in its isotropic phase to study the entire range of self-focusing behavior from transient to quasi-steady-state. We have performed such a study using a single input laser with a constant pulse length, by varying the orientational relaxation time of p-ethoxybenzylidene-p-butylaniline (EBBA) as a function of temperature. Our results agree well with a simple unified physical description of self-focusing and with known theoretical predictions. Stimulated Brillouin scattering in the backward direction is identified as the mechanism responsible for the limiting diameter of the self-focused beam in our experiment.

NONLINEAR OPTICAL EFFECTS IN LIQUID CRYSTALS

Contents

Appendices

I. INTRODUCTION

Nematic liquid crystals are fascinating materials with distinctive properties unlike those of other forms of condensed matter.[1] These materials are composed of long, rigid, organic molecules. Each molecule has a highly anisotropic polarizability, causing the orientation of neighboring molecules to be strongly coupled together by dispersion or Van der Waals forces. As a result of this coupling, these materials posess an unusual phase, the nematic phase, which occurs in a temperature range between the solid and the liquid phases. In the nematic phase, the molecules move around freely but always remain roughly parallel to each other. The material is birefringent because of the anisotropic polarizability of the individual molecules.

As the material is heated, it makes an abrupt phase transition into the isotropic liquid phase. This transition is interesting because of its simplicity. Only one degree of freedom changes during this transition, that of orientational ordering.[2] In order to learn about this phase transition, we perturbed the isotropic liquid to cause a small amount of orientational ordering. The perturbation was from the optical frequency electric field produced by a pulsed laser, which coupled to the induced dipole moments on the molecules and produced the ordering. We probed the response of the material by measuring the resulting birefringence, or in other words, by measuring the optical Kerr constant B[3]. We also measured the decay of the birefringeance after the strong laser pulse was over. From this we could deduce the orientational relaxation time τ. In Chapter II, we discuss the results of these measurements for seven closely related nematic compounds. We find that the optical Kerr constants and the relaxation times are strongly temperature-dependent, in agreement with the Landau-deGennes model. As with other liquid crystalline materials, these compounds have a large B and a long τ, because of the strong orientational coupling between the molecules.[3] We show that we can deduce characteristic parameters of the nematic-isotropic phase transitions in these materials, and we see how these parameters vary with increasing molecular length. Using these parameters, we estimate the latent heat of the nematic-isotropic phase transition ΔH, and compare this to the calorimetrically determined ΔH.[4] We find good agreement for the lower members of the series, but substantial deviation for the highest two members.

In the nematic phase, the large optical birefringence is the basis of many applications such as liquid crystal displays. The magnitude of this birefringence is determined by the molecular optical anisotropy and the degree of orientational ordering, both of which are strongly affected by the molecular structure.[5] Recent work using nuclear magnetic resonance techniques has investigated some effects of changing molecular structure upon the orientational order paramter.[6] These measurements showed the effects of increasing alkyl chain length by studying a homologous series of nematics. However, no measurements have yet been reported on the variation of the optical anisotropy or of the resulting birefringence as a function of chain length.

In Chapter III, we show that the optical refractive indices and birefringence can be measured to an accuracy of 0.5% as a function of temperature. We present the results of these measurements for seven members of the same homologous series as discussed in Chapter II. We deduce the microscopic order parameters, which agree well with those determined by

Pines et al.[6] We find that the macroscopic polarizability anisotropy decreases strongly with increasing chain length due to the molecular volume effect. The microscopic polarizability anisotropy of the individual molecules actually increases slightly with increasing chain length. This shows that the end chains do contribute to the anisotropy, but their contribution is always much less than that of the molecular core.

The field-induced refractive index of a liquid crystal can lead to self-focusing of an optical beam.[7] Previous quantitative experiments on self-focusing have investigated only two limiting cases: the case of extreme transient self-focusing[8] and the case of quasi-steady-state self-focusing.[9] In the nematic liquid crystal it is possible to investigate both of these limiting cases as well as the intermediate range between them simply by varying the sample temperature. In Chapter IV, we describe the results of measurements using a Q-switched laser pulse with a conventional detection system, where we vary the relaxation time of the liquid crystal over the entire range with only one sample. We show that our results can be explained in terms of a simple unified physical model. In the quasi-steady-state limit, the focusing behavior approaches that predicted for the moving focal spot model, while in the transient limit the behavior agrees with that predicted for the dynamic trapping model. We can also identify backward stimulated Brillouin scattering as the mechanism responsible for the limiting diameter in our measurements.

References

1. See, for example, P. G. de Gennes, "Physics of Liquid Crystals", Clarendon Press, Oxford (1974).
2. P. G. de Gennes, Phys. Lett. A30, 454 (1969) and Mol. Cryst. Liq. Cryst. 12, 193 (1971).
3. G. K. L. Wong and Y. R. Shen, Phys. Rev. Lett. 30, 895 (1973) and Phys. Rev. A10, 1277 (1974).
4. H. Arnold, Z. Phys. Chem. Leipzig 226, 146 (1964).
5. I. Haller, Progress in Solid State Chemistry 10, 103 (1975).
6. A. Pines, D. I. Ruben, and S. Allison, Phys. Rev. Lett. 33, 1002 (1974).
7. See, for example, Y. R. Shen, Prog. Quant. Elect. 4, 1 (1975); J. H. Marburger, Prog. Quant. Elect. 4, 35 (1975).
8. G. K. L. Wong and Y. R. Shen, Phys. Rev. Lett. 32, 527 (1974).
9. M. M. T. Loy and Y. R. Shen, Phys. Rev. Lett. 22, 994 (1969), 25, 1333 (1970) and IEEE J. Quant. Electron. 9, 409 (1973).

II. OPTICAL-FIELD-INDUCED REFRACTIVE INDICES AND ORIENTATIONAL RELAXATION TIMES IN A HOMOLOGOUS SERIES OF ISOTROPIC NEMATIC SUBSTANCES

1. INTRODUCTION

Recently, it has been demonstrated by nonlinear optical measurements that liquid crystalline materials in their isotropic phase can have a large optical Kerr constant with a long relaxation time.[1] Such characteristics result from the pretransitional behavior of the materials. The nonlinear optical measurements actually provide a stringent test on the Landau-de Gennes phase transition model for liquid cyrstals. From these measurements together with measurements on the order parameter and anisotropy in refractive indices, one can obtain values for large number of characteristic material parameters: T^*, the fictitous second-order isotropic-nematic transition temperature; ν, the viscosity coefficient for molecular orientation; a, b, and d, the coefficients in the Landau's series expansion of the free energy; and others. These parameters are important for characterizing a liquid crystalline material. To understand how molecular structure affects the properties of liquid crystals, it will then be of great interest to find these parameters for a homologous series of compounds. However, no such information for any homologous series exists in the literature.

In this chapter, we report the results of our recent nonlinear refractive index measurements on the homologous compounds of p,p'-di-n-alkoxy-azoxybenzenes. The molecular structures of these compounds are shown in Table I. Also listed in the Table are the isotropic-nematic transition temperatures T_K of our samples, the macroscopic order parameters Q_K at T_K, the refractive index anisotropies $\Delta\chi$ (defined for the case of perfect molecular alignment) we recently measured, and the latent heats ΔH obtained from Ref. 2. From the nonlinear optical measurements and the values of T_K, Q_K, and $\Delta\chi$, we then deduce the various characteristic parameters we mentioned earlier for these homologous compounds. The work here constitutes one of the very few examples where nonlinear optical measurements can yield quantitative results not only on nonlinear optical coefficients but also on other characteristic parameters of a condensed matter.

In Sec. 2, we give a brief review on the theory of optical field-induced refractive indices. We describe in Sec. 3, the experimental arrangement and the data analysis procedure. Then, in Sec. 4, we present the experimental results and the material parameters deduced from our results. Finally, Sec. 5 discusses the implications of our results from the molecular structural view point.

2. THEORETICAL BACKGROUND

Liquid crystalline materials are composed of highly anisotropic molecules. Consequently, the induced dipoles on the molecules are also highly anisotropic. In the presence of intense optical field, the molecules tend to be aligned by the field via induced dipole interaction with the field. The resultant molecular ordering is then reflected by the induced optical anisotropy in the medium.

If Q is a macroscopic tensorial order parameter which describes the degree of molecular alignment, then the optical susceptibility χ_{ij} (or any tensorial property of the medium) can be written as[3]

$$\chi_{ij} = \bar{\chi}\,\delta_{ij} + \frac{2}{3}\Delta\chi\, Q_{ij} \qquad (1)$$

where $\overline{\chi} = \frac{1}{3}\,\Sigma_i\chi_i$ and $\Delta\chi$ is the anisotropy in χ_{ij} with perfect molecular alignment such that $\frac{1}{2}Q_{xx} = -Q_{yy} = -Q_{zz} = 1$. In the absence of field, in an isotropic medium, Q_{ij} is zero, but becomes finite in the presence of a field. According to the Landau-de Gennes model,[2] the free energy per unit volume of an isotropic fluid in the presence of an intense field $\vec{E}(\omega)$ and a weak probing field $\vec{E}(\omega')$ is given by

$$F = F_o + \frac{1}{2}a(T - T^*)Q_{ij}Q_{jk} + \frac{1}{3}bQ_{ij}Q_{jk}Q_{ki} + \frac{1}{4}dQ_{ij}Q_{jk}Q_{kl}Q_{li}$$

$$- \frac{1}{4}\chi_{ij}(\omega)E_i^*(\omega)E_j(\omega) - \frac{1}{4}\chi_{ij}(\omega')E_i^*(\omega')E_j(\omega') \qquad (2)$$

where F_o is independent of Q and where we assume $(1/|\omega - \omega'|)$ is much shorter than the response time of Q (see Appendix I). The field-induced molecular ordering then obeys the dynamic equation[3] $\nu\partial Q_{ij}/\partial t = -\,\partial F/\partial Q_{ji}$. Normally, Q is small in the isotropic phase, and hence the Q^3 and Q^4 terms and the $\chi_{ij}(\omega')E_i^*(\omega')E_j(\omega')$ term in Eq. (2) are often negligible. The dynamic equation assumes the form

$$\nu\,\frac{\partial Q_{ij}}{\partial t} + a(T - T^*)Q_{ij} = f_{ij}(t)$$

$$f_{ij}(t) = \frac{1}{12}\Delta\chi\left(E_i^*(\omega,t)E_j(\omega,t) - \frac{1}{3}|E(\omega,t)|^2\delta_{ij}\right) + \text{c. c.} \qquad (3)$$

under the condition that $|\omega - \omega'| >> 1/\tau = a(T - T^*)/\nu$.

Consider first the steady-state solution of Eq. (3). If the optical field propagating along $\hat{z}$ is linearly polarized, e.g., $\vec{E} = E\hat{x}$, we find immediately

$$Q_{xx} = -2\,Q_{yy} = \frac{1}{9}\Delta\chi(\omega)\,|E(\omega)|^2/a(T - T^*). \tag{4}$$

The corresponding induced linear birefringence at ω' is

$$\begin{aligned}\delta n_\ell(\omega') &= (2\pi/n)\frac{2}{3}\Delta\chi(\omega')(Q_{xx} - Q_{yy}) \\ &= (2\pi/n)\;\Delta\chi(\omega)\;\Delta\chi(\omega')\;|E(\omega)|^2/9a(T - T^*)\end{aligned} \tag{5}$$

where n is the linear refractive index and we assume $|\omega - \omega'| >> 1/\tau$. From the usual definition of the optical Kerr constant $B = \omega'\delta n_\ell/\pi c|E(\omega)|^2$, we have

$$B = 2(\omega/nc)\;\Delta\chi(\omega)\;\Delta\chi(\omega')/9a(T - T^*). \tag{6}$$

If the intense optical field is elliptically polarized, e.g., $\vec{E}(\omega) = \hat{e}_+E_+ + \hat{e}_-E_-$ with $\hat{e}_\pm = (\hat{x} \pm i\hat{y})/\sqrt{2}$, we find from Eqs. (1) and (3) the following susceptibility tensor in the circular coordinates for $\omega = \omega'$

$$\begin{aligned}&\frac{1}{2}\begin{pmatrix}\chi_{xx} + \chi_{yy} + i(\chi_{xy} - \chi_{yx}), & (\chi_{xx} - \chi_{yy}) - i(\chi_{xy} + \chi_{yx}) \\ (\chi_{xx} - \chi_{yy}) + i(\chi_{xy} + \chi_{yx}), & \chi_{xx} + \chi_{yy} - i(\chi_{xy} - \chi_{yx})\end{pmatrix} \\ &= \bar{\chi}\,\delta_{ij} + \frac{(\Delta\chi)^2}{18a(T - T^*)}\begin{pmatrix}\frac{1}{3}|E_+|^2 + \frac{1}{3}|E_-|^2 & 2E_-^*E_+ \\ 2E_-E_+^* & \frac{1}{3}|E_+|^2 + \frac{1}{3}|E_-|^2\end{pmatrix}.\end{aligned} \tag{7}$$

We can write

$$\chi_{ij}(\omega)E_i^*(\omega)E_j(\omega) = \bar{\chi}|E(\omega)|^2 + \delta\chi_+|E_+(\omega)|^2 + \delta\chi_-|E_-(\omega)|^2 \cdot$$

$$\delta\chi_\pm = [(\Delta\chi)^2/18a(T - T^*)] \left(+ \frac{1}{3}|E_\pm(\omega)|^2 + \frac{7}{3}|E_\mp(\omega)|^2\right) \qquad (8)$$

and then the field-induced refractive indices seen by the two circular components of the incoming elliptically polarized light are

$$\delta n_\pm(\omega) = (2\pi/n)\delta\chi_\pm(\omega). \qquad (9)$$

The corresponding circular birefringence is

$$\begin{aligned} \delta n_c &= \delta n_- - \delta n_+ \\ &= (2\pi/n)[(\Delta\chi)^2/9a(T - T^*)]\ [|\hat{e}_+ \cdot \vec{E}(\omega)|^2 - |\hat{e}_- \cdot \vec{E}(\omega)|^2]. \end{aligned} \qquad (10)$$

We shall see later that the above-mentioned induced linear and circular birefringences can be deduced from measurements of phase shifts of linear and the elliptical polarizations respectively. As seen in the above expressions, all these field-induced refractive indices and birefringences diverge as T approaches T^*. This critically divergent behavior is of course characteristic of a pretransitional phenomenon. In liquid crystalline materials, the first-order transition temperature T_K (> T^*) always sets in before T reaches T^*.

In nonlinear optics, the field induced refractive indices can be described more generally from symmetry considerations.[4,5] For an isotropic medium, the third-order nonlinear polarization takes the form

$$\begin{aligned} P_i^{(3)}(\omega') = \sum_j D\Big[&\chi^{(3)}_{1122}(\omega' = \omega' + \omega - \omega)E_i(\omega')E_j(\omega)E_j^*(\omega) \\ &+ \chi^{(3)}_{1212}(\omega' = \omega' + \omega - \omega)E_j(\omega')E_i(\omega)E_j^*(\omega) \qquad (11) \\ &+ \chi^{(3)}_{1221}(\omega' = \omega' + \omega - \omega)E_j(\omega')E_j(\omega)E_i^*(\omega)\Big] \end{aligned}$$

where $\chi^{(3)}$'s are components of the third-order nonlinear susceptibility tensor and where D is a degeneracy factor[4], which accounts for the equivalent permutations of the frequency indices. For these field induced refractive indices, $D = 6$ if $\omega \neq \omega'$, while $D = 3$ if $\omega = \omega'$. Of course, there is no factor of 2 jump in the observed nonlinear refractive indices as ω approaches ω'. Instead, these quantities have a smooth frequency dependence (see Appendix I). The tensor elements of $\chi^{(3)}$ are <u>not</u> frequency-independent, but as ω approaches ω', they vary smoothly (see Appendix I).

In general, for $\vec{E}(\omega) = \hat{x}\, E(\omega)$, we can solve Eq. (11) to give

$$\begin{aligned} \delta n_{xx}(\omega') &= (2\pi/n)P_x^{(3)}(\omega')/E_x(\omega') \\ &= (2\pi/n)6\Big[\chi^{(3)}_{1122} + \chi^{(3)}_{1212} + \chi^{(3)}_{1221}\Big]|E(\omega)|^2 \\ & \qquad\qquad (12) \\ \delta n_{yy}(\omega') &= (2\pi/n)P_y^{(3)}(\omega')/E_y(\omega') \\ &= (2\pi/n)6\chi^{(3)}_{1122}|E(\omega)|^2 . \end{aligned}$$

Comparing Eq. (12) with Eqs. (4), (5), and (6), we find, assuming $\Delta\chi(\omega) = \Delta\chi(\omega')$ and $|\omega - \omega'| >> 1/\tau$,

$$\chi^{(3)}_{1122}(|\omega - \omega'| \gg 1/\tau) = -\frac{1}{3}\,\frac{1}{6}\left[\frac{(\Delta\chi)^2}{9a(T - T^*)}\right] = -\frac{1}{3}\,\frac{1}{12}\,\frac{nc}{\omega}\,B$$

$$\chi^{(3)}_{1212}(|\omega - \omega'| \gg 1/\tau) + \chi^{(3)}_{1221}(|\omega - \omega'| \gg 1/\tau) = \frac{1}{6}\left[\frac{(\Delta\chi)^2}{9a(T - T^*)}\right]$$

$$= \frac{1}{12}\,\frac{nc}{\omega}\,B. \tag{13a}$$

This gives, for $|\omega - \omega'| \gg 1/\tau$,

$$-3\chi^{(3)}_{1122}(|\omega - \omega'| \gg 1/\tau) = \chi^{(3)}_{1212}(|\omega - \omega'| \gg 1/\tau) + \chi^{(3)}_{1221}(|\omega - \omega'| \gg 1/\tau). \tag{13b}$$

For $\omega = \omega'$, and for $\vec{E} = \hat{e}_+E_+(\omega) + \hat{e}_-E_-(\omega)$, we have in circular coordinates,

$$\begin{aligned}
\delta n_\pm &= (2\pi/n)P^{(2)}_\pm(\omega)/E_\pm(\omega)\\
&= (2\pi/n)3\Big[\Big(\chi^{(3)}_{1122}(\omega = \omega') + \chi^{(3)}_{1212}(\omega = \omega')\Big)|E_\pm(\omega)|^2\\
&\qquad + \Big(\chi^{(3)}_{1122}(\omega = \omega') + \chi^{(3)}_{1212}(\omega = \omega')\\
&\qquad + 2\chi^{(3)}_{1221}(\omega = \omega')\Big)|E_\mp(\omega)|^2\Big]
\end{aligned} \tag{14}$$

$$\delta n_c = (2\pi/n)6\chi^{(3)}_{1221}\Big[|\hat{e}_+{}^\dagger \cdot \vec{E}(\omega)|^2 - |\hat{e}_-{}^\dagger \cdot \vec{E}(\omega)|^2\Big].$$

Comparing Eq. (14) with the previous expressions, we find,

$$\chi^{(3)}_{1221}(\omega = \omega') = \frac{1}{6}\left[(\Delta\chi)^2/9a(T - T^*)\right] = \frac{1}{12}\frac{nc}{\omega}B$$
$$= 3\left(\chi^{(3)}_{1122}(\omega = \omega') + \chi^{(3)}_{1212}(\omega = \omega')\right). \qquad (15)$$

Also, from the symmetry of Eq. (11), $\chi^{(3)}_{1122}(\omega = \omega') = \chi^{(3)}_{1212}(\omega = \omega')$.

Owyoung et al. have shown that with only nuclear contribution, the third-order nonlinear polarization can be written as[6]

$$P_i^{(3)}(\omega') = \frac{2\alpha}{4} E_i(\omega')E_j(\omega)E_j^*(\omega) + \frac{\beta}{4} E_j(\omega')E_j(\omega)E_i^*(\omega) + \frac{\beta}{4} E_j(\omega')E_i(\omega)E_j^*(\omega)$$
$$P_i^{(3)}(\omega) = \frac{\beta + 2\alpha}{8} E_i(\omega)E_j(\omega)E_j^*(\omega) + \frac{\beta}{4} E_j(\omega)E_j(\omega)E_i^*(\omega) + \frac{\beta + 2\alpha}{8} E_j(\omega)E_i(\omega)E_j^*(\omega) \qquad (16)$$

where again we assume $|\omega - \omega'| >> 1/\tau$. In the case of liquid crystalline materials, this is true since the electronic contribution is negligible compared to the nuclear part. Comparing Eqs. (13), (15), and (16), we obtain

$$\beta = 2[(\Delta\chi)^2/9a(T - T^*)] = -3\alpha$$
$$B = (\omega/nc)\beta. \qquad (17)$$

We now consider the transient case where molecular ordering Q_{ij} is induced by an intense light pulse. From Eq. (3), we find immediately[1]

$$Q_{ij}(t) = \int_{-\infty}^{t} [f_{ij}(t')/\nu]e^{-(t - t')/\tau}, \qquad (18)$$

where the orientational relaxation time is defined as

$$\tau = \nu/a(T - T^*). \tag{19}$$

Consequently, we have

$$\delta n_\ell(t) = (\pi c/\omega)B\,\frac{1}{\tau}\int_{-\infty}^{t}|E|^2(t')e^{-(t - t')/\tau}dt'$$

$$\delta n_c(t) = (\pi c/\omega)B\,\frac{1}{\tau}\int_{-\infty}^{t}(|\hat{e}_+ \cdot \vec{E}|^2 - |\hat{e}_- \cdot \vec{E}|^2)(t')e^{-(t - t')/\tau}dt'. \tag{20}$$

Thus, knowing the time variation of $\delta n_\ell(t)$ or $\delta n_c(t)$, we should be able to deduce the values of B and τ. Equation (19) shows that τ would diverge as T approaches T^*. This critical slowing-down behavior is again characteristic of a pretransitional phenomenon.

Suppose we have obtained B and τ as functions of temperature T. Then from Eqs. (15) and (19), we can deduce the parameters T^*, $(\Delta\chi)^2/a$, and ν/a. If, in addition, $\Delta\chi$ is separately measured, then a and hence ν are also known. Now, the Landau-de Gennes model with the free-energy expression of Eq. (2) predicts[7] a first-order phase transition at $T_K = T^* + 50b^2/243ad$ and an order parameter $Q_K = 20b/27d$ at the transition. Knowing T_K, T^*, a, and Q_K, we can then deduce b and d.

$$b = 18a(T_K - T^*)/5Q_K$$

$$d = 8a(T_K - T^*)/3Q_K^2. \tag{21}$$

The validity of Eq. (21) however depends on whether the Landau model gives a valid description of the isotropic-nematic transition.

3. EXPERIMENTAL ARRANGEMENT AND DATA ANALYSIS

A. Sample Preparation.,

Our experimental work was on seven homologous compounds of p,p'-di-n-alkoxy-azoxybenzenes. ($C_NH_{2N+1}O-C_6H_4-N_2O-C_6H_4-OC_NH_{2N+1}$ with N-1,2,---,7). The samples were purchased from Eastman Kodak Co. Purification of the samples was done by recrystalization from a saturated solution in various solvents (see Table II). The recrystallized sample was then placed in a pyrex optical cell 2.5 cm long with strain-free windows, and evacuated for several hours to remove atmospheric H_2O and O_2 and the residual solvent. After evacuation, the sample cell was sealed under vacuum. A sample prepared this way was very homogeneous and had a sharp isotropic-nematic transition. The transition temperature was constant to within 0.1°K for more than one month.

There was apparently a small amount of impurities in our samples as evidenced by the lower transition temperatures than those reported for pure samples in the literatures. The differences were typically less than 5°K, suggesting an impurity concentration less than 1%. It appears that with such small impurity concentrations $(T_K - T^*)$ remains nearly unchanged. The temperature-dependent pretransitional properties as a function of $(T - T^*)$ should also remain unchanged and the material parameters deduced from our experiments should be insensitive to impurity contamination.[7]

During our optical measurements, the sample cell was placed in an oven with thermal control. The sample temperature was stablized to within 0.1°K and its uniformity throughout the cell was better than 0.2°K.

B. Experimental Techniques

We obtained the orientational relaxation time τ from the measurements of the transient optical Kerr effect, using a 1 nsec long pulse from a weakly mode-locked ruby laser (see Appendix II). It was necessary to use a pulse that was this short, because the orientational relaxation time τ can be as short as a few nsec for these homologous compounds. A single pulse of ~ 20 KW was switched out of the mode-locked train using a Pockels shutter driven by a laser-triggered spark gap (see Appendix II). This pulse was linearly polarized by P - 1 (see Fig. 1a), and passed through the sample. The resulting molecular ordering was probed by a 10 mW CW He-Ne laser. It passed through a crossed polarizer (P - 2) and analyzer (P - 3), whose axes were oriented at 45° to that of the ruby polarizer (P - 1). Ruby-induced molecular ordering in the sample resulted in a birefringence, causing some of the He-Ne light to pass through the analyzer (P - 3). The time-dependence of this transmission was measured by photomultiplier D - 2. In order to prevent the intense ruby light from reaching D - 2, a diffraction grating, spatial filter, and interference filter were used. This allowed the detection of birefringence in the sample as small as 1 part in 10^6. In order to avoid any possible thermal lensing effect in the sample caused by absorption of He-Ne laser light, an electrically pulsed Pockels cell blocked the He-Ne beam until just before the ruby pulse.

We obtained the nonlinear refractive index or optical Kerr constant from measurements of intensity-dependent ellipse rotation,[4] using a single-mode Q-switched ruby laser (see Fig. 1b). It had a pulsewidth of ~ 12 nsec and a peak power of ~ 100 KW. This was monitored with detector D - 1. The light entered the Fresnel rhomb R - 1 with its $\vec{E}$ field oriented at an angle of 22.5° to the fast axis, so that it emerged elliptically polarized. It was then focused at the center of the sample cell, so that the length of the focal region was appreciably smaller than the cell length. The rhomb R2 was adjusted to give a phase shift opposite to that of R1. With the laser beam strongly attenuated at F - 1 to make ellipse rotation negligible, the analyzer P - 2 was crossed with the polarizer P - 1. Then the laser power was increased by removing filters from the stack F - 1. The intensity dependent rotation of the elliptical polarization was then measured by the signal at photodiode D - 2.

C. Data Analysis

In our optical Kerr measurements, the signal detected was the He-Ne laser light transmitted through the sample between crossed polarizers. The signal S^{OK} was therefore proportional to $\sin^2(\omega'\delta n_\ell \ell/2c)$ where ℓ is the sample length. The linear birefringence δn_ℓ was induced by a laser pulse according to Eq. (20). In our case, $\delta n_\ell \ell \ll 1$, and hence we have

$$S^{OK}(t) \propto \left[B \int_{-\infty}^{t} |E(t')|^2 e^{-(t - t')/\tau} dt'\right]^2 \qquad (22)$$

where $|E(t)|^2$ is the exciting laser pulse. The above equation shows that if the laser pulsewidth is smaller than or comparable with τ, then at sufficiently large t, the signal $S^{OK}(t)$ should decay exponentially as $\exp(-2t/\tau)$. This was indeed the case in our measurements. From the exponential tail, we could deduce the relaxation time τ. In principle, since the exciting pulse $|E(t)|^2$ is known from the oscilloscope trace, we should be able to deduce not only τ but also the optical Kerr constant B from the signal $S^{OK}(t)$. However, in the present case, the probing He-Ne laser beam was too weak to yield good signal-to-noise ratio for an accurate determination of B. We therefore used intensity dependent ellipse rotation measurements instead to determine B.

For an infinite plane wave, the intensity-dependent ellipse rotation θ across the cell is given by[1,4,6]

$$\theta = (\omega/2c)\delta n_c \ell. \tag{23}$$

For a focused beam, however, θ is a function of radius r. In our experiment, the laser pulse oscillated in a single transverse mode, and had a Gaussian profile. We knew this because self focusing experiments done with this same laser consistently showed the formation of only a single focal spot. Our laser pulse had an extremely smooth, nearly Gaussian time dependence as well, so near the focus at z = 0, its field was:

$$|E|^2(r,z,t) = |\mathcal{E}_o|^2 \frac{W_o}{W^2(z)} \exp\left[-\frac{2r^2}{W^2(z)} - \alpha(z + \frac{\ell}{2}) - \gamma^2 t^2\right] \tag{24}$$

where $W^2(z) = W_o^2[1 + (2cz/\omega n W_o^2)^2]$, W_o is the minimum radius of the focus, α is the power attenuation coefficient due to scattering and linear loss, and γ is a constant. The sample cell extends from $z = -\ell/2$ to $z = \ell/2$. Following the analysis of Owyoung[6] using the paraxial approximation, we can describe each cylindrically symmetric set of rays in the focused beam by a parameter K defined by

$$r^2 = KW^2(z). \tag{25}$$

For each set of rays, the ellipse rotation can be evaluated using Eqs. (20) and (24) to give:

$$\theta_K(t) = \int_{-\ell/2}^{\ell/2} (\omega/2c)\delta n_c(K,z,t)dz$$

$$= \frac{1}{4}(|\mathcal{E}_o|^2\text{Cos } 2\phi)\ \frac{\pi^2\omega n W_o^2}{c}\ BLg(t)e^{-2K} \qquad (26)$$

where

$$L = \frac{2c}{\pi\omega n}\ e^{-\alpha\ell/2}\int_{-\ell/2}^{\ell/2}[e^{-\alpha z}/W^2(z)]dz$$

$$|\hat{e}_+\cdot\vec{E}|^2 - |\hat{e}_-\cdot\vec{E}|^2 = |E|^2\ \text{Cos } 2\phi \qquad (27)$$

$$g(t) = \frac{\sqrt{\pi}}{2\gamma\tau}\ e^{-1/r\ \gamma^2\tau^2}[1 + \text{erf}(\gamma t - \frac{1}{2\gamma\tau})]e^{-t/\tau}.$$

If the attenuation length $(1/\alpha)$ is much larger than the longitudinal focal dimension, $\omega n W_o^2/c$, then L can be approximated by

$$L = \frac{2}{\pi}\ e^{-\alpha\ell/2}[\tan^{-1}(c\ell/2\omega n W_o^2)] \qquad (28)$$

which reduces to $\exp(-\alpha\ell/2)$ when the sample length $\ell \gg \omega n W_o^2/c$. If in addition, $\ell \ll 1/\alpha$, then $L = 1$. In these experiments, we had $\ell \cong 5(\omega n W_o^2/c)$, and $\ell \cong (1/\alpha)$ resulting in $L \cong 0.45$.

We now have to integrate over all the rays in the beam to find the total power of the elliptically polarized light transmitted through the analyzer. In our case, $\theta_K \ll 1$, and hence the measured signal is

$$S^{ER}(t) = \int_0^{\infty}(\sin 2\phi)^2\theta_K^2(t)P_K(t)dK \qquad (29)$$

where

$$P_K(t)dK = (nc/4\pi)|E|^2(r,z = \ell/2,t)2\pi r dr$$

$$= (ncW_o^2/4)|\mathcal{E}_o|^2 \exp(-\ 2K - \alpha\ell - \gamma^2 t^2)dK$$

$$= \frac{P_o}{2} \exp(-\ 2K - \alpha\ell - \gamma^2 t^2)dK$$

and where P_o is the incoming peak power, $P_o = (ncW_o^2/8)|\mathcal{E}_o|^2$. We then have

$$S^{ER}(t) = \frac{4\pi^4\omega^2}{3\ c^4} P_o^3 \sin^2(4\phi)B^2L^2\Gamma(t)e^{-\alpha\ell} \tag{30}$$

where $\Gamma(t) = g^2(t)\exp(-\ \gamma^2 t^2)$.

In our experiment, we measured S^{ER}_{max} for the sample and used CS_2 as a reference whose Kerr constant is known. From Eq. (30), we find

$$B/B_{cs_2} = \left[\frac{S^{ER}_{max} e^{\alpha\ell}/L^2\Gamma_{max} P_o^3}{\left(S^{ER}_{max} e^{\alpha\ell}/L^2\Gamma_{max} P_o^3\right)_{cs_2}}\right]^{\frac{1}{2}} . \tag{31}$$

As seen from Eq. (30), S^{ER}_{max} is proportional to P_o^3. However, because of scattering and imperfect alignment, S^{ER}_{max} also has a residual term linear in P_o. Therefore, we measured S^{ER}_{max} as a function of P_o and extracted the term proportional to P_o^3 from the measurements.

We have measured τ, α, and B as functions of temperature in the isotropic phase for the seven homologous compounds of p,p'-di-n-alkoxy-azoxybenzenes. We have also found n and $\Delta\chi (= \delta\chi_{11}/Q_{xx})$ for these compounds using the wedge method of index refraction measurements[8] and the order parameters from magnetic resonance measurements.[9] Then, from Eqs. (6) and (19), we deduce the parameters ν, T^*, and a for each compound.

4. EXPERIMENTAL RESULTS

In Figs. 2 and 3, we show, as examples, the results of our measurements of τ and B respectively as functions of temperature for two p,p'-di-n-alkoxy-azoxzybenzene compounds. Similar results were obtained for the other five compounds in the homologous series. In all cases, the data can be described very well by Eqs. (6) and (19). Strictly speaking, the viscoscity coefficient ν in Eq. (6) is not temperature-independent. One often expresses $\nu(T)$ in the form

$$\nu(T) = \nu_o \exp(-W/T) \tag{32}$$

where W is a constant. However, in our cases, because the investigation was limited to a narrow temperature range, we can approximate $\nu(T)$ by $\nu(T_K)$. The error introduced by this approximation is less than 4%. Thus, by fitting the experimental data with the theoretical curves of Eqs. (6) and (19), we can deduce T^*, ν/a and $(\Delta\chi)^2/a$ for each compound. From the independently measured values of $\Delta\chi$,[8] we then obtain ν and a separately. As discussed in Sec. 2, if we believe in the Landau's expansion at the isotropic-nematic transition, we can also deduce the parameters b and d for these compounds using Eq. (21). Here, T_K's were measured, and the Q_K's were obtained from the linear birefringence measurements[8] normalized against the NMR results of Pines et al.[9] We have listed in Table III the values of $(T - T^*)\tau$, $(T - T^*)B$ and other parameters deduced from our measurements for the seven compounds of the homologous series. We have then plotted, as functions of the number of carbon atoms in the alkyl chain at either end of the molecule, $(T - T^*)\tau$ and $(T - T^*)B$

in Fig. 4, T^*, T_K, and ΔH in Fig. 5, ν and $\Delta\chi$ in Fig. 6, and a, b, and d in Fig. 7.

In our relaxation measurements, shot noise in the photonmultiplier was the main source of experimental uncertainty. Typical error of about ± 10% is represented by the error bars in Fig. 2 where each data point was the result of average over more than 4 laser shots. This uncertainty can be improved by using a probe beam of stronger intensity. As the relaxation time τ approaches the response time of the detection system ($\lesssim$ 7 nsec in our case), the uncertainty would of course become larger unless the signal is properly deconvoluted.

The ellipse-rotation measurements had an accuracy better than 2% so far as the signal S^{ER}_{max}/P_o^3 was concerned. However, in deducing the optical Kerr constant from Eq. (31), the uncertainty in the relaxation time τ came in through g(t). Together with the uncertainty (~ ± 5%) in determining L, this led to an overall uncertainty of ~ ± 15% in the values of B shown in Fig. 2.

5. DISCUSSION

Figures 4 - 7 show how the increase of alkyl chain length by the addition of CH_2 groups modifies the physical behavior of the homologous compounds. Here, we give a brief qualitative discussion of the results.

Figure 4 shows that the seven homologous compounds all have a large Kerr constant and a long relaxation time, which are characteristics of other liquid crystalline materials.[1] For the same $\Delta T = T - T^*$, $B\Delta T$ drops appreciably as N increases mainly due to a drop in $\Delta\chi$ shown in Fig. 6. On the other hand, $\tau\Delta T$ has a zig-zag behavior with increase of N. It is the result of the zig-zag behavior of ν also shown in Fig. 6.

In Fig. 5, we notice that a regular alteration of the isotropic-nematic transition temperatures T_K and T^* and the latent heat ΔH occurs between homologues containing odd and even numbers of carbon atoms in the alkyl chain. For T_K and ΔH, this is a common behavior for many homologous series of liquid crystalline compounds and is known to be the result of the cog-wheel arrangement of the carbon atoms along the alkyl chain. That the fictitious second-order transition temperature T^* also has such a behavior is a manifestation of the weak first-order transition characteristics of these compounds. Because of that, T_K and T^* never differ by more than 5°K. We also notice in Fig. 5 that $T_K - T^*$ becomes appreciably smaller for $N = 6$ and 7. This seems to suggest that the longer chains on the molecules make the transition closer to second order presumably due to the stronger waggling motion of the end segment and the falling off of the terminal interaction.

The viscosity coefficient ν shown in Fig. 6 also alters regularly between homologues containing odd and even numbers of carbon atoms in the alkyl chain. This is caused by the strong temperature dependence of ν as suggested in Eq. (32). In the present case, we can approximate $\nu(T)$ by $\nu(T_K)$. Then, according to Eq. (32), we expect to find smaller ν for compounds with large T_K and hence the qualitative behavior of ν in Fig. 6. However, we should not expect the constants ν_o and W in Eq. (32) to be the same for all the compounds in the homologous series. If they were, we would find $\log \nu(T_K)$ versus T_K^{-1} to be a straight line from which we could deduce ν_o and W. As shown in Fig. 8, this is certainly not the case for the PAA homologues.

The optical anisotropy in Fig. 6 shows a fairly smooth decrease with increase of the chain length. In fact, on the microscopic scale, the molecular polarizability anisotropy $\Delta\alpha$ actually increases with the increase of chain length as one would expect intuitively.[8] The fact that $\Delta\chi$ behaves differently from $\Delta\alpha$ is because of the molar volume effect. The medium with longer chain molecules has a lower molecular density. Its effect on $\Delta\chi$ turns out to be larger than the incremental effect of $\Delta\alpha$ on $\Delta\chi$ due to addition of methylene group on the chain.

Figure 7 shows that the variations of the Landau parameters a, b, and d with chain length do not have any regular pattern. The physical meanings of a, b, and d often depend on the model describing the intermolecular interaction. In the mean-field theory of Maier and Saupe,[10] we should expect a to be a constant independent of the compounds. The values of a for the seven homologous compounds in Fig. 7 however vary over a factor of 2. This suggests that the mean field theory for isotropic-nematic transition is actually a poor approximation. The values of b and d in Fig. 7 were deduced by assuming the Landau expansion of free energy is valid at the isotropic-nematic transition. To check the validity of the Landau expansion, we insert the values of a, b, and d in Eq. (2) with $Q \sim 0.4$ and $T = T_K$. We find that the b and d terms in Eq. (2) are often larger than the a term indicating a divergence or poor convergence of the power series expansion. Thus, at least the truncated Landau expansion in the form of Eq. (2) is not valid at $T = T_K$. The values of b and d given in Fig. 7 are therefore not very meaningful. For $T > T_K$ and $Q < 0.01$, however, Eq. (2) is valid. With the values of b and d given in Fig. 7, and for $Q < 0.01$, the b and d terms in Eq. (2) become negligible. This was true in our experiment where Q was always less than 10^{-3}.

In the literature, the Landau expansion has also been used to derive the heat content ΔH of a first-order transition

$$\Delta H = \frac{3}{4} a\, T_K Q_K^2 + \frac{5T_K}{12}\left(\frac{\partial b}{\partial T}\right)_{T_K} Q_K^3 + \frac{9T_K}{32}\left(\frac{\partial d}{\partial T}\right)_{T_K} Q_K^4. \tag{33}$$

If we neglect the $\partial b/\partial T$ and $\partial d/\partial T$ terms, then we have

$$\Delta H = \frac{3}{4} a\, T_K Q_K^2. \tag{34}$$

The above equation was used by Stinson et al.[7] Using the values of a, T_K, and Q_K listed in Tables I and III for the homologous compounds, we find the values of ΔH shown in Fig. 5 as ΔH_{th}. Compared with the directly measured values ΔH_{exp}, the agreement is fairly good for all compounds except N = 6 and 7. The discrepancy could be due to neglect of b and d terms in Eq. (33) or due to failure of the Landau expansion. It may also be the result of residual short-range smectic order at T_K since the N = 6 and N = 7 homologues are known to have a smectic phase at lower temperatures. The rapid rise of ΔH_{th} towards N = 6 and 7 comes from the corresponding rise of a which in turn is the result of quick drop of $B(T - T^*)$ towards N = 6 and 7.

6. CONCLUSION

Using ellipse rotation and transient optical Kerr effect, we have measured the third-order nonlinear susceptibility (or the optical Kerr constant B) and the corresponding relaxation time τ for seven nematic compounds of the p,p'-di-n-alkoxy-azoxybenzene homologous series as functions of temperature in the isotropic phase. The results showing critical divergence of B and critical slowing down of τ are in good agreement with predictions from the Landau-de Gennes' model. Similar in characteristics to other liquid crystalline materials, all these compounds have a large Kerr constant and a long relaxation time strongly dependent on temperature. Together with the existing data on optical anisotropy and the order parameter at the nematic-isotropic transition, we have deduced various characteristic parameters of the nematic compounds. These include the fictitious second-order transition temperature T^*, the orientational viscosity ν, the Landau expansion coefficients a, b, and d, the heat content ΔH, etc. The results show how these characteristic parameters vary among the homologous series as the alkyl chain length of the molecules increases through addition of methylene groups to the chain. Part of the results can be understood from the molecular structural point of view. The variation of the Landau parameter a with compounds indicates that the mean field theory of Maier-Saupe is not a good approximation to describe the isotropic-nematic transition. Our values of a, b, and d also suggest that the Landau series expansion of the free energy is a poor approximation at the transition. The heat contents ΔH derived from the expression $\Delta H = 3\ a\ T_K Q_K^2/4$ deviates appreciably from the experimental values for the higher members of the homologous series.

References

1. G. K. L. Wong and Y. R. Shen, Phys. Rev. Lett. 30, 895 (1973); Phys. Rev. A10, 1277 (1974); J. Prost and J. R. Lalanne, Phys. Rev. A8, 2090 (1973).
2. H. Arnold, Z. Phys. Chem. Leipzig 226, 146 (1964).
3. P. G. de Gennes, Phys. Lett. A30, 454 (1969) and Mol. Cryst. Liq. Cryst. 12, 193 (1971).
4. P. D. Maker and R. W. Terhune, Phys. Rev. 137, A801 (1965).
5. P. N. Butcher, "Nonlinear Optical Phenomena," (University Engineering Publications, Columbus, Ohio, 1965).
6. A. Owyoung, R. W. Hellworth, and N. George, Phys. Rev. B4, 2342 (1971); 5, 628 (1972); A. Owyoung, IEEE J. Quantum Electron. QE-9, 1064 (1974).
7. T. W. Stinson and J. D. Litster, Phys. Rev. Lett. 25, 503 (1970); T. W. Stinson, J. D. Litster, and N. A. Clarke, J. Phys. (Paris) 33, 69 (1972).
8. See Chapter III.
9. A. Pines, D. J. Ruben, and S. Allison, Phys. Rev. Lett. 33, 1002 (1974); More refined data are given by A. J. Pines and D. J. Ruben (to be published).
10. W. Maier and A. Saupe, Z. Naturf. A13, 564 (1958); A14, 882 (1959); A15, 287 (1960).

FIGURE CAPTIONS

Fig. 1(a) Experimental arrangement for observing molecular orientational relaxation times in nematic liquid crystals. BS, beam splitter; P-1, P-2, P-3 linear polarizers; D-1, ITT F4018 fast photodiode; D-2, RCA photomultiplier 6342A; F-1, neutral-density stacks.

(b) Experimental arrangement for observing ellipse-rotation effect. P-1, P-2, Glan polarizers; R-1, R-2, Fresnel rhombs; L-1, L-2, 10-cm lenses, F-1, F-2, neutral-density stacks; D-1, D-2, ITT fast photodiodes.

Fig. 2 Experimental results on optical Kerr constants versus temperature for $C_NH_{2N+1}O-C_6H_4-N_2O-C_6H_4-OC_NH_{2N+1}$ with N = 1 and 7. The solid curves are calculated from Eq. (6).

Fig. 3 Experimental results on orientational relaxation times versus temperature for $C_NH_{2N+1}O-C_6H_4-N_2O-C_6H_4-OC_NH_{2N+1}$ with N = 1 and 7. The solid curves are calculated from Eq. (19).

Fig. 4 Experimental values of $(T - T^*)B$ and $(T - T^*)\tau$ for the first seven p,p'-di-n-alkoxy-azoxybenzene homologues.

Fig. 5 Experimental values of T_K, T^*, and ΔH_{exp} for the first seven p,p'-di-n-alkoxy-azoxybenzene homologues. The values of ΔH_{th} were deduced from Eq. (34) using experimental values of a, T_K, and Q_K.

Fig. 6 Values of ν and $\Delta\chi$ for the first seven p,p'-di-n-alkoxy-azoxybenzene homologues.

Fig. 7 Values of the Landau expansion coefficients a, b, and d (see Eq. (2)) deduced from the experiment for the first seven p,p'-di-n-alkoxy-azoxybenzene homologues.

Fig. 8 Plot of log ν versus T_K^{-1} showing that the experimental data do not fall on a straight line.

TABLE CAPTIONS

Table I.	Molecular structures and other characteristic parameters of the p,p'-di-n-alkoxy-azoxybenzene homologues.
Table II.	Solvents used for recrystallization of the p,p'-di-n-alkoxy-azoxybenzene homologous compounds.
Table III.	Various characteristic parameters of the p,p'-di-n-alkoxy-azoxybenzene homologues deduced from the experiment.

TABLE I

Structure: $CH_3-(CH_2)_{N-1}-O-(C_6H_4)-N_2O-(C_6H_4)-O-(CH_2)_{N-1}-(CH_3)$

N	1	2	3	4	5	6	7
T_K(°C)	132.7	163.1	119.95	129.9	118.6	123.9	119.3
Q_K	.400	.517	.395	.475	.358	.437	.431
$\Delta\chi$ ($X10^{-3}$)	108.9	97.1	87.2	79.0	74.9	64.5	60.9
ΔH_{exp}(10^6 erg/cm^3)	25.4	52.5	22.8	31.4	19.9	26.2	23.5

TABLE II

N	1	2	3	4	5	6	7
Solvent	1-pentanol		n-hexane	1-pentanol	acetone		

TABLE III

N	1	2	3	4	5	6	7
$(T_K - T^*)$(°K)	3.0	3.8	2.75	4.9	4.4	0.9	0.7
$\tau\Delta T(10^{-9}$sec°K)	90	80	180	155	240	150	140
$B\Delta T(10^{-5}$esu)	10.5	9.2	9.0	8.9	6.4	3.9	2.2
$\nu(10^{-3}$poise)	62.6	52.1	95.9	68.9	135.4	105.1	151.3
$a(10^5$ergs/cm^3°K)	6.69	6.52	5.33	4.45	5.57	7.00	10.81
$b(10^7$ergs/cm^3)	21.0	19.4	15.0	17.9	24.1	4.4	6.0
$d(10^7$ergs/cm^3)	41.1	27.3	29.7	29.1	49.4	6.9	10.1
$\Delta H_{th}(10^6$ergs/cm^3)	33.9	56.9	24.6	30.3	20.9	39.8	59.0

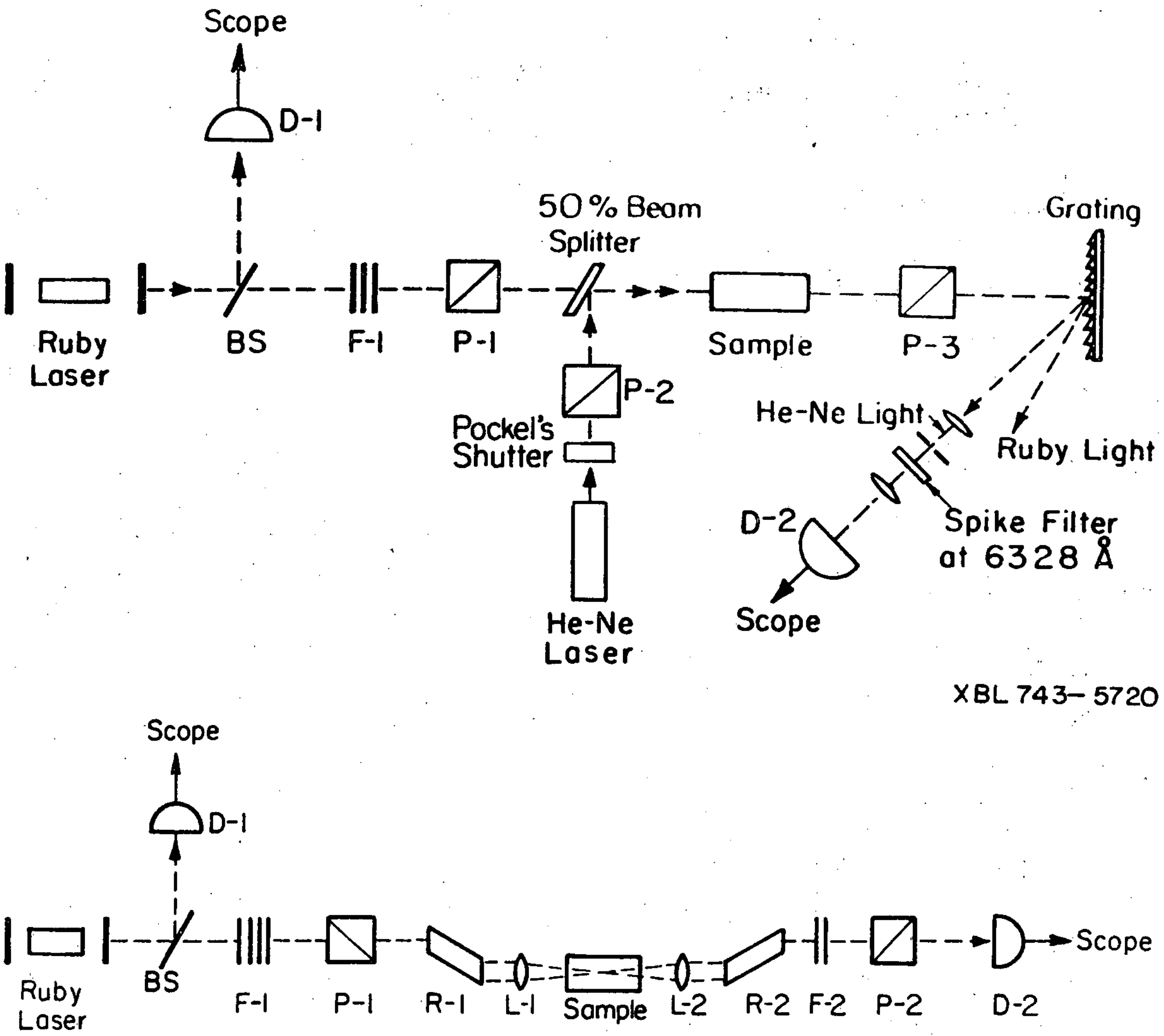

XBL 743-5720

XBL 743-5713A

Fig. 1

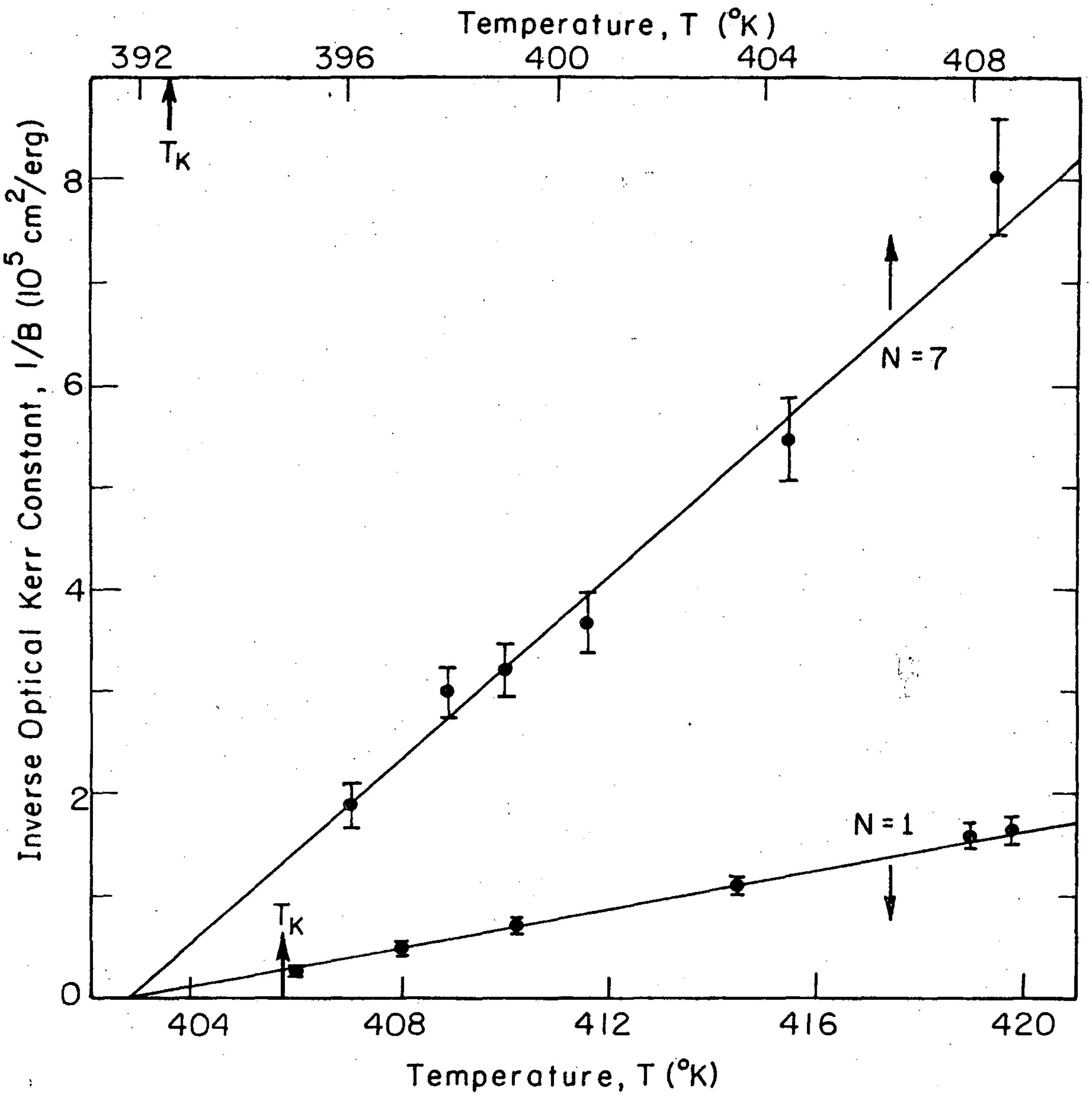

XBL 761-6335

Fig. 2

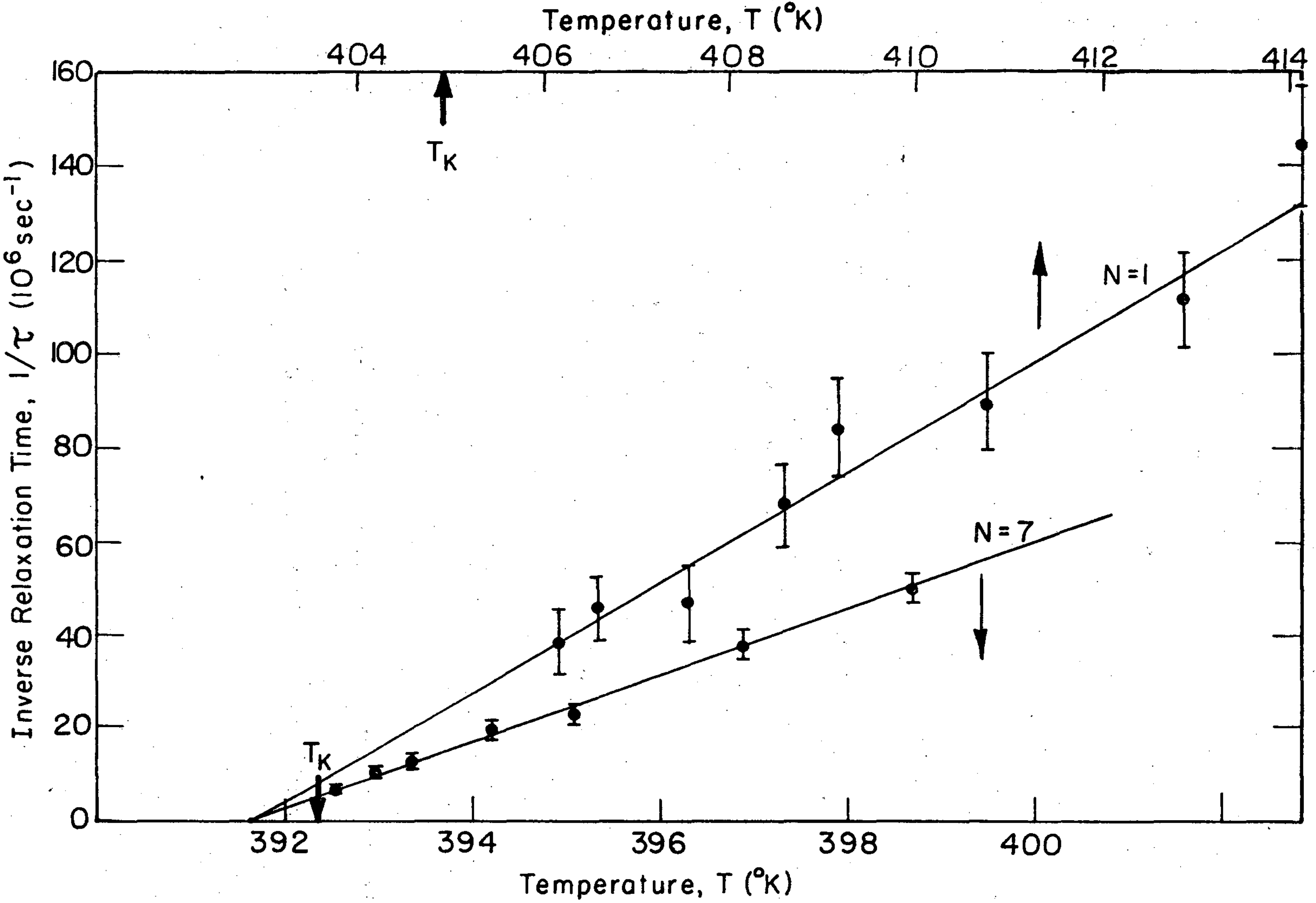

XBL 761-6336

Fig. [illegible]

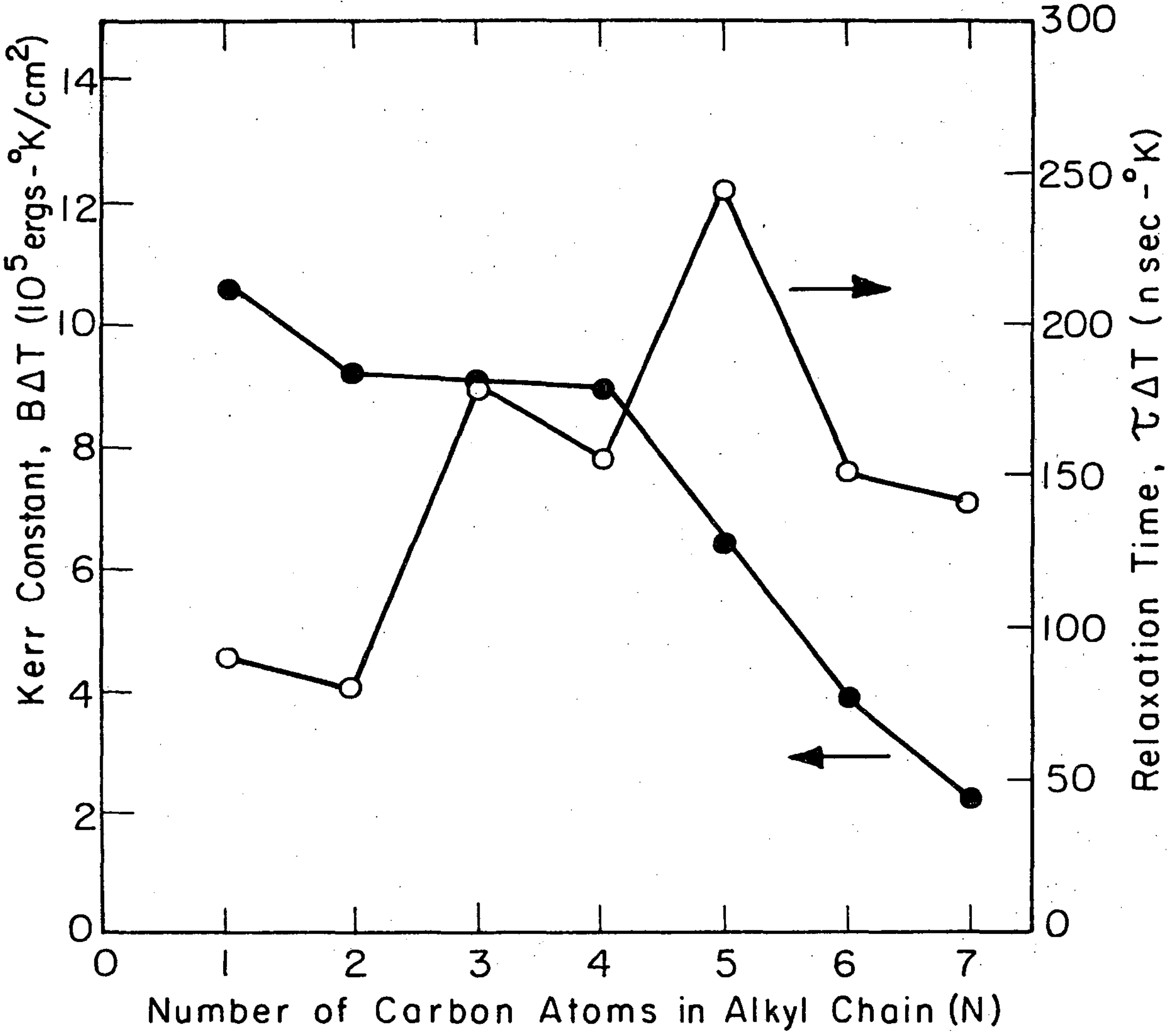

XBL 761-6334

Fig. 4

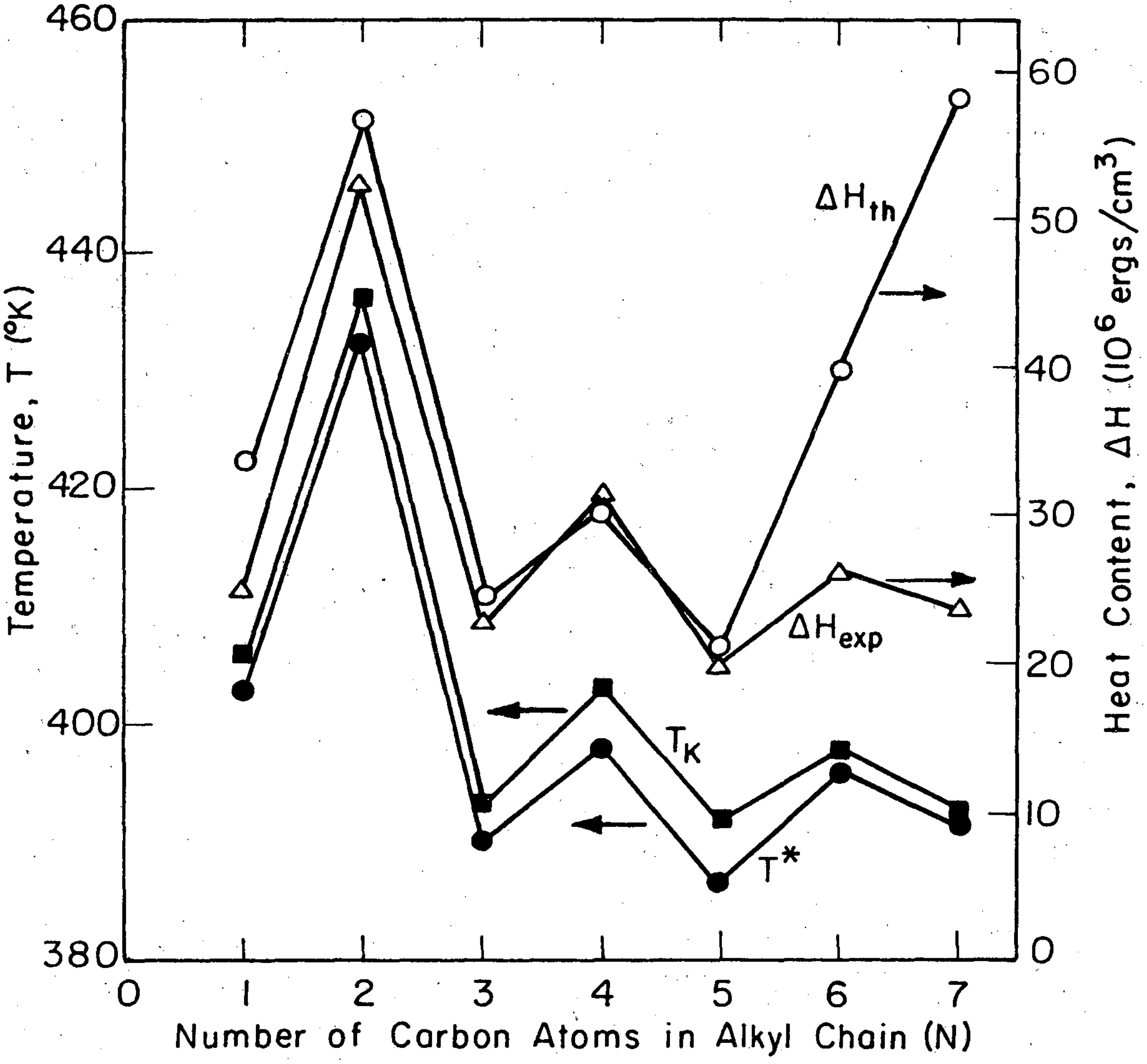

XBL 761-6333

Fig. 5

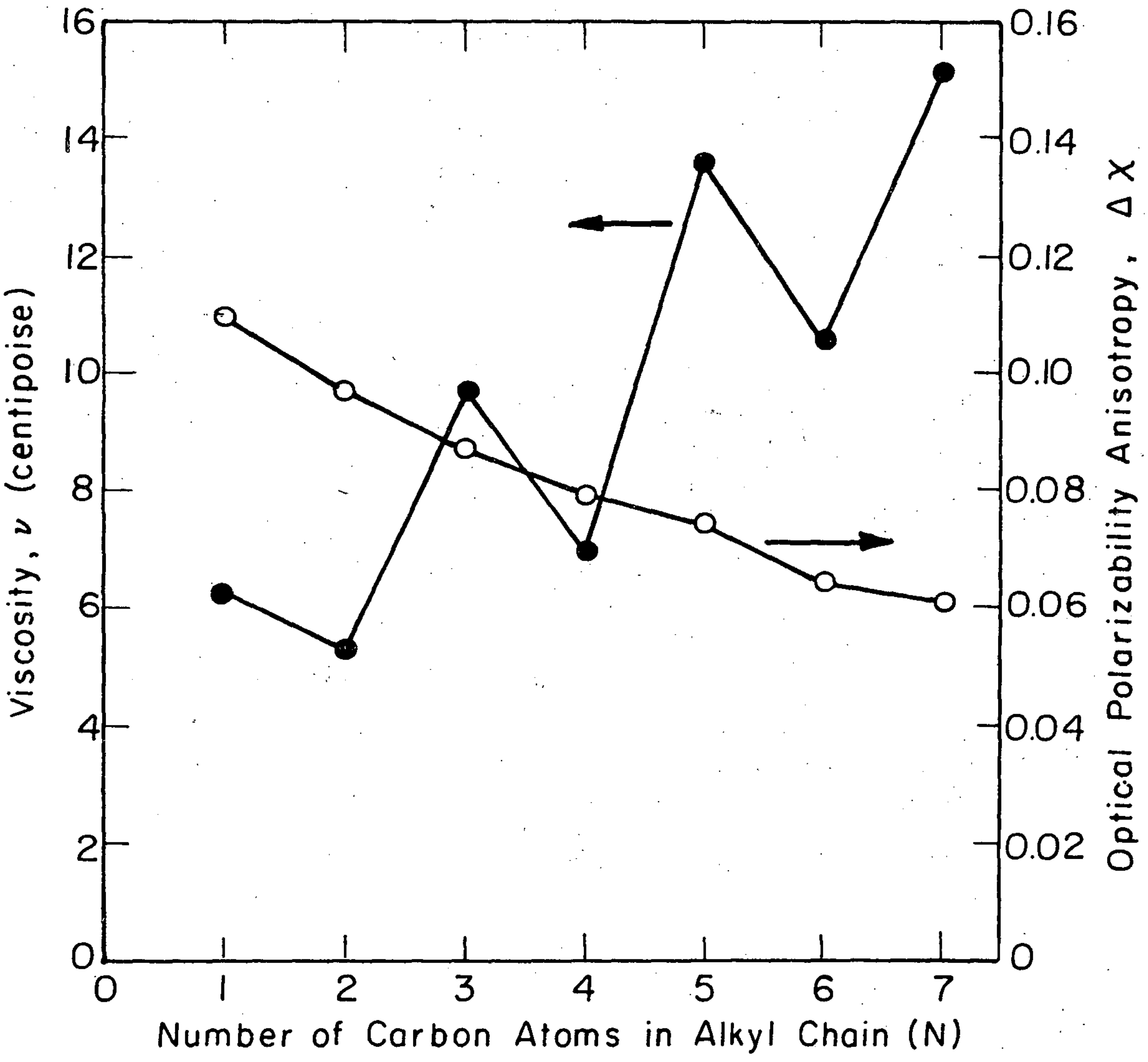

XBL 761-6332

Fig. 6

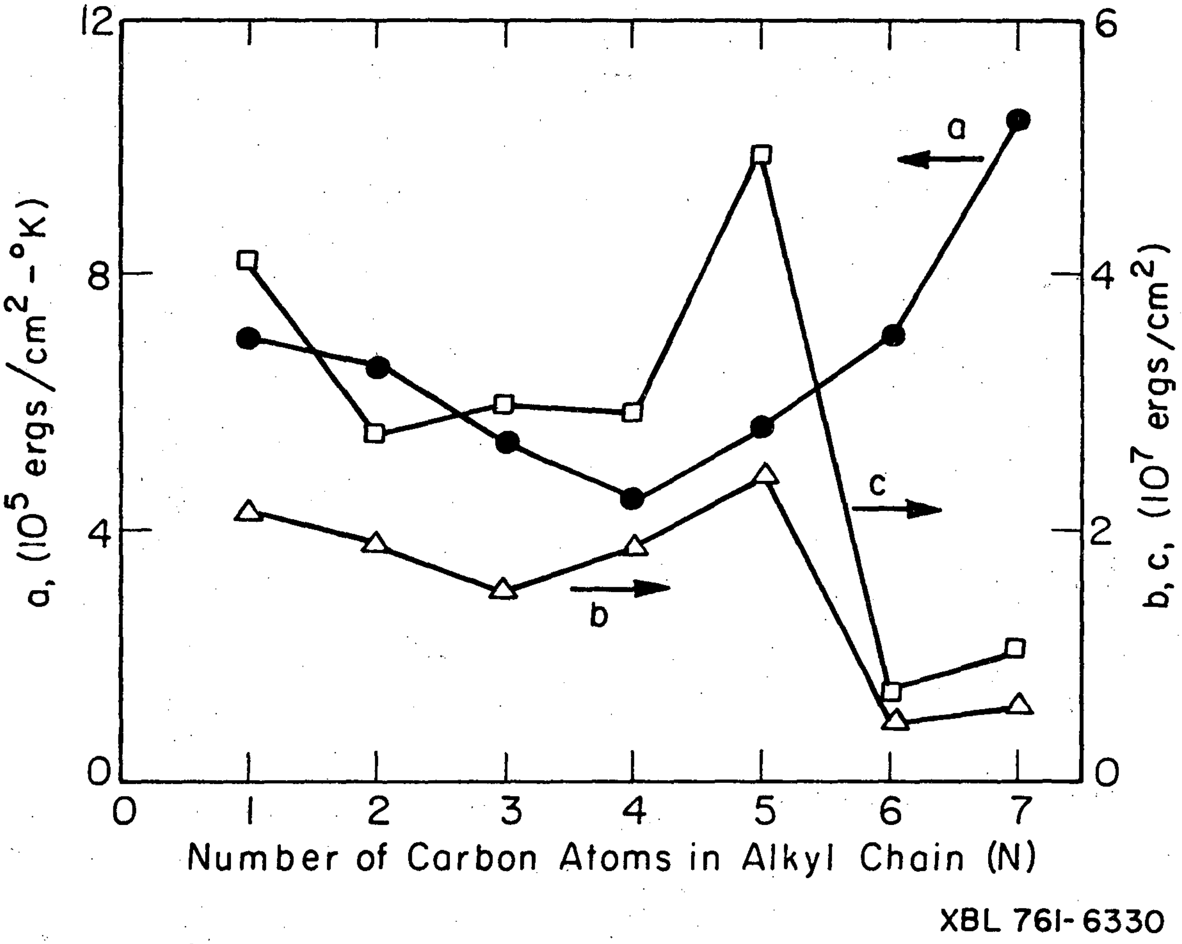

12
8
4
0
6
4
2
0
0
1
2
3
4
5
6
7
a
b
c
a, (10^5 ergs/cm^2-°K)
b, c, (10^7 ergs/cm^2)
Number of Carbon Atoms in Alkyl Chain (N)
XBL 761-6330

Fig. 7

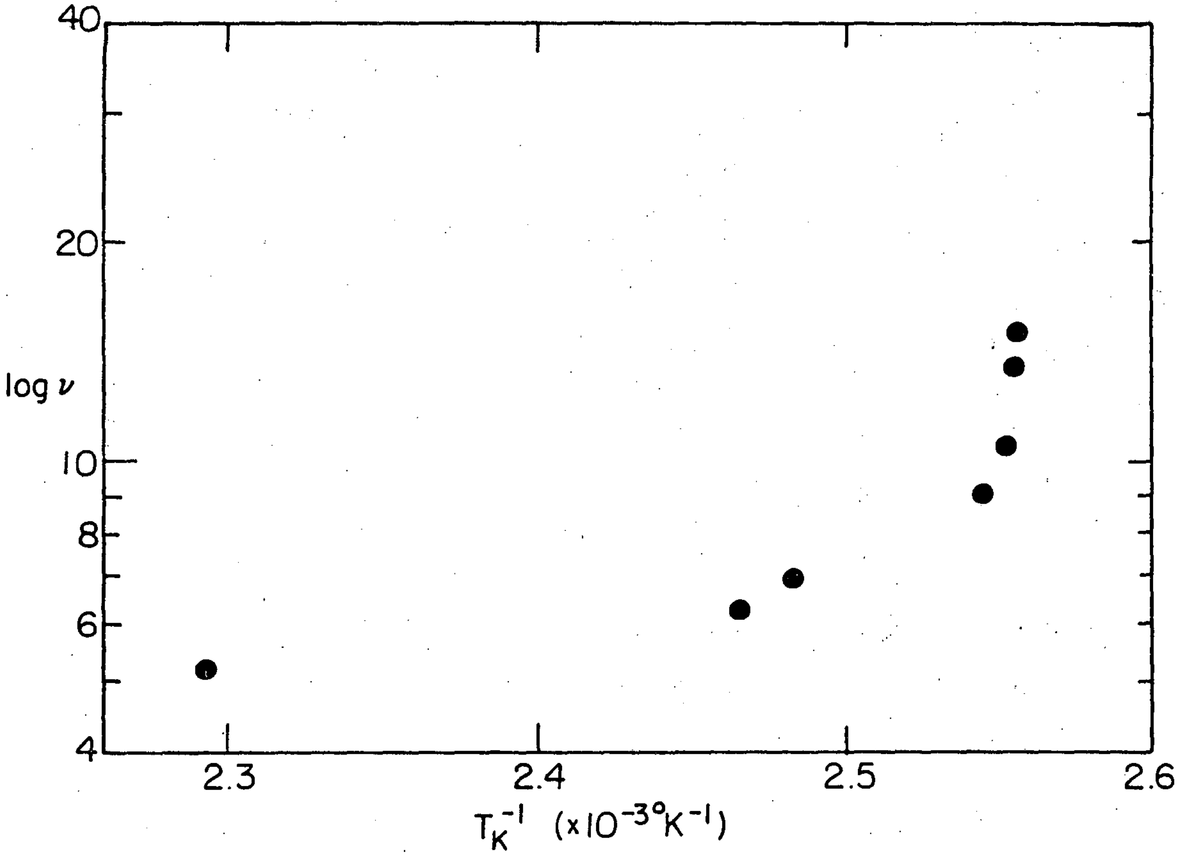

XBL 762-6511

Fig. 8

III. REFRACTIVE INDICES AND OPTICAL ANISOTROPY OF HOMOLOGOUS LIQUID CRYSTALS

1. INTRODUCTION

Among the many interesting properties of liquid crystals, optical birefringence is probably the most important. It is the basis of liquid crystal display as well as other device applications. Physically, the strong optical birefringence arises from alignment of molecules with large molecular anisotropy.[1] The molecular anisotropy reflects not only the geometric shape of the molecules but also anisotropy of their electronic orbitals. With increasing molecular alignment in the nematic phase, the optical birefringence increases accordingly. It can therefore be used as a measure of the nematic order.

As emphasized by de Gennes,[2] any tensorial property of the nematics can be used to define a nematic order parameter. Thus, we can write the refractive indices parallel and perpendicular to the direction of molecular alignment as

$$\begin{aligned} n_{\parallel} &= \bar{n} + \frac{2}{3} Q_n \Delta n \\ n_{\perp} &= \bar{n} - \frac{1}{3} Q_n \Delta n \end{aligned} \qquad (1)$$

where $\bar{n}$ is the average refractive index, Q_n the order parameter, and Δn the birefringence corresponding to full molecular alignment ($Q_n = 1$). From Eq. (1), the optical birefringence is given by

$$\delta n = n_{\parallel} - n_{\perp} = Q_n \Delta n. \qquad (2)$$

The order parameter Q_n defined in Eq. (1) is in general not identical to the order parameters defined through other tensorial properties such as electric and magnetic susceptibilities, although all order parameters should range from 0 for random molecular orientation to 1 for perfect alignment. In particular, because of local-field correction due to intermolecular interaction, Q_n should be different from the microscopic order parameter defined as[2]

$$S = \langle (3 \cos^2\theta - 1)/2 \rangle \tag{3}$$

where θ is the angle between the long molecular axis and the average direction of molecular alignment. However, with a given model for local-field correction, there should be a definite relation between Q_n and S. For example, the Vuks' model gives[3]

$$\delta n = (4\pi/3)N(\overline{n^2} + 2)\delta\alpha/(n_{\parallel} + n_{\perp}) \tag{4}$$

$$(\Delta\alpha/\overline{\alpha})S = (n_{\parallel} + n_{\perp})\delta n/(\overline{n^2} - 1) \tag{5}$$

where $\delta\alpha = \alpha_{\parallel} - \alpha_{\perp} = S\Delta\alpha$, N is the number of molecules per unit volume, the superbars indicate average over molecular orientations, $\alpha_{\parallel}$ and $\alpha_{\perp}$ are the average polarizabilities parallel and perpendicular to the direction of alignment respectively, and $\Delta\alpha$ is the polarizability anisotropy at $S = 1$. From Eqs. (2) and (4), we find immediately

$$S = \frac{(2\overline{n} + Q_n\Delta n/3)}{(2\overline{n} + \Delta n/3)} Q_n . \tag{6}$$

Usually, we have $\Delta n \sim 0.4$ and $\bar{n} \sim 1.6$. Then, Eq. (6) shows that for intermediate values of Q or S, the two order parameters can differ by a few percent and Q_n is not strictly proportional to S.

In addition, Q_n is different from the order paramter Q_χ defined by:

$$\delta\chi = \chi_{\parallel} - \chi_{\perp} = Q_\chi \Delta\chi \tag{7}$$

where $\chi_{\parallel}$ and $\chi_{\perp}$ are the average macroscopic polarizabilities parallel and perpendicular to the direction of alignment respectively, and $\Delta\chi$ is the polarizability anisotropy for perfect alignment ($Q_\chi = 1$). We can evaluate Q_χ using

$$\delta\chi = \frac{1}{4\pi} (n_{\parallel}^2 - n_{\perp}^2) = Q_n \frac{\Delta n}{4\pi} \left(2\bar{n} + \frac{Q_n \Delta n}{3}\right) . \tag{8}$$

From equations (6), (7), and (8), we find

$$Q_\chi = \left(\frac{2\bar{n} + Q_n \Delta n/3}{2\bar{n} + \Delta n/3}\right) Q_n = S. \tag{9}$$

In Chapter II, the theory was developed in terms of the order parameter Q_χ. Here in Chapter III, we will drop the subscripts and define $Q \equiv Q_n$, since we have $S = Q_\chi$.

Several authors have suggested that one can express the temperature dependence of the order parameter S in the form[4,5]

$$S = (1 - T/T^+)^\gamma \tag{10}$$

where T^+ and γ are constant coefficients. Then, by least-square fitting the results of $(\Delta\alpha/\bar{\alpha})S$ versus T to the form $A(1 - T/T^{+})^{\gamma}$, one can deduce both the absolute values of S and $\Delta\alpha/\bar{\alpha}$. Such an approach, however, has implicitly assumed that S = 1 at T = 0°K and $A = \Delta\alpha/\bar{\alpha}$. These assumptions are not justifiable. In fact, as we shall see later from our work, S can indeed be approximated by $S_o(1 - T/T^{+})^{\gamma}$ but the constant S_o is different from 1.

Experimentally, δn can be measured with very high accuracy.[4] If we neglect the temperature dependence of Δn, then $\delta n(T)$ gives directly the variation of nematic order with temperature. On the other hand, if a particular local field model is chosen and $n_{\parallel}(T)$ and $n_{\perp}(T)$ are measured, we should be able to find the temperature dependence of Q and S without making other assumptions. The absolute values of Q and S, however, have to come from other measurements.

There already exist in the literature a number of reports on the measurements of refractive indices and optical birefringence of liquid crystals and their temperature dependence.[5] From these measurements, the order parameters were deduced and compared with those obtained from other measurements. One would expect that these measurements carried out on a homologous series of liquid crystals could yield valuable information about the effects of molecular structure on refractive indices, optical anisotropy, and molecular ordering. However, no such measurements have yet been reported.

In this chapter, we present the results of refractive index measurements on the homologous series of p,p'-di-n-alkoxy-azoxybenzenes. We first describe in Sec. 2 the experimental arrangement, sample preparation, and experimental results. We then deduce the order parameters as functions of temperature for the homologous nematics and compare them with the microscopic order parameters deduced from nuclear magnetic resonance (NMR) measurements.[6] In Sec. 3, we discuss the results and show how the increase of alkoxy chain length on the molecules affects the average molecular polarizability and the polarizability anisotropy.

2. EXPERIMENT

We used the wedge method to measure the refractive indices and linear birefringence of the nematics.[4,7] As shown in Fig. 1, the wedge was made of two glass plates with a 0.015 in. tungsten wire as the spacer to give an apex angle β of 0.0210 radian. The glass plates were coated with a surfactant (Dow Corning XZ 2-2024) and rubbed along the wedge axis. The wedge was then mounted in a hot stage, using a small phosphor bronze spring to hold the glass plates together and to insure that the apex angle β remained constant during each experimental run. It was put under a microscope and illuminated by a He-Ne laser beam. The incoming beam was partially reflected by the wedge, at an angle $\theta_o = 2\beta$. By measuring θ_o, the apex angle β was deduced with an accuracy of better than ±0.2%. It was essential to remeasure β for each experimental run, because β varied by ±2% from one run to another. This precaution was not taken in the original use of the wedge method.[4,7]

The hot stage was heated into the nematic temperature range, and the sample was added without disturbing the apex angle β. Then the top of the hot stage was installed, and the sample was allowed to reach thermal equilibrium. The hot stage temperature was maintained stable to ~ 0.1° C using a proportional thermal controller. Thin glass windows on the top and the bottom of the stage were used to prevent cooling of the wedge by convection. As a result, a temperature uniformity of ~ 0.1° C was achieved at an operating temperature of ~ 130° C.

The sample was studied between crossed polarizers. The polarizer axes were oriented at 45° to the nematic director, which was parallel to the wedge axis. As seen in Fig. 1, the incoming laser beam produced two reflected beams at angles θ_1 and θ_2 respectively from the sample. They were polarized parallel and perpendicular to the wedge axis respectively. The refractive indices $n_{\parallel}$ and $n_{\perp}$ could then be deduced from the Snell's law $n_{\parallel,\perp} = \sin\theta_{1,2}/\sin 2\beta$ if θ_1 and θ_2 were measured. At the same time, we could use the microscope to photograph the interference fringes in the beam transmitted through the sample. From the observed fringe spacing d, we could deduce the linear birefringence

$$\delta n = \lambda/\beta d \tag{11}$$

where λ is the He-Ne laser wavelength.

In our experiment, the samples of azoxybenzene derivatives ($C_NH_{2N+1}O - C_6H_4 - N_2O - C_6H_4 - C_NH_{2N+1}O$ with N = 1, 2, - - -, 7) were purchased from Kodak Co. and recrystallized before use. The nematic-isotropic transition temperatures T_K remained constant during the measurement and were measured to an accuracy of ± 0.05°K. The accuracy of the refractive index measurements was better than ± 0.3%. The spacing of the interference fringes was determined by averaging over 20 ± 0.1 fringes. This led to a δn accurate to < 0.5%.

The results of our measurements of $n_{\parallel}$ and $n_{\perp}$ versus temperature for the seven homologous nematic liquid crystals are presented in Fig. 2. The directly measured linear birefringence data δn versus T are shown in Fig. 3. In all cases, $n_{\parallel} - n_{\perp}$ from the refractive index measurements and δn from the linear birefringence measurements agree well within the experimental accuracy. Our results on the N = 1 and N = 2 compounds agree very well with those reported earlier.[8]

As we mentioned in the last section, one can define a macroscopic order parameter $Q = \delta n/\Delta n$. With a given model of local field correction, Q is then related to the microscopic order parameter S. Here, we adopted the Vuks' local-field model.[3] Knowing $\delta n(T)$, $n_{\parallel}(T)$, and $n_{\perp}(T)$, we could find from Eqs. (5) and (6) the relative values of S and Q versus T, realizing that $\Delta\alpha/\overline{\alpha}$ should be essentially independent of temperature. Then, for each sample, we normalized our S value at a temperature sufficiently far below T_K (where T_K is the nematic-isotropic transition temperature) against the absolute S value obtained by Pines et al. from measuring the chemical shifts of the ^{13}C NMR spectra.[6] The results of S and Q versus T thus obtained are shown in Fig. 4. As an example, we compare our S(T) results for PAA with those of Pines et al. obtained from NMR in Fig. 5(a). We also show in Fig. 5(b) Q(T) and $\delta n(T)/\Delta n(T_o)$ for PAA, where T_o is arbitrarily chosen to be 31°K below T_K.

In the process of deducing S, we also obtained values of $\Delta\alpha/\overline{\alpha}$ for the seven homologous compounds. They are listed in Table I and plotted in Fig. 6 together with the order parameters $S(T_K)$ deduced from extrapolation of the curves in Fig. 4.

3. DISCUSSION

The highly accurate measurements of refractive indices and linear birefringence enables us to obtain the temperature variation of the order parameters with very good accuracy. The relative accuracy of S and Q shown in Fig. 4 is certainly within 1%. The absolute values of S and Q depend on calibration of S at one temperature against measurements of Pines et al. which were accurate to within ± 3%.

In deducing the values of S and Q, we have used the Vuks' local-field model. We can check the validity of this model by comparing our S versus T curves with those of Pines et al.[6] The NMR experiment of Pines et al. measures the chemical shifts of ^{13}C spectra from which the microscopic order parameter can be deduced. As shown in Fig. 5(a) for PAA, our results are in encellent agreement with theirs. Aside from the point at T_K, the highest discrepancy is about 1% and is certainly within the experimental uncertainty. The same is true for all the other homologous compounds we have studied. This shows that the Vuks' model is adequate for the present application of local-field correction.

Figure 4 shows a clear difference between the macroscopic order parameter Q and the microscopic order parameter S. The difference is due to local-field correction which is governed by Eq. (6) in the Vuks' model. In all cases, Q is larger than S by 0.5-2%, as it should be.

One may think that the temperature dependence of Δn in Eq. (2) should be negligible so that the linear birefringence δn versus T measures directly Q versus T. Actually, this is not true as can be seen in Fig. 5(b) comparing Q with $\delta n/\Delta n(T_o)$ for PAA where $T_o = T_k - 30.8°C$. The discrepancy between Q and $\delta n/\Delta n(T_o)$ is however less than 3%. This is also true for all the homologous compounds. The variation of Δn over a temperature range of 40°C is about 4%. It is presumably due to thermal expansion of the medium. The latter can be estimated from the expression

$$N\overline{\alpha} = (3/4\pi)(\overline{n^2} - 1)/(\overline{n^2} + 2) \qquad (12)$$

since $\overline{\alpha}$ should be independent of temperature. As an example, we show $N\overline{\alpha}$ versus T for PAA in Fig. 7. From the results, we can deduce the thermal expansion coefficient dV/Vdt. We have listed the values of dV/Vdt for the seven homologous compounds in Table I and plotted them in Fig. 8. The first two agree well with those reported in the literature.[9]

For all the seven homologous compounds, we can fit our data of S versus T by an equation of the form

$$S = S_o(1 - T/T^+)^\gamma \qquad (13)$$

where S_o, γ, and T^+ are constants to be determined. We have listed the values of S_o, γ, and $T^+ - T_K$ for all the compounds in Table II. Contrary to what has been suggested,[4,5] we find in no case does $S_o = 1$. As mentioned in Sec. I, this means that from the refractive index measurements only, it is not possible to obtain the absolute values of the order parameter S and the polarizability anisotropy $\Delta\alpha/\bar{\alpha}$. We note, however, that the exponent γ for all compounds except N = 3 falls in a narrow range between 0.181 and 0.192. The physical meaning of such a coincidence is not clear to us.

The values of $T^+ - T_K$ show a zigzag variation as N varies from 1 to 7. This actually reflects the well known zigzag behavior of $S(T_K)$ among the homologous compounds resulting from the cogwheel configuration of the alkyl chains. From either Eq. (13) or simple extrapolation of the curves in Fig. 4 to T_K, we can obtain $S(T_K)$ for all compounds. They are plotted in Fig. 6 showing explicitly the zigzag behavior. We compare our values of $S(T_K)$ with those of Pines et al[6] in Table I. The discrepancy of ~ 10% is mainly due to inaccuracy in our extrapolation procedure and partly due to the larger uncertainty in the measurements of Pines et al at T_K.

Figure 6 also shows that $\Delta\alpha/\overline{\alpha}$, the anisotropy of molecular polarizability normalized against the average polarizability, decreases almost linearly with the number of carbon atoms in the alkyl chain or with the increase of chain length. This suggests that the polarizability anisotropy $\Delta\alpha$ mainly comes from the core (azoxybenzene) contribution. The covalent bond electrons in the alkyl chain, on the other hand, contribute more to the average polarizability than to the anisotropy. As a result, the addition of the CH_2 groups to the alkyl chain increases $\overline{\alpha}$ much more than $\Delta\alpha$, and so $\Delta\alpha/\overline{\alpha}$ decreases with N. We can find $\overline{\alpha}$ and $\Delta\alpha$ explicitly if $\mathcal{N}$ is known. It turns out that the molar volumes of the seven homologous compounds studied here have actually been measured by Linsert.[11] Therefore, from Eq. (12) and our results on $\overline{n^2}$ and $\Delta\alpha/\overline{\alpha}$, we can deduce the values of $\overline{\alpha}$ and $\Delta\alpha$ separately. They are listed in Table I and plotted in Fig. 9. As N increases from 1 to 7, $\overline{\alpha}$ rises almost linearly by a factor of 1.8 while $\Delta\alpha$ shows a saturable increase of a factor of 1.18. The saturation of $\Delta\alpha$ at larger N is presumably because the waggling end segment of the chain is more disordered than the core. By assuming an order parameter S_A which varies along the alkyl chain, Marčelja[10] has calculated S_A/S as a function of N. We can then write

$$\Delta\alpha = \Delta\alpha_o + (S_A/S)N\Delta\alpha_A \tag{14}$$

where $\Delta\alpha_o$ comes from the core and $\Delta\alpha_A$ from each CH_2 group in the chain. Using Marčelja's values of S_A/S, we can fit the data of $\Delta\alpha$ versus N with Eq. (14) in Fig. 9, but the result suggests that Marčelja's values of S_A/S do not decrease fast enough with N. The least-square fit gives $\Delta\alpha_o = 25.6\text{x}10^{-24}$ and $\Delta\alpha_A = 2.06\text{x}10^{-24}$.

4. CONCLUSION

Highly accurate measurements of refractive indices and optical anisotropy together with a local-field model enables us to deduce the temperature dependence of both microscopic and macroscopic order parameters with very good accuracy. We have made these measurements on seven homologous compounds of $C_NH_{2N+1}O - C_6H_4 - N_2O - C_6H_4 - OC_NH_{2N+1}$ with N = 1, – – –,7. Using the Vuks' model for local-field correction and calibrating the microscopic parameter at one temperature against that obtained by Pines et al from NMR measurements, we have deduced as functions of temperature absolute values of both microscopic and macroscopic order parameters for these compounds. They agree very well with the results of Pines et al on the temperature dependence of the microscopic order parameters. This shows that the Vuks' model is adequate in the present application. Our results also indicate that the use of the linear birefringence $\delta n(T)$ as a direct measure of the temperature dependence of the order parameter could lead to a few percent error.

We have shown that for all the homologous compounds, the microscopic order parameter S as a function of temperature can be described by a simple equation $S = S_o(1 - T/T^+)^\gamma$, but S_o is not equal to 1 as has been suggested by others. Our results on the homologous series also yield information about the effects of molecular structure on the optical properties. We have found that with increasing N from 1 to 7 in the C_NH_{2N+1} alkyl chain the average polarizability increases by a factor of 1.8 while the polarizability anisotropy only increases by a factor of

1.18. Using Marčelja's calculation, we have also been able to deduce separately the contributions to the polarizability anistropy from the core and from the CH_2 groups in the chain.

References

1. See, for example, P. G. de Gennes, "Physics of Liquid Crystals", Clarendon Press, Oxford (1974).
2. P. G. de Gennes, Mol. Cryst. Liq. Cryst. <u>12</u>, 193 (1971).
3. M. F. Vuks, Optics Spectr. <u>20</u>, 644 (1966); (English Translation: Optics Spectr. <u>20</u>, 361 (1966).) See, also, S. Chandresekhar and N.V. Madhusudana, J. Phys. (Paris) Suppl. <u>30</u>, C4-24 (1969).
4. I. Haller, H. A. Huggins, H. R. Lilienthal, and T. R. McGuire, J. Phys. Chem. <u>77</u>, 950 (1973).
5. I. Haller, Progress in Solid State Chemistry <u>10</u>, 103 (1975), and references therein.
6. A. Pines, D. J. Ruben, and S. Allison, Phys. Rev. Lett. <u>33</u>, 1002 (1974). The S values used in this work are obtained from their more recent refined data; A. Pines and D. J. Ruben (to be published).
7. I. Haller, H. A. Huggins, and M. J. Freiser, Mol. Cryst. Liq. Cryst. <u>16</u>, 53 (1972).
8. M. Brunet-Germain, Mol. Cryst. Liq. Cryst. <u>11</u>, 289 (1970).
9. E. Bauer and J. Bernament, J. Phys. Radium <u>7</u>, 19 (1936); W. Maier and A.Saupe, Z. Naturforsch. <u>15a</u>, 287 (1966).
10. See, for example, G. W. Gray, "Molecular Structure and the Properties of Liquid Crystals", (Academic Press, New York, 1962), Chapter IX; S. Marčelja, J. Chem. Phys. <u>60</u>, 3599 (1974).
11. F. Linsert, Diplomarbeit, 1945, Universität Halle; H. Gruler, Z. Naturforsch. <u>28a</u>, 474 (1973).

FIGURE CAPTIONS

Fig. 1. Schematic of the wedged sample.

Fig. 2. Refractive indices of the seven azoxybenzene derivatives ($N = 1, 2, ---, 7$) as functions of temperature. T_K is the isotropic-nematic transition temperature. For $T < T_K$, the upper and lower branches of the curves refer to optical polarizations parallel and perpendicular to the molecular alignment respectively.

Fig. 3. Linear birefringence δn of the seven azoxybenzene derivatives as functions of temperature.

Fig. 4. Microscopic order parameter S and macroscopic order parameter Q versus temperature for the seven azoxybenzene derivatives.

Fig. 5. (a) Comparison of microscopic order parameters obtained in this work for p-azoxyanisole (PAA) with those of Pines et al in Ref. 6. (b) Comparison of Q versus T with δn versus T for PAA.

Fig. 6. Variations of $\Delta\alpha/\overline{\alpha}$ and $S(T_K)$ with the number of carbon atoms in the alkyl chain of the p, p'-di-n-alkoxy-azoxybenzene homologous series.

Fig. 7. Variation of $4\pi N\overline{\alpha}/3$ with temperature for p-azoxyanisole.

Fig. 8. Thermal expansion coefficient dV/Vdt, averaged over the nematic temperature range of the seven azoxybenzene derivatives.

Fig. 9. Variations of $\overline{\alpha}$ and $\Delta\alpha$ with the number of carbon atoms in the alkyl chain of the p,p',-di-n-alkoxy-azoxybenzene derivatives. The solid line is a theoretical fit using Eq. (11).

TABLE CAPTIONS

Table I. Values of $\Delta\alpha/\overline{\alpha}$, T_K, $S(T_K)$, dV/VdT, $\overline{\alpha}$, and $\Delta\alpha$ for the axozybenzene derivatives with N = 1, 2, - - -, 7.

Table II. Values of S_o, γ, and $T^+ - T_K$ obtained by least-square fitting of our data on S versus T to the form $S = S_o(1 - T/T^+)^\gamma$ for the azoxybenzene derivatives with N = 1, 2, - - -, 7.

TABLE I

N	1	2	3	4	5	6	7
$\Delta\alpha/\bar{\alpha}$	.830	.797	.746	.704	.636	.603	.545
$T_K(^\circ K)$	406.2	440.3	392.8	406.2	392.2	397.7	393.6
$S(T_K)^a$	.40	.517	.395	.475	.358	.437	.431
$S(T_K)^b$	.37	.487	.396	.436	.410	.485	.432
$dV/VdT(^\circ C^{-1})^a$	$7.8\mathrm{x}10^{-4}$	$9.4\mathrm{x}10^{-4}$	$8.0\mathrm{x}10^{-4}$	$8.9\mathrm{x}10^{-4}$	$8.2\mathrm{x}10^{-4}$	$7.1\mathrm{x}10^{-4}$	$5.4\mathrm{x}10^{-4}$
$dV/VdT(^\circ C^{-1})^c$	$8.2\mathrm{x}10^{-4}$	$9.6\mathrm{x}10^{-4}$	—	—	—	—	—
$\bar{\alpha}(\mathrm{x}10^{-24})$	31.9	36.5	39.8	43.7	49.5	51.0	57.4
$\Delta\alpha(\mathrm{x}10^{-24})$	26.5	29.1	29.7	30.8	31.5	30.8	31.3

[a] This work

[b] Pines et al (Ref. 6)

[c] Ref. 9

TABLE II

N	1	2	3	4	5	6	7
S_o	1.13 ± .03	1.27 ± 03	1.11 ± .03	1.32 ± .02	1.24 ± .02	1.34 ± .02	1.4 ± .04
γ	.189 ± .008	.182 ± .008	.155 ± .01	.192 ± .008	.181 ± .007	.189 ± .006	.188 ± .01
$T^+ - T_K$(°K)	1.8 ± .3	3.3 ± .5	0.5 ± .2	2.0 ± .2	0.4 ± .2	1.1 ± .2	0.8 ± .2

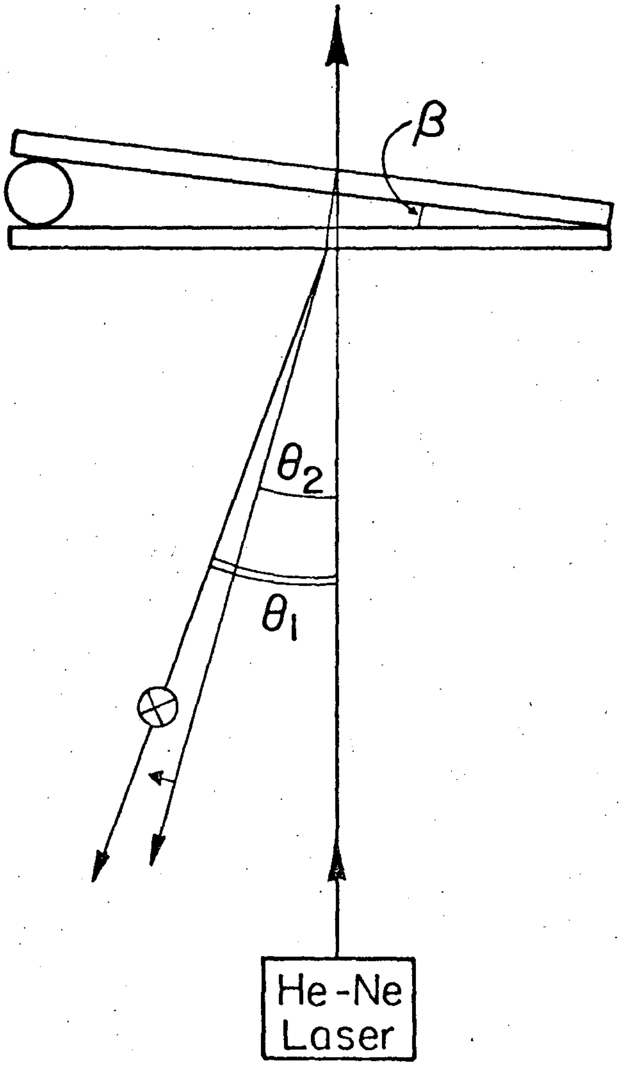

XBL 762-6472

Fig. 1

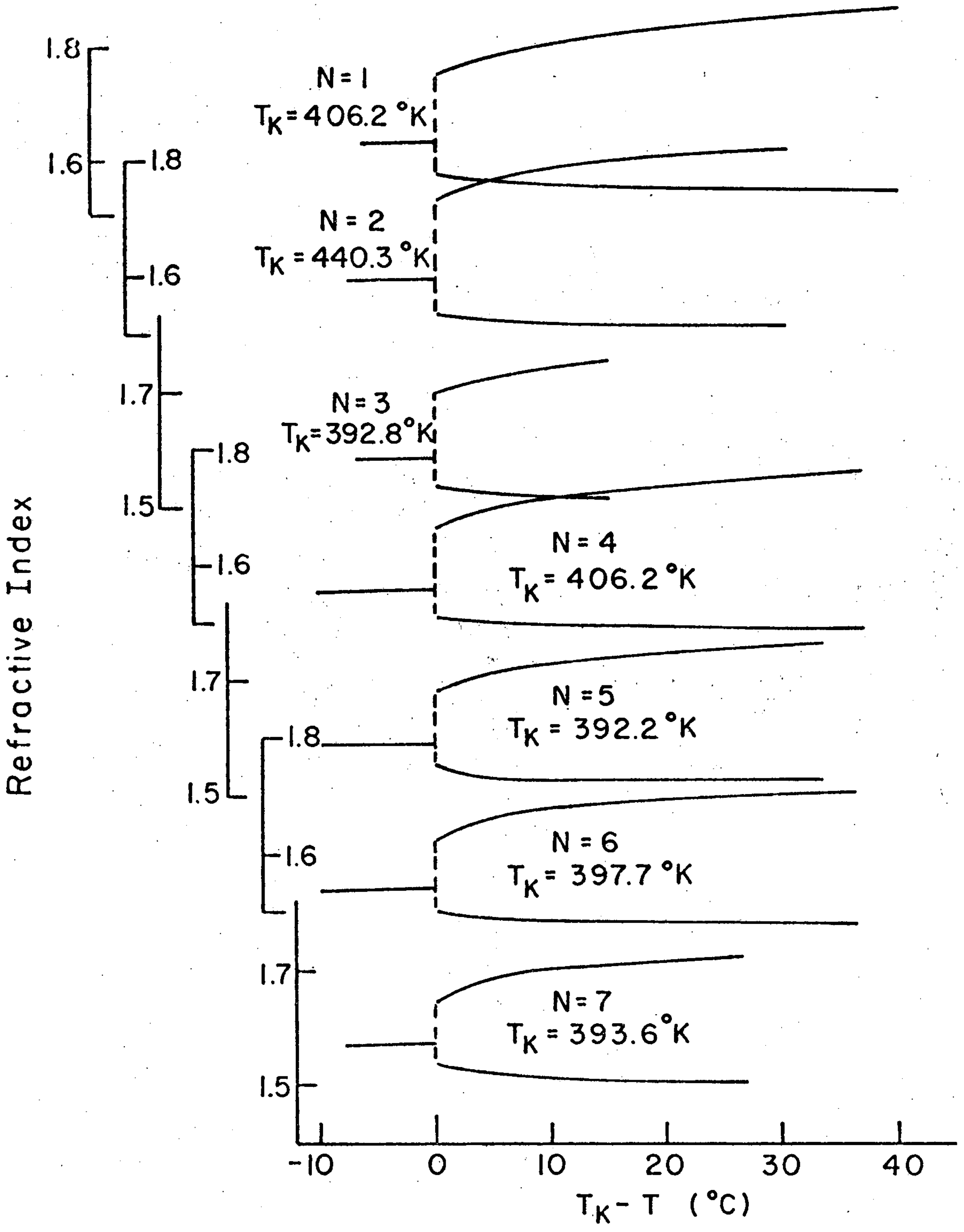

XBL 762-6473

Fig. 2

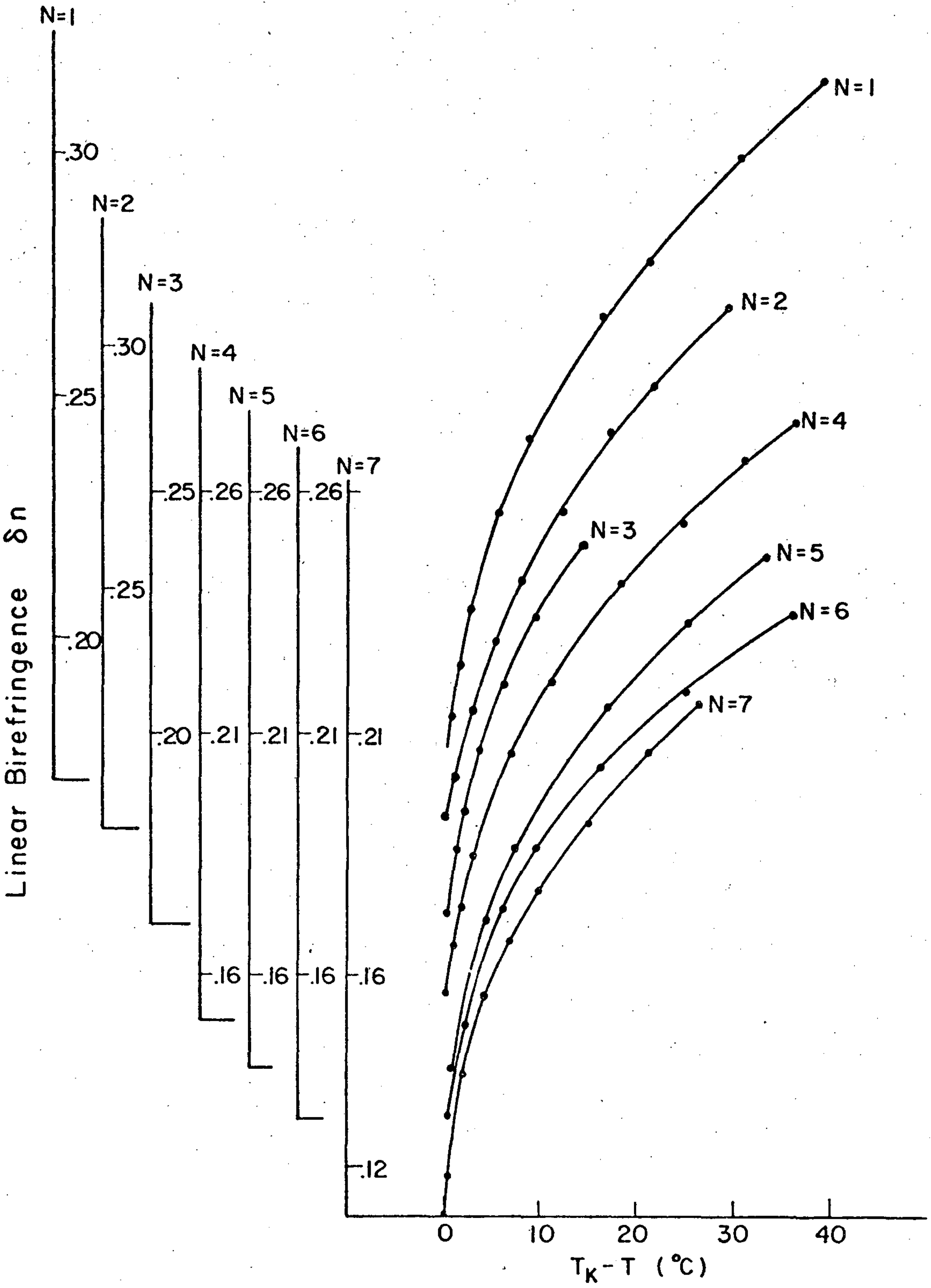

XBL762-6474

Fig. 3

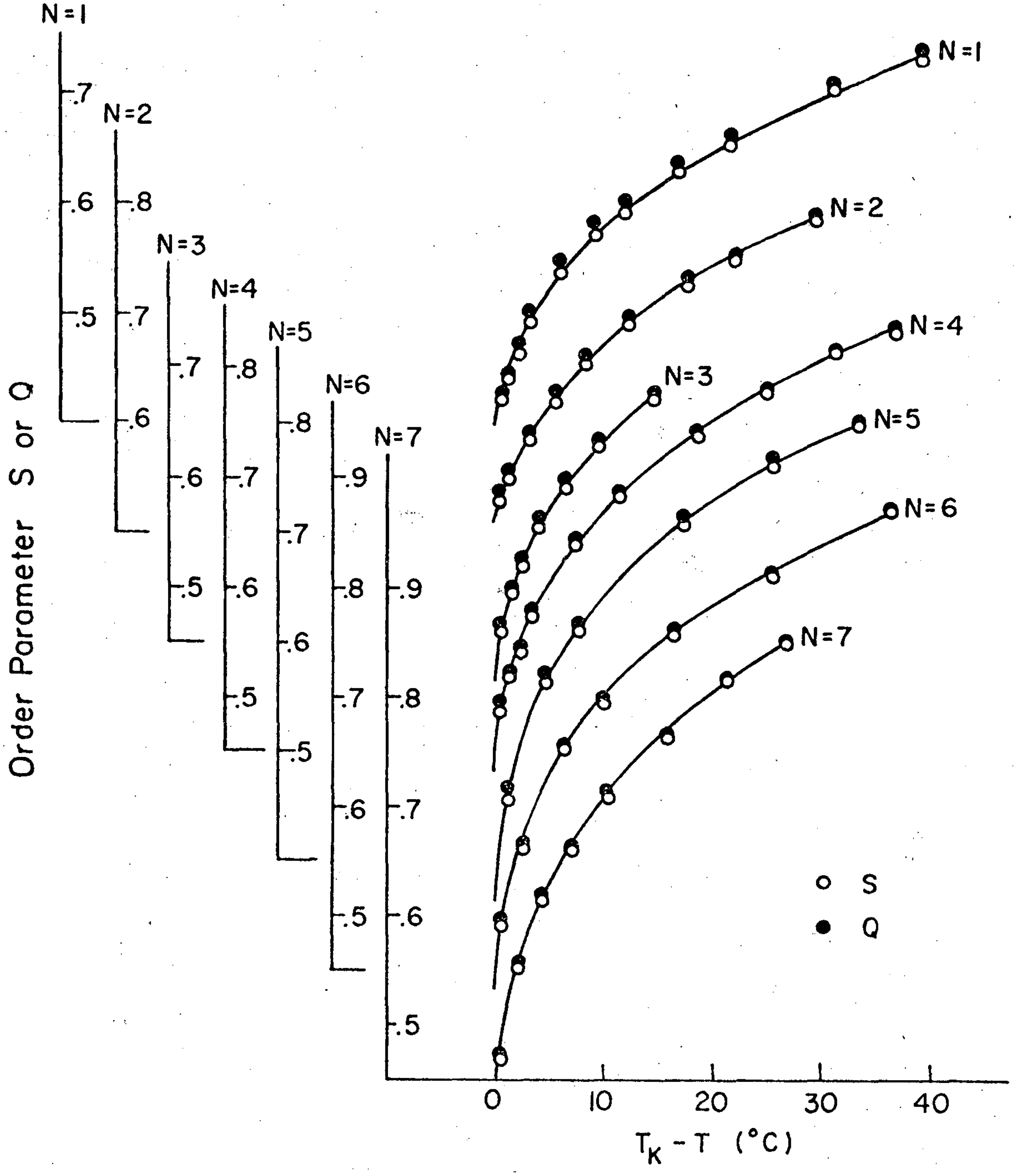

XBL 762-6475

Fig. 4

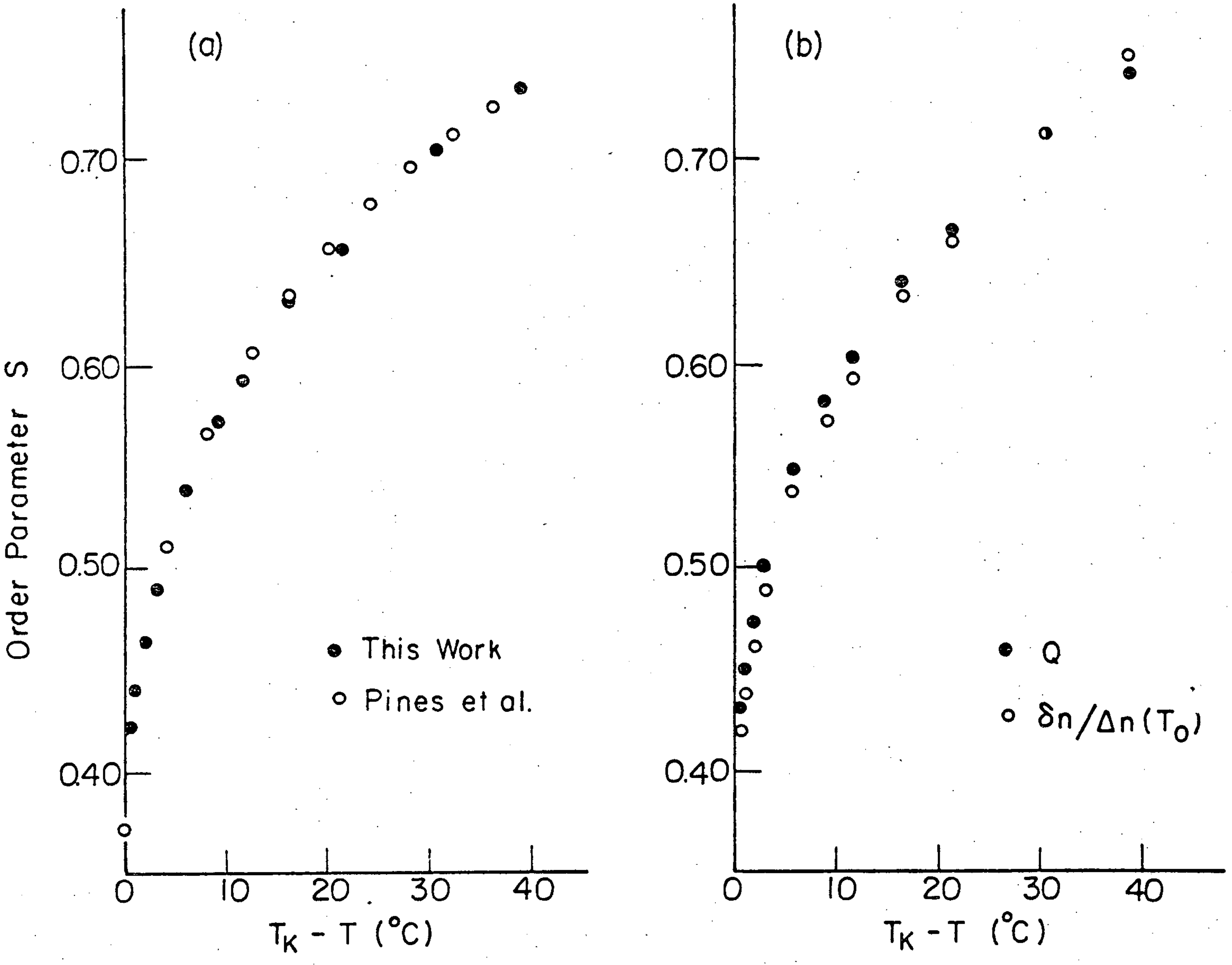

XBL 762-6476

Fig. 5

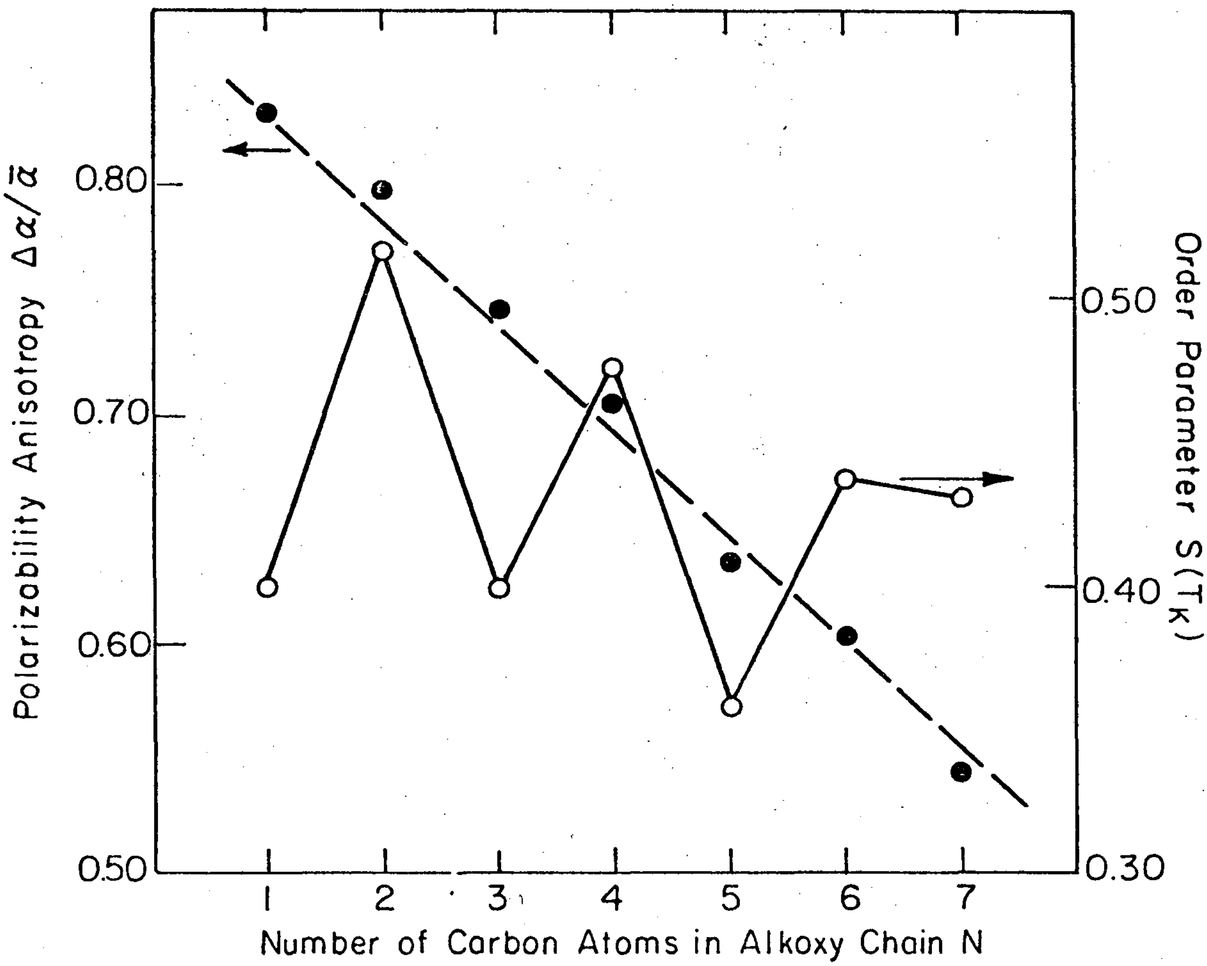

XBL 762-6477

Fig. 6

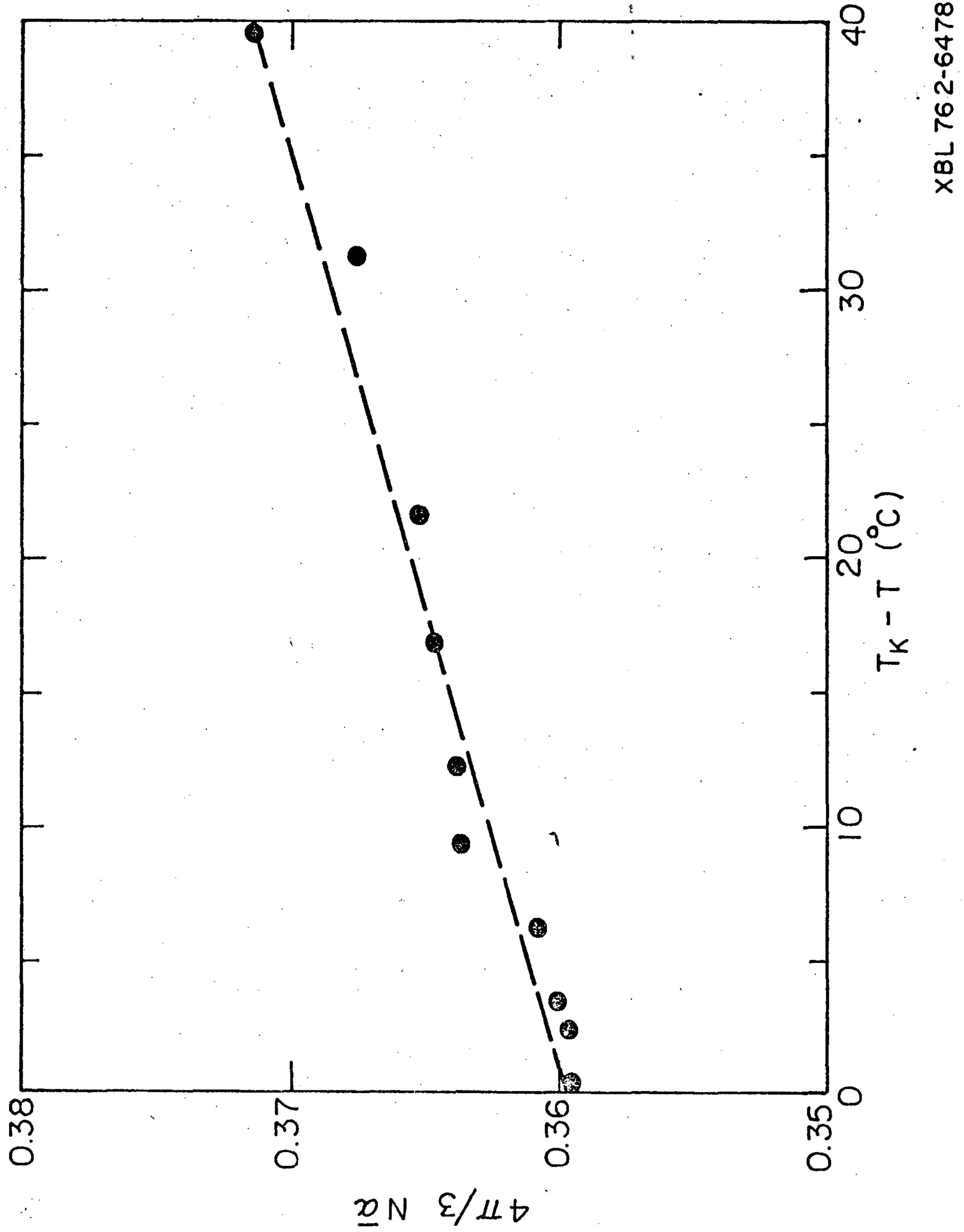

Fig. 7

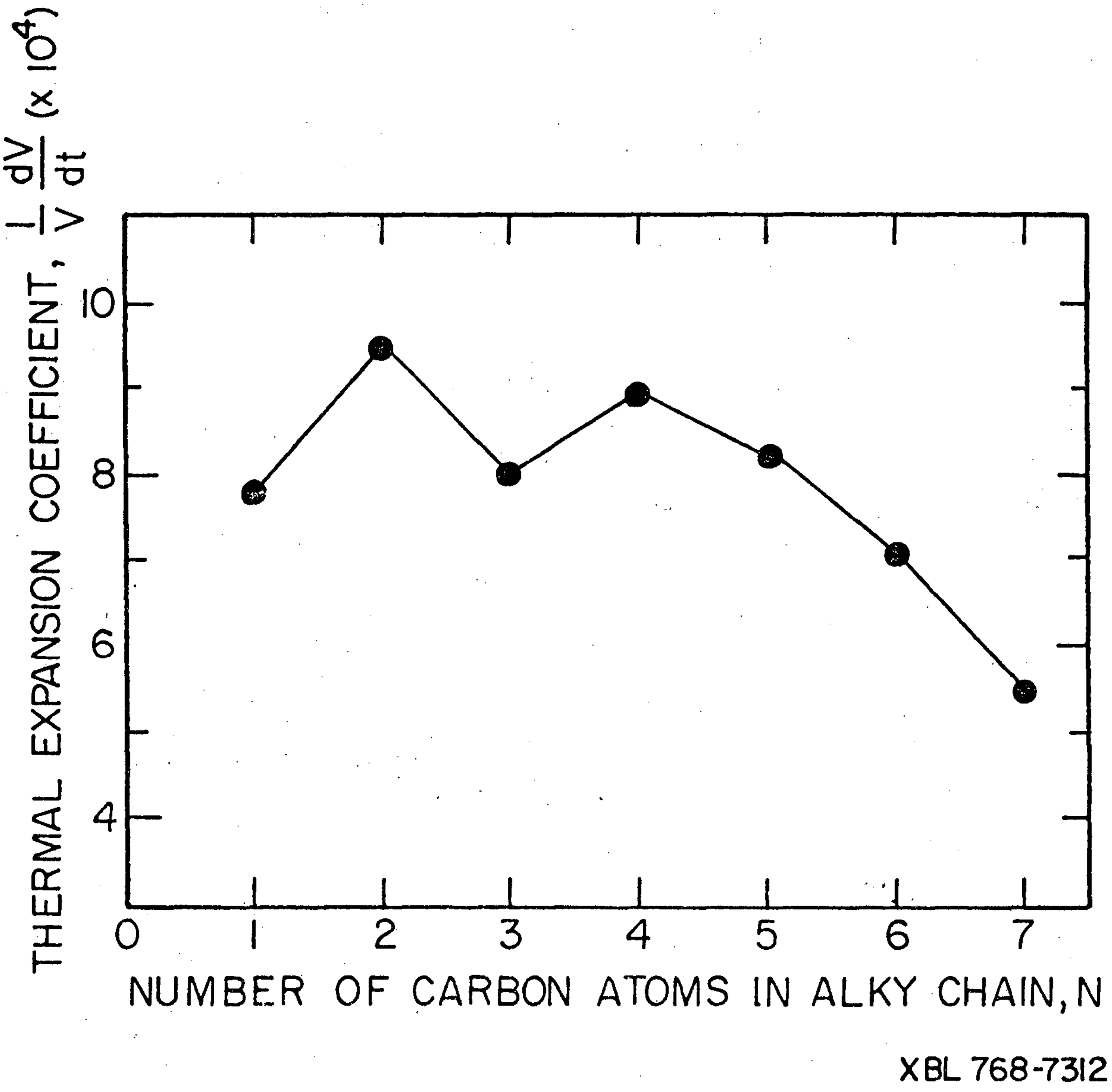
THERMAL EXPANSION COEFFICIENT, $\frac{1}{V}\frac{dV}{dt}$ (x 10^4)
10
8
6
4
0
1
2
3
4
5
6
7
NUMBER OF CARBON ATOMS IN ALKY CHAIN, N
XBL 768-7312

Fig. 8

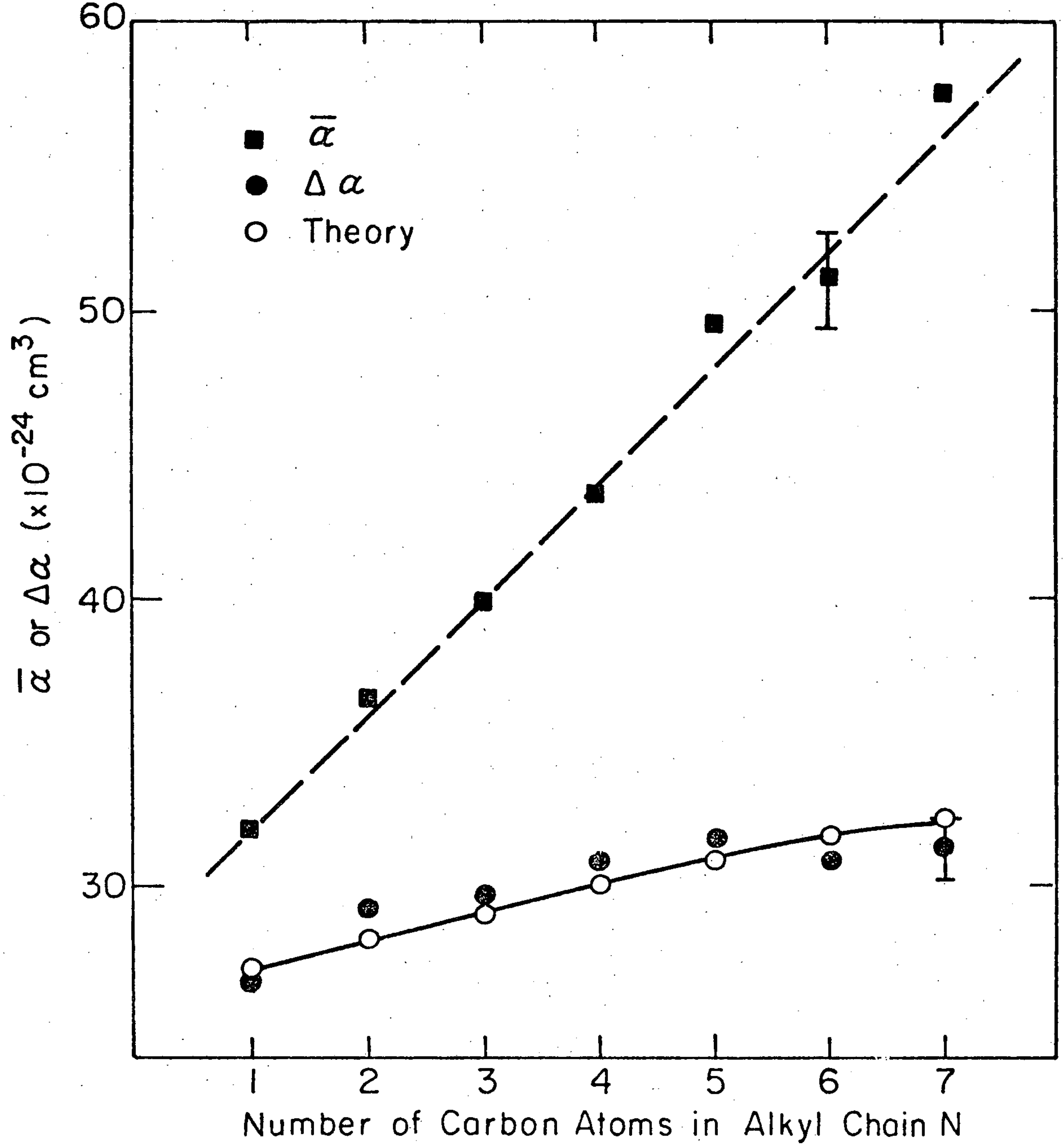

XBL 762-6479

Fig. 9

IV. SELF-FOCUSING: FROM TRANSIENT TO QUASI-STEADY-STATE

1. INTRODUCTION

Self-focusing of light is one of the most complex and interesting phenomena in nonlinear optics.[1] It is of central importance in the design of high-power laser amplifiers because of its role in possible laser-induced damages. It is of fundamental interest as well because of its interplay with many other nonlinear optical processes.

While many physical aspects of self-focusing are now well understood, a number of important questions still remain, namely, the detailed dynamics of focusing, the limiting focusing diameter, polarization properties, etc. In particular, it is not clear how the self-focusing behavior changes in accordance with the variation in the laser pulsewidth t_p, relative to the response time τ of the induced refractive index in the medium.

When $t_p >> \tau$, in the so-called quasi-steady-state limit, the moving focus model[2] describes the self-focusing behavior very well. This model was first suggested by Lugovoi and co-workers,[2] who realized that a self-focused beam leads to one or more sharp focal spots which move along the beam axis as the beam power varies during a laser pulse. The model actually follows closely the earlier theoretical calculation of steady-state self-focusing. Experiments performed with well-controlled, single transverse mode lasers have confirmed the predictions of the calculations. The motion of the focal spot has been observed by time of flight measurements,[4,5] and has been photographed directly with a streak camera.[6] It explains the observed backward-forward asymmetry in stimulated Raman scattering[7,8] and the time dependence of the stimulated Raman and Brillouin pulses under various self-focusing conditions.[8,9] In addition, it explains quantitatively the spectral broadening of the self-focused beam resulting from self-phase modulation.[10,11] Measurements of the self-focusing dynamics in the prefocal region[12] also agree well with the theoretical calculations.[13,14]

When $\tau >> t_p$, transient response of the medium dominates the self-focusing behavior. Focusing becomes much more gradual and no sharp focal spot is formed. Transient self-focusing was first discussed by Akhmanov et al.[15] It was shown that as the laser pulse propagates on in the nonlinear medium, the beam radius would first deform into a horn shape (see Sec. II B) and then retains the shape over long distances. This is known as dynamic trapping. Numerical calculations yield this same picture,[16-18] although they suggested that the neck of the horn might continue to shrink in radius as the pulse propagates on and may even form singularities.[19] This dynamic trapping model of transient self-focusing has been used to semi-quantitatively account for the observed assymmetric semi-periodic spectral broadening of the laser light.[8,20] Experiments using an isotropic liquid crystalline material with a long relaxation time τ as the nonlinear medium have been performed to study this extreme transient self-focusing [21] and have confirmed the theoretical predictions. It has been shown that the pulse does deform into a horn shape. The diameter of the neck of the horn first decreases almost exponentially with increasing input power, as predicted,[18] and then approaches a constant when some limiting nonlinear process sets in.

As is described above, the dynamic trapping model for transient self-focusing ($t_p << \tau$), and the moving focus model for quasi-steady-state self-focusing, ($t_p >> \tau$) appear to be very different physically. It is therefore interesting to know how self-focusing would vary as t_p/τ is varied from one limit to the other. This has not been studied either experimentally or theoretically. Experimentally, difficulty comes in the choice of a suitable nonlinear medium with τ variable over a wide range or a laser with a variable t_p. While the former seems easier, in order to quantitatively measure the time dependence of the focusing, a laser pulse with t_p of the order of 10 nsec or longer must be used, as limited by the response time of ordinary detection systems. These constraints rule out the use of conventional Kerr liquids, for which τ is in the 1-100 psec range.

We have found recently that a nematic liquid crystal in the isotropic phase can have a τ variable from $\sim$ 1 nsec to > 100 nsec depending on the temperature.[22,23] Such a medium also has a large nonlinearity in which self-focusing of a Q-switched laser pulse readily occurs. We therefore have on hand a perfect medium we can use to study the entire range of self-focusing from the quasi-steady-state to the transient limit. In this paper, we discuss in quantitative detail our recent measurements of self-focusing in a liquid crystalline medium with t_p/τ varied from << 1 to >> 1.

Section 2 gives a brief review of the theory and physical description of self-focusing under different conditions. Section 3 summarizes our experimental techniques, data analysis and results. Section 4 shows how our experimental results agree with a qualitative united physical description of self-focusing in all cases. We also identify the mechanism responsible for the limiting focal diameter in our sample.

2. THEORY

A. General Formalism

Consider a medium with a refractive index $n = n_o + \delta n(|E|^2)$, where δn is the part induced by the optical field E. This induced δn leads to self-focusing which is governed by the wave equation[1]

$$\nabla^2 E - \frac{1}{c^2}\frac{\partial^2}{\partial t^2}[(n_o + \delta n)E] = 0. \qquad (1)$$

For a quasi-monochromatic light beam we can write

$$E = A(r,z,\zeta)\exp[ikz - i\omega t + iks(r,z,\zeta)] \qquad (2)$$

where $\zeta \equiv t - zn_o/c$ is the reduced time, and A and s are respectively the amplitude and the eikonal (or phase function) of the wave. We can convert Eq. (1) into two coupled equations

$$\frac{\partial A}{\partial z} + \left(\frac{\partial s}{\partial r}\right)\left(\frac{\partial A}{\partial r}\right) + \frac{A}{2}\left(\frac{\partial^2 s}{\partial r^2} + \frac{1}{r}\frac{\partial s}{\partial r}\right) = 0 \qquad (3a)$$

$$2k\left(\frac{\partial s}{\partial z}\right) + \left(\frac{\partial s}{\partial r}\right)^2 = 2\frac{\delta n}{n_o} + \frac{1}{A}\left(\frac{\partial^2 A}{\partial r^2} + \frac{1}{r}\frac{\partial A}{\partial r}\right). \qquad (3b)$$

In order to solve these equations, we need to know the amplitude and phase profile of the input laser pulse. We also need to know the functional dependence of δn upon the field. For Kerr liquids, the dominant mechanism contributing to δn is molecular reorientation.[15,22-24] It obeys a relaxation equation

$$\left[1 + \tau\frac{\partial}{\partial t}\right]\delta n = n_2|E|^2, \qquad (4)$$

which yields

$$\delta n(t) = \frac{n_2}{\tau} \int_{-\infty}^{t} |E(t')|^2 e^{-(t - t')/\tau} dt, \qquad (5)$$

where n_2 is a constant coefficient of the medium. Then, in the quasi-steady-state limit ($t_p >> \tau$),

$$\delta n(t) = n_2 |E(t)|^2, \qquad (6)$$

and, in the extreme transient limit ($t_p << \tau$),

$$\delta n(t) = \frac{n_2}{\tau} \int_{-\infty}^{t} |E(t')|^2 dt'. \qquad (7)$$

Self-focusing can now be described by the solution of the coupled equations in Eq. (3) together with Eq. (5). Unfortunately, an analytical solution is not generally possible, so these equations have been solved numerically. In the quasi-steady-state limit, the calculation predicts the appearance of a sharp focal spot at the self-focusing distance[14]

$$z_f(\zeta) = \frac{K}{\sqrt{P(\zeta)} - 0.858 \sqrt{P_{cr}}}, \qquad (8)$$

$$P_{cr} = \frac{(1.22\lambda_o)^2 c_o}{128 n_2}, \qquad (9)$$

where P is the input laser power, λ_o and c_o are the wavelength and the speed of sound in vacuum, $K = 0.369\, ka^2 \sqrt{P_{cr}}$, $k = \omega n_o/c$, and a is the input beam radius. The axial intensity of the self-focused beam is given approximately by

$$I_{ax}(z,\zeta) = I_{ax}(0,\zeta)\left[1 - (z/z_f(\zeta))^2\right]^{-\alpha/2}, \qquad (10)$$

where α is a parameter which depends upon P/P_{cr}.

For the transient case, we can discuss self-focusing using the paraxial approximation. The beam is assumed to have a Gaussian transverse profile and the wavefronts are assumed to be paraboloids[1]

$$A^2(\zeta,r,z) = \frac{A_o^2(z = 0,\zeta)}{f^2(z,\zeta)}\, e^{-(r^2/a^2f^2(z,\zeta))}$$

$$s(\zeta,r,z) = \phi(\zeta,z) + \frac{1}{2}\,\beta(z,\zeta)r^2 \qquad (11)$$

where $f(z,\zeta) = r_o(z,\zeta)/r_o(z = 0,\zeta)$ is the reduced dimensionless radius. From Eqs. (3), (5), and (11), we obtain[15]

$$\frac{1}{f}\frac{\partial^2 f(\zeta)}{\partial z^2} = \frac{1}{k^2a^4f^4(\zeta)} - \frac{n_2}{n_o a^2}\frac{1}{\tau}\int_o^\zeta \frac{A_o^2(\eta)}{f^4(\eta)}\, e^{(\eta - \zeta)/\tau}\, d\eta \qquad (12a)$$

$$\frac{1}{f}\frac{\partial f}{\partial z}(\zeta) = \beta(\zeta) \qquad (12b)$$

$$\frac{\partial\phi(\zeta)}{\partial z} = -\frac{1}{k^2a^2f^2(\zeta)} + \frac{n_2}{2n_o}\frac{1}{\tau}\int_o^\zeta \frac{A_o^2(\eta)}{f^2(\eta)}\, e^{(\eta - \zeta)/\tau}\, d\eta. \qquad (12c)$$

In Eq. (12a), the first term on the right comes from linear diffraction, while the second term is due to self-focusing. In the transient limit, the integral in the second term builds up gradually with time. During the very first part of the pulse, it is so small that the pulse propagation is dominated by linear diffraction. In later parts of the pulse, the integral becomes larger and $\partial^2 f/\partial z^2$ becomes negative. This causes $\partial f(\zeta)/f(\zeta)\partial z$ to become negative, and the beam radius shrinks as the beam propagates on. Towards the end of the pulse, the integral approaches a limiting value, while the linear diffraction term becomes stronger as the propagating beam shrinks in radius. After a certain propagation distance, $\partial f/fdz$ becomes less and less negative and the radius f approaches a minimum value. Thus, the longitudinal spatial profile of the pulse gets deformed into a horn shape as shown in Fig. 1c. The horn-shaped pulse then travels on without appreciable change over approximately a diffraction length $z_d = ka^2$. From Eqs. (11) and (12b), we see that the eikonal should be independent of r in the neck of the horn, where f = constant. This has in fact been observed experimentally.[20] Also, in the transient limit ($t_p << \tau$), Eq. (12) predicts that self-focusing will remain unchanged if n_2/τ remains constant.

The paraxial approximation of Eqs. (11) and (12) does not successfully explain the detailed transient self-focusing behavior. To obtain more exact predictions, Eqs. (3) and (5) have been solved numerically for certain input conditions.[17,20,21] Numerical calculations[16-18] show that aberrations in self-focusing are significant. They also predict that the pulse is deformed into an overall horn shape but with weak oscillation in the beam radius along the neck. Aside from the oscillation, the neck radius r_o^{min}, should remain nearly constant as the pulse propagates over a distance $z << z_d$, but r_o^{min} is supposed to be a strong function of P/P_{cr} and t_p/τ.

B. Physical Description

We have so far described self-focusing in the quasi-steady-state limit and in the transient limit in rather different physical terms. However, in varying from one limit to the other, we should expect the self-focusing behavior to change continuously. We therefore need a unified physical description to describe self-focusing throughout the entire range.

In our unified description, we concentrate on how the beam radius of different parts of the laser pulse varies as a function of distance as the pulse propagates in the medium. In the quasi-steady-state limit, self-focusing and subsequent diffraction are both abrupt. Thus, each small section of the incoming laser pulse self-focuses into a sharp focal spot at the self-focusing distance z_f given by Eq. (5). We can then sketch in Fig. (1a) the evolution of the beam radius and hence the longitudinal pulse profile along the cell. The pulse enters the sample from the left. The radius of each consecutive section of the pulse (A - A, B - B, etc.) follows a different trajectory and reaches a sharp minimum at $z_f(P)$ according to its instantaneous power $P(\zeta)$. For $\ell > (z_f)_{min}$, there should be two focal spots simultaneously present on the beam axis. In practice, the second focal spot is usually prevented from forming by depletion of incoming laser power by backward stimulated Raman and Brillouin scattering initiated earlier by the first focal spot.[8] We expect the longitudinal dimension of the focal spot to be about $\Delta\zeta = \tau$.

We can similarly sketch the evolution of the beam radius and longitudinal pulse profile for the transient limit. Note however that self-focusing is now much more gradual and diffraction extremely slow because of the transient response of the medium. According to the description in Sec. II A, the front part of the pulse hardly self-focuses while the lagging part of the pulse self-focuses gradually to a limiting diameter. Then as shown in Fig. 1c, the incoming pulse first gets deformed into a horn shape and then propagates on without much further change.

Now, for the intermediate range of self-focusing, we should expect the self-focusing and diffraction trajectory to be intermediate between the two limiting cases. Both self-focusing and diffraction are less abrupt than the quasi-steady-state case but also less gradual then the transient limiting case. The middle part of the pulse sees the largest Δn and self-focuses most strongly, while both the front and the lagging parts of the pulse do not self-focus very much. Following the above description for the beam trajectory of different parts of the laser pulse, we can then sketch again the evolution of the pulse profile for the intermediate case as shown in Fig. 1b. The sketches in Fig. 1 show that the evolution of the pulse profile will indeed change continuously as self-focusing is varied from the quasi-steady-state to the transient limit.

C. Effect of Other Nonlinear Processes on the Limiting Diameter

As the input laser power is increased, the theories discussed in Section 2 A would predict that the minimum diameter of the self-focused beam should continually become smaller. Experiments however find a limiting diameter which appears to be a characteristic of the nonlinear medium.[1]

Numerous explanations have been proposed for this limiting diameter.[14,25-32] They generally assume either saturation of Δn or depletion of the laser beam.[1] While the pre-breakdown ionization[29] which creates free electrons to reduce Δn may be the domination mechanism for limiting the focal diameter in self-focusing of picosecond pulses, stimulated Raman and Brillouin scattering appears to be the most possible mechanism for the cases of longer pulses. A large fraction of the incoming laser power can be depleted by stimulated Raman and Brillouin scattering during self-focusing so that the self-focusing strength is limited. The limiting focal diameter is presumably the result of balancing between increase of stimulated scattering gain due to self-focusing and decrease of self-focusing strength due to depletion of laser power by stimulated scattering. Rehn and Maier[32] have considered the possibility of forward stimulated Raman scattering as the mechanism for the limiting diameter. Kelley and Gustafson[31] have considered backward stimulated scattering. However, in either case, no serious calculation in connection with the real physical problems has been carried out.

3. EXPERIMENT

Our experiment was designed to check the predictions of the unified physical description of self-focusing discussed in the previous section. We wanted to obtain the results quantitatively so that the data can be used to compare with available or possible numerical calculations.

We used the response time τ of the medium as a varying parameter to vary self-focusing from the quasi-steady-state limit to the transient limit. In order to compare our results with the sketches in Fig. 1, we should have measured the beam radius $r_o(z,\zeta)$ defined, for example, as

$$r_o(z,\zeta) = \left[P(\zeta)/\pi\ I_{ax}(z,\zeta)\right]^{\frac{1}{2}} \qquad (13)$$

for a given input laser pulse of power P(t). (For a Gaussian beam, $r_o(z,\zeta)$ defined in Eq. (3) is the beam radius at the 1/e points.) However, this is not practically feasible. Instead, we varied the input peak power P_o and measured $r_o(z = \ell,\zeta)$ at the end of the sample. Examination of the self-focusing equation in Sec. II A shows that the evolution of $r_o(z = \ell,\zeta)$ with increasing peak input power should appear qualitatively the same as the evolution of $r_o(z,\zeta)$ along z with constant P_o.

A. The Nonlinear Medium

We used the liquid crystalline material p-ethoxy-benzylidene-p-butylaniline (EBBA) in its isotropic liquid phase as our self-focusing medium. This material is known to have a large nonlinear refractive index and a long relaxation time.[22] In addition, both n_2 and τ have a strong pretransitional temperature dependence in the range above the nematic-isotropic transition temperature T_K. They can be written as[22]

$$n_2 = \frac{6.35 \times 10^{-9} \text{ esu °K}}{(T - T^*)}$$

$$\tau = \frac{e^{2800° \text{ K}/T}\ 7.0 \times 10^{-11} \text{nsec - °K}}{(T - T^*)} \tag{14}$$

where $T^* = T_K - 1.0°$ K is a ficticious second-order transition temperature. Over the temperature range we used, n_2 varied by a factor of 20, while τ varied by a factor of 50 (see Table I).

We used in our self-focusing experiment EBBA purchased from Varilight Corporation without further purification. The sample was placed in a 10-cm fused-quartz optical cell, and evacuated for several hours to remove any H_2O or O_2. After evacuation, the cell was sealed under vacuum. The sample then had a sharp isotropic-nematic transition at $T_K = 78.0°$ C. This T_K was constant to within 0.1° C throughout the experiment, indicating that no degradation of the sample had occured. In our experiment, the sample cell was held inside an oven which had a temperature stability of better than 0.1° C, and a uniformity of better than 0.2° C throughout the cell.

B. Experimental Technique

These experiments were performed with a ruby laser, Q-switched by cryptocyanine in methanol, which gave a smooth output pulse having a duration approximately 15 nsec full width at half maximum. Oscillation on a single transverse mode was insured by placing an 0.8 mm diameter pinhole in the laser cavity. The laser power was varied using neutral density filters outside the cavity. After collimation by lenses L1 and L2 (see Fig. 2) the beam entered the sample with a 1/e intensity radius of 130 μm. The time dependence of the input power was monitored by D2 (ITT-F4018 biplanar vacuum photodiode) and by Scope A (Tek. 519).

After the beam excited the sample cell, measurements were made on it to observe the effects of self-focusing. First, a magnified image of the exit plane of the sample was formed using imaging lenses, and the actual measurements were performed on the magnified image. An image of any plane inside the sample would be distorted by gradients in Δn inside the sample. This is the reason we made all measurements at (z = constant).

To obtain the most complete information, we made three different measurements simultaneously, each using a separate magnified image of the exit plane of the sample. The first image was formed on a ground glass plane by light passing through lenses L3 and L4. This image had a magnification of 85 × and a resolution corresponding to 5 μm in the exit plane of the sample. This image was photographed with the streak camera (TRW model 1D Image Converter Camera, with model 7B streaking plug-in) at a streak rate of 1 ns/mm. The camera magnification was 0.5 ×. The camera was triggered by an electrical pulse from D - 1 (ITT-F4000 photodiode). Because of the triggering delay of the streak camera electronics, a fixed optical delay line (27.5 meters) was used before the streak camera. The reference monitor pulse from the streaking plug-in was displayed on scope A to monitor the exact time delay before initiation of the streak for each laser shot. This was necessary, as the jitter in the delay time was of the order of 10 nsec.

The second image was formed on the plane of the pinhole P1 with light reflected by beamsplitter B4 (reflectivity = 50%). This image, formed by lenses L3 and L5, had a magnification of 71 × and a resolution of better than 5 μm in the exit plane of the sample. The image was centered on the 0.5 mm diameter pinhole, so that light which passed through the pinhole originated in a 7 μm diameter region centered on the beam axis in the exit plane of the sample. This light was detected by D4 (ITT-F4018 photodiode) and displayed on Scope B (Tek 7904, with 7B92 time base and 7A19 vertical amplifier). This oscilloscope was triggered externally by the trigger output pulse from Scope A. In this way, the absolute time delay between signals on Scope A and Scope B could be compared.

The third image (magnification also equal to 71 ×) was formed on the film plane of a camera to monitor the time-integrated laser intensity in the exit plane of the sample. The light for this image was reflected by B4 and B5 (reflectivity = 30%).

Photodiode D3 (ITT-FW114A) monitored the presence of any backward stimulated Brillouin light. Aperture A1 blocked specular reflections from the sample cell windows because the input ruby beam entered the cell at a slight angle to the window normal. A coaxial delay cable delayed the signal from D3 so it appeared after the signal from D4 on Scope B.

C. Data Analysis

To calibrate the absolute power in our laser beam, we used the known self-focusing properties of CS_2, for which $P_{cr} = 8kW$. A 19 cm long CS_2 cell was inserted in place of the EBBA cell, and the radius at the exit plane of the sample was monitored using the techniques discussed above. Then using Eqs. (8), (9), and (10), the absolute value of $P(\zeta)$ was determined.

To calibrate the axial intensity monitored by D4, pinhole P1 was removed, and the signals from D4 and D2 were measured with laser pulses at least ten times below the self-focusing threshold. At the same time, photodiode D3 was calibrated by removing aperture A1 and allowing the specular reflections from the sample windows to enter D3.

Knowing the calibrations, we could determine the absolute stimulated Brillouin power generated in the backward direction for each laser shot. We could also determine the absolute axial intensity at the exit plane of the sample $I_{ax}(\zeta)$.

Then we could deduce the characteristic radius at the exit plane $r_o(\zeta)$ using

$$r_o^2(\zeta) = P_e(\zeta)/\pi\ I_{ax}(\zeta), \tag{15}$$

where the beam power at the exit plane is

$$P_e(\zeta) = P(\zeta) - P_{SBS}(\zeta). \tag{16}$$

Here Eq. (16) takes account of the depletion of the input power $P(\zeta)$ by the power fed into the Brillouin scattered beam $P_{SBS}(\zeta)$ if any. Eq. (15) will provide a useful characteristic radius unless the stimulated Brillouin scattering is so strong that it substantially changes the transverse profile of the beam. In our experiment, such substantial changes in the beam profile occured only at the very highest input powers used.

If the transverse profile of the beam is Gaussian, then from Eq. (15), we have

$$I(r,\zeta) = I_{ax}(\zeta)\, e^{-r^2/r_o^2(\zeta)} . \tag{17}$$

In our analysis, we assumed the profile was Gaussian, and used Eq. (17) to compare our measurements of $I_{ax}(\zeta)$ to the streak photographs and the time-integrated photographs. We found good agreement, except for those cases having very strong stimulated Brillouin scattering. This was not surprising. It is known that the number of focal spots observed at the exit plane of a self-focusing sample is very sensitive to the spatial mode structure of the laser beam.[4,33] Because we consistently observed only one focal spot, we knew our beam must have a near Gaussian single transverse mode. Transient self-focusing experiments have shown that the focal spots have a near Gaussian profile around their center.[20,34] Calculations for both quasi-steady-state[3] and transient[21] self-focusing show that the off-axis parts of the beam should have more power than would be expected for a Gaussian profile. Thus Eq. (17) may overestimate the power near the axis, and underestimate the power far from the axis. Of course, it will be exactly correct for the power right on the axis.

D. Results

We made a series of measurements with different input laser powers for five values of t_p/τ listed in Table I. In Fig. 3, we present a typical set of results showing self-focusing for three clearly different cases: (I) near quasi-steady-state limit, $t_p/\tau = 11.3$; (II) the intermediate case, $t_p/\tau = 5.2$; and (III) near transient limit, $t_p/\tau = 0.21$. Figures 3(a) and 3(b) show respectively the input laser pulses $P(\zeta)$ and the axial intensity pulses $I_{ax}(\zeta)$, measured by the fast detectors D2 and D4 in Fig. 2. Each pulse is plotted with its leading edge at the right. Using Eq. (15) we could deduce the temporal variation of the beam radius $r_o(\zeta)$

at the end of the cell as shown in Fig. 3(d), and compared it directly with the observed streak camera picture in Fig. 3(e). We found the agreement in all cases was excellent. Note however that in the near quasi-steady-state case, only the leading part of the pulse can be seen because backward stimulated Brillouin scattering actually depletes the lagging part of the pulse and prevents it from self-focusing.

We present more extensive results showing $I_{ax}(\zeta)$ for a wide range of input laser powers in Fig. 4. For these same input powers, we show $r_o(\zeta)$ in Fig. 5 as determined from Eq. (15). Of all these shots, the peak of the axial intensity was substantially depleted by Brillouin scattering in only two shots, (c)(v) and (d)(v). This depletion caused Eq. (15) to give a minimum $r_o(\zeta)$ which was about 30% larger than the minimum $r_o(\zeta)$ which was deduced from the streak photograph. For these two shots only, the $r_o(\zeta)$ shown in Fig. 5 is deduced from the streak photograph rather than from Eq. (15). In Fig. 6 we show the corresponding streak photographs.

4. DISCUSSION

A. Agreement with Theoretical Models

The radial profiles of the self-focused laser pulse in Fig. 3(c) can now be compared with those in Fig. 1. They clearly have the same qualitative features, which shows that our unified physical description in Fig. 1 is a valid description. In the transient limit the pulse had a horn shape with weak oscillations along the neck region, as predicted by the theory.[17,18] As t_p/τ was increased by decreasing τ, the axial intensity pulse decreased in length, and the radius started to diverge at the end of the pulse. In the quasi-steady-state limit ($t_p/\tau >> 1$) the radius showed a localized focal spot, and the axial intensity pulse length was of the order of τ, in agreement with theoretical predictions.[11]

We can see the effect of varying input power in Fig. 5. The deformation of the longitudinal pulse profile is strikingly dependent on t_p/τ at all power levels investigated. As an example, let us examine the pulse deformation right at the self-focusing threshold. These low input power pulses are shown in Fig. 5(i). In the quasi-steady-state limit (see Fig. 5a(i)), the tail of the pulse was focused no more strongly than was the leading edge of the pulse. The peak of the pulse was focused most strongly, and $r_o(\zeta)$ was nearly symmetrical about $\zeta = 0$. As t_p/τ decreased (see Fig. 5b(i) and 5c(i)), the tail of the pulse was affected more and more by the onset of self-focusing. In the transient limit (see Fig. 5d(i)), the tail of the pulse was focused more strongly than any preceding part of the pulse. This behavior is in good agreement with the predictions of Fig. 1.

Another qualitative aspect of self-focusing one can deduce from Fig. 1 is that near the self-focusing threshold, the peak of the axial intensity pulse should be delayed from the peak of the input laser pulse if the transient effect is appreciable. For the transient cases, the self-focusing threshold is higher and the delay is longer. As the input power increases and the beam self-focuses more strongly, the peak of the axial intensity pulse will first move backward in time until the self-focused beam reaches its limiting diameter, and then it will move forward toward the peak of the input pulse. These features are what we actually observed in our experiment as shown in Fig. 7. For comparison, we include in Fig. 7 a theoretical curve (a) calculated using the quasi-steady-state formula Eq. (8) with the actual time dependence of the laser pulses we used in these measurements. The results in Fig. 7 indicate that even with $t_p/\tau = 11.3$, the transient effect on self-focusing is still quite appreciable. For the more transient cases, the delay of the axial intensity pulse approached $\zeta_o \cong 0.3\ t_p$. This is in good agreement with the delay predicted in numerical calculations.[17,18]

In Fig. 8, we show the observed minimum radius of the self-focused beam at the end of the cell $R_{min} \equiv r_{o,min}/r_{o,input}$ as a function of the normalized input peak power P/P_{cr} for the various cases. The theoretical curve (a) for the quasi-steady-state limit is also plotted for comparison.[14] Curve (b) shows again that with $t_p/\tau = 11.3$, self-focusing is still somewhat transient. For the more transient cases, the minimum radius R_{min} of the self-focused beam shrank more gradually with increasing input power. Towards the transient limit, curves (e) and (f), R_{min} depended only on the quantity$(Pt_p/P_{cr}\tau)$, as predicted by theory.[18,19] Points of equal R_{min} on curves (e) and (f) occur at powers P/P_{cr} differing by a factor equal to the ratio of τ for the two curves. Curves (g) and (h) in Fig. 8 show the theoretical predictions for $t_p/\tau = 0.47$ and $t_p/\tau = 0.21$, based upon interpolation of the numerical results of Shimizu.[21] Presumably because of the onset of stimulated Brillouin scattering, our results deviate from the theoretical predictions as the limiting diameter is reached.

In Fig. 9, we show R_{min} as a function of P/P_{cr} for CS_2, which has a response time $\tau = 2$ sec. With $t_p/\tau = 7.5 \times 10^3$, this is the true quasi-steady-state limiting case. As expected, the solid theoretical curve for the quasi-steady-state limit agrees well with our experimental results down to the limiting value.

B. Limiting Mechanisms

In all cases, the R_{min} in Fig. 8 approached a limiting value at high P. As discussed in Section II, numerous mechanisms have been proposed for this behavior. Here, let us estimate the effects of some of these mechanisms.

The limiting focal diameter could be due to saturation of Δn resulting from high degrees of molecular alignment in a Kerr liquid. In our experiments, however, we estimated the maximum Δn using Eqs. (5) and (15) and the measured axial intensities in Fig. 4. We found $\Delta n_{max} \cong .007$. For fully aligned EBBA with an order parameter of unity, Δn should be around 0.35. So, the maximum ordering in our sample is only 0.02. This is more than an order of magnitude less than the ordering present in the nematic phase, and is therefore far from saturation. From the known results on the optical field-induced refractive index in EBBA,[22] there should also be no steric or compressional effects[28] which could introduce saturation in Δn at our level of laser intensities.

Another possible mechanism of limiting the focal diameter is the generation of free electrons in pre-breakdown ionization.[29] This would require an electron density of $n \cong mc^2 I_{ax}/e^2 P_{cr}$ so that the plasma frequency is $\omega_p \simeq \omega \left[n_o n_2 |E|^2\right]^{\frac{1}{2}}$. The total required number of free electrons for an appreciable reduction of Δn would then be $N \cong 5 \times 10^{13} P/P_{cr}$. From Fig. 8, we see that $N \cong 10^{15}$. However, our input pulse contained at most 5×10^{15} photons, and the quantum yield of photons into free electrons was certainly significantly less than 1. It could not create a sufficient electron density to reduce Δn appreciably unless virtually the whole beam were depleted. This means that any effect of pre-breakdown ionization would be from depletion of laser power rather than from its effect upon Δn. In our experiment, we did not see any evidence of depletion of the laser beam below the stimulated Brillouin scattering threshold. As a result the limiting value of R_{min} could not be due to laser depletion from pre-breakdown ionization, or multiphoton absorption.

We have monitored in our experiment stimulated Raman and Brillouin scattering under all conditions. No stimulated Raman scattering was observed until the input power is substantially higher than the level at which the limiting diameter is reached. On the other hand, backward stimulated Brillouin scattering was always observed before the limiting diameter was reached. In Fig. 8, the stimulated Brillouin scattering threshold is marked by an arrow for each set of data. We see that in each case, the limiting value of R_{min} is reached at power slightly above the stimulated Brillouin threshold. We can therefore conclude that in our experiment stimulated Brillouin scattering must be the mechanism responsible for the limiting diameter.

Kelley and Gustafson[31] have pointed out that stimulated Brillouin scattering could not be the limiting mechanism in CS_2 or toluene because its response time was so much longer than the response time of Δn. In our experiment, the situation is different. We can estimate the acoustic response time in EBBA based upon measurements made on other organic liquids. For example, in toluene the response time is 0.3 nsec[35] and in a mixture of cholesteric liquid crystals, it is 0.6 nsec.[36] We infer that in EBBA, this response time should be less than 1 nsec. In our experiment, this means that the orientation relaxation time τ was always greater than the Brillouin response time. As a result, the Brillouin gain can more or less follow the variations of the self-focused laser beam intensity. Since the steady-state gain is higher for Brillouin scattering than for Raman scattering, we would expect Brillouin scattering to be dominant in our experiment.

In Fig. 8, we see that stimulated Brillouin scattering set in more abruptly in the steady-state case, and thus stopped the shrinking beam radius more readily. For laser pulses well above the Brillouin threshold, we observed Brillouin depletion in excess of half of the beam power. Since the gain is highest on the beam axis, the most intense axial part of the beam was preferentially depleted, and Δn dropped along the beam axis. The light somewhat off the beam axis was much less depleted. So, Δn was higher off of the beam axis than it is on the axis. This should lead to a defocusing of the axial rays. A dynamic equilibrium was expected to set up: any tendency of the beam to further self-focus would result in an increased stimulated Brillouin scattering and the resulting additional depletion of laser power would oppose the tendency of the beam to further self-focus.

In Fig. 10, we show the variation of the peak Brillouin output power as a function of input power for the cases studied. Again, we see that the growth of the Brillouin power is clearly the most abrupt in the most steady-state case as expected.

5. CONCLUSION

Using the temperature dependence of the relaxation time τ in an isotropic liquid crystalline material, we have studied the variation of self-focusing from the quasi-steady-state to the transient limits. In all cases, our quantitative measurements of the time variation of the laser pulse radius strongly support the unified qualitative description of self-focusing in Fig. 1. We see that there is no abrupt change in the character of the self-focusing as t_p/τ is varied, but rather there is a smooth variation from one limit to the other. Our measurements are in good qualitative agreement with available theoretical predictions. Unfortunately, because numerical calculations of self-focusing for our cases do not exist at present, we have not yet been able to make quantitative comparison between theory and experiment over the entire range.

References

1. See, for example, Y. R. Shen, Prog. Quant. Elect. 4, 1 (1975); J. H. Marburger, Prog. Quant. Elect. 4, 35 (1975); O. Svelto, Prog. in Optics XII, 1 (1974); and S. A. Akhmanov, R. V. Khokhlov, and A. P. Sukhorukov, in Laser Handbook, p. 1151 edited by F. T. Arrechi and E. O. Schulz-Dubois, North-Holland Publishing Co. (1972).
2. V. N. Lugovoi and A. M. Prokhorov, Zh. Eksp. Teor. Fiz. Pis'ma 7, 153 (1968) (Translation: JETP Lett. 7, 117 (1968)); A. L. Dyshko, V. N. Lugovoi, and A. M. Prokhorov, Zh. Eksp. Teor. Fiz. Pis'ma 6, 665 (1967) (Translation: JETP Lett. 6, 146 (1967)); V. N. Lugovoi, Doklady Akad. Nauk SSSR 176, 58 (1967) (Translation: Sov. Phys. Doklady 12, 866 (1968)).
3. P. L. Kelley, Phys. Rev. Lett. 15, 1005 (1965); V. I. Talanov, Zh. ETF Pis'ma 2, 218 (1965) (Translation: JETP Lett. 2, 138 (1965)); S. A. Akhmanov, A. P. Sukhhorukov, and R. V. Khokhlov, Zh. Eksp. Teor. Fiz. 50, 1537 (1966) (Translation: Sov. Phys. JETP 23, 1025 (1966)).
4. M. M. T. Loy and Y. R. Shen, Phys. Rev. Lett. 22, 994 (1969).
5. M. M. T. Loy and Y. R. Shen, Phys. Rev. Lett. 25, 1333 (1970); M. M. T. Loy and Y. R. Shen, Appl. Phys. Lett. 19, 285 (1971).
6. V. V. Korobkin, A. M. Prokhorov, R. V. Serov, and M. Ya. Shchelev, Zh. ETF Pis'ma 11, 153 (1970) (Translation: JETP Lett. 11, 94 (1970)).
7. M. Maier, W. Kaiser, and J. A. Giordmaine, Phys. Rev. Lett. 17, 1275 (1966); Phys. Rev. 177, 580 (1969).
8. M. M. T. Loy and Y. R. Shen, IEEEJ Quant. Electron. QE-9, 409 (1973).
9. M. Maier, G. Wendl, and W. Kaiser, Phys. Rev. Lett. 24, 352 (1970); M. Maier, O. Rehn, and G. Wendl, Z. Naturforsh. A25, 1868 (1970).

10. G. K. L. Wong and Y. R. Shen, Appl. Phys. Lett. 21, 163 (1972).

11. Y. R. Shen and M. M. T. Loy, Phys. Rev. A3, 2099 (1971).

12. G. McAllister, J. Marburger, and L. De Shazer, Phys. Rev. Lett. 21, 1648 (1968).

13. V. N. Goldberg, V. I. Talanov, and R. E. Irm, Izv. Vysshikh. Uchebn. Zavedenii Radiofizika 10, 674 (1967).

14. J. H. Marburger and E. L. Dawes, Phys. Rev. Lett. 21, 556 (1968); E. L. Dawes and J. H. Marburger, Phys. Rev. 179, 862 (1969).

15. S. A. Akhmanov, A. P. Sukhorukov, and R. V. Khoklov, Zh. Eksp. Tech. Fiz. 51, 296 (1966) (Translation: JETP 24, 198 (1966)).

16. J. A. Fleck and P. L. Kelley, Appl. Phys. Lett. 15, 313 (1969).

17. J. A. Fleck and R. L. Carman, Appl. Phys. Lett. 20, 290 (1972).

18. F. Shimizu, IBM J. Res. Develop. 17, 286 (1973).

19. V. A. Aleshkevich, S. A. Akhmanov, A. P. Sukhorukov, and A. M. Khachatryan, Zh. ETF Pis'ma 13, 55 (1971) (Translation: JETP Lett. 13, 36 (1971)).

20. See, for example, R. Polloni, C. A. Sacchi, and O. Svelto, Phys. Rev. Lett. 23, 690 (1969); R. Cubeddu et al. Phys. Rev. Lett. 26, 1009 (1971).

21. G. K. L. Wong and Y. R. Shen, Phys. Rev. Lett. 32, 527 (1973).

22. G. K. L. Wong and Y. R. Shen, Phys. Rev. Lett. 30, 895 (1973).

23. E. G. Hanson, Y. R. Shen, and G. K. L. Wong, Phys. Rev. A14, 1281 (1976).

24. Y. R. Shen, Phys. Lett. 20, 378 (1966).

25. V. N. Goldberg, V. I. Talanov, and R. E. Irm, Izv. Vysshikh. Uchebn. Zavadenii Radiofizika 10, 674 (1967).

26. W. G. Wagner et al. Phys. Rev. 175, 256 (1968); J. H. Marburger et

al. Phys. Rev. 184, 255 (1969).

27. T. K. Gustafson et al. Appl. Phys. Lett. 12, 165 (1968); T. K. Gustafson et al. Phys. Rev. 177, 306 (1969).
28. T. K. Gustafson and C. H. Townes, Phys. Rev. A6, 1659 (1972).
29. E. Yablonovich and N. Bloembergen, Phys. Rev. Lett. 29, 907 (1972); N. Bloembergen, IEEEJ. Quant. Electr. QE-10, 375 (1974).
30. A. L. Dyshko, V. N. Lugovoi, and A. M. Prokhorov, Zh. Tekh. Fiz. 61, 2305 (1971) (Translation: Sov. Phys. JETP 34, 1235 (1972)).
31. P. L. Kelley and T. K. Gustafson, Phys. Rev. A8, 315 (1973).
32. O. Rehn and M. Maier, Phys. Rev. Lett. 29, 558 (1972); Phys. Rev. A9, 1427 (1974).
33. V. I. Bespalov and V. I. Talanov, Zh. ETF Pis'ma 3, 471 (1966) (Translation: JETP Lett. 3, 307 (1966)).
34. R. G. Brewer and C. H. Lee, Phys. Rev. Lett. 21, 267 (1968).
35. See, for example, Kaiser and Maier in Laser Handbook, vol. 2, p. 1077, edited by F. T. Arecchi and E. O. Schulz-Dobois, North-Holland (1972).
36. H. Rosen and Y. R. Shen, Mol. Cryst, and Liq. Cryst. 18, 285 (1972).

FIGURE CAPTIONS

Fig. 1. Schematic drawing showing how an imput pulse gets deformed through self-focusing (a) in the quasi-steady-state limit, (b) in an intermediate case, and (c) in the transient limit. Here the pulse is shown as viewed from the side in a series of snapshots.

Fig. 2. Experimental arrangement for observing self-focusing. B1, B2, B3, B4, B5, beamsplitters; L1, L2, L3, L4, L5, lenses; D1, D2, D3, D4, biplanar vacuum photodiodes; A1, aperature; P1, pinhole.

Fig. 3. Typical sets of results showing (a) input laser pulses, (b) on-axis intensity pulses, (c) radial profiles of the self-focused pulses, (d) intensity contours of the self-focused pulses, and (e) streak photographs. In each case the horizontal axis is the local time ξ. The intensity contour map shows the intensity as a function of transverse coordinate and time. Contours shown are $I = 0.30\ I_{max}$ and $I = 0.03\ I_{max}$. For $t_p/\tau = 11.3$, the input peak power is $P = 7.9$ kW, $P/P_{cr} = 5.5$, and the on-axis peak intensity is $I_{max} = 0.77\ \mathrm{GW/cm^2}$. For $t_p/\tau = 5.2$: $P = 5.2$ kW, $P/P_{cr} = 5.6$, and $I_{max} = 0.75\ \mathrm{GW/cm^2}$. For $t_p/\tau = 0.21$: $P = 4.4$ kW, $P/P_{cr} = 61$, and $I_{max} \doteq 0.54\ \mathrm{GW/cm^2}$.

Fig. 4. Axial intensity pulses.

(a) $t_p/\tau = 11.3$: (o) input pulse, (i) $P_o = 3.66$ kW, $I_{ax} = 38$ $\mathrm{MW/cm^2}$ (ii) $P_o = 4.42$ kW, $I_{ax} = 75.5\ \mathrm{MW/cm^2}$ (iii) $P_o = 5.17$ kW, $I_{ax} = 431\ \mathrm{MW/cm^2}$ (iv) $P_o = 7.86$ kW, $I_{ax} = 768\ \mathrm{MW/cm^2}$ (v) $P_o = 9.18$ kW, $I_{ax} = 705\ \mathrm{MW/cm^2}$

(b) $t_p/\tau = 5.2$: (o) input pulse, (i) $P_o = 2.58$ kW, $I_{ax} = 28.8$ MW/cm^2
(ii) $P_o = 3.58$ 89.7 (iii) 4.07 304
(iv) 5.17 753 (v) 6.15 864

(c) $t_p/\tau = 2.07$: (i) 1.21 8.0
(ii) 2.27 3.52 (iii) 3.65 481
(iv) 4.33 560 (v) 6.80 348

(d) $t_p/\tau = 0.21$: (i) 0.99 6.4
(ii) 1.93 102 (iii) 2.44 150
(iv) 4.35 544 (v) 7.41 538

Fig. 5. Pulse radius at exit plane of cell, for the same pulses as in Fig. 4.

Fig. 6. Streak photographs, for the same pulses as in Fig. 4.

Fig. 7. Peak position of the on-axis intensity pulse of the self-focused beam as a function of normalized input peak power in different cases: (a) $t_p/\tau \to \infty$, (a theoretical curve), (b) $t_p/\tau = 11.3$, (c) $t_p/\tau = 5.2$, (d) $t_p/\tau = 2.07$, and (e) $t_p/\tau = 0.47$. Curve (a) is calculated from Eq. (8), which gives $z_f = 10$ cm for $P = 2.97$ P_{cr}.

Fig. 8. Reduced minimum radius of the self-focused beam at the end of the cell as a function of normalized input peak power in various cases: (a) $t_p/\tau \to \infty$ (a theoretical curve from Ref. 13), (b) $t_p/\tau = 11.3$, (c) $t_p/\tau = 5.2$, (d) $t_p/\tau = 2.07$, (e) $t_p/\tau = 0.47$, (f) $t_p/\tau = 0.21$, (g) $t_p/\tau = 0.47$ (a theoretical curve from Ref. 21), and (h) $t_p/\tau = 0.21$ (a theoretical curve from ref. 21).

Fig. 9. Reduced minimum radius of the self-focused beam at the end of the cell as a function of normalized input peak power for CS_2. Here the solid curve is calculated from Eqs. (8), (10), and (13)

using z = 19 cm.

Fig. 10. Peak output power of the backward stimulated Brillouin pulse, as a function of the normalized input power in the various cases studied.

TABLE CAPTIONS

Table I Characteristic parameters of EBBA (T_K = 78°) used as a self-focusing medium, with laser pulses having a full width at half maximum t_p = 15 nsec.

TABLE I

T (°C)	τ nsec	t_p/τ	n_2 (10^{-11} esu)	P_{cr} (kW)
79.7	72.5	0.21	237	0.071
82.7	32.1	0.47	111	0.151
96.0	7.25	2.07	33.4	0.503
112.0	2.87	5.2	18.2	0.926
130.8	1.33	11.3	11.8	1.420

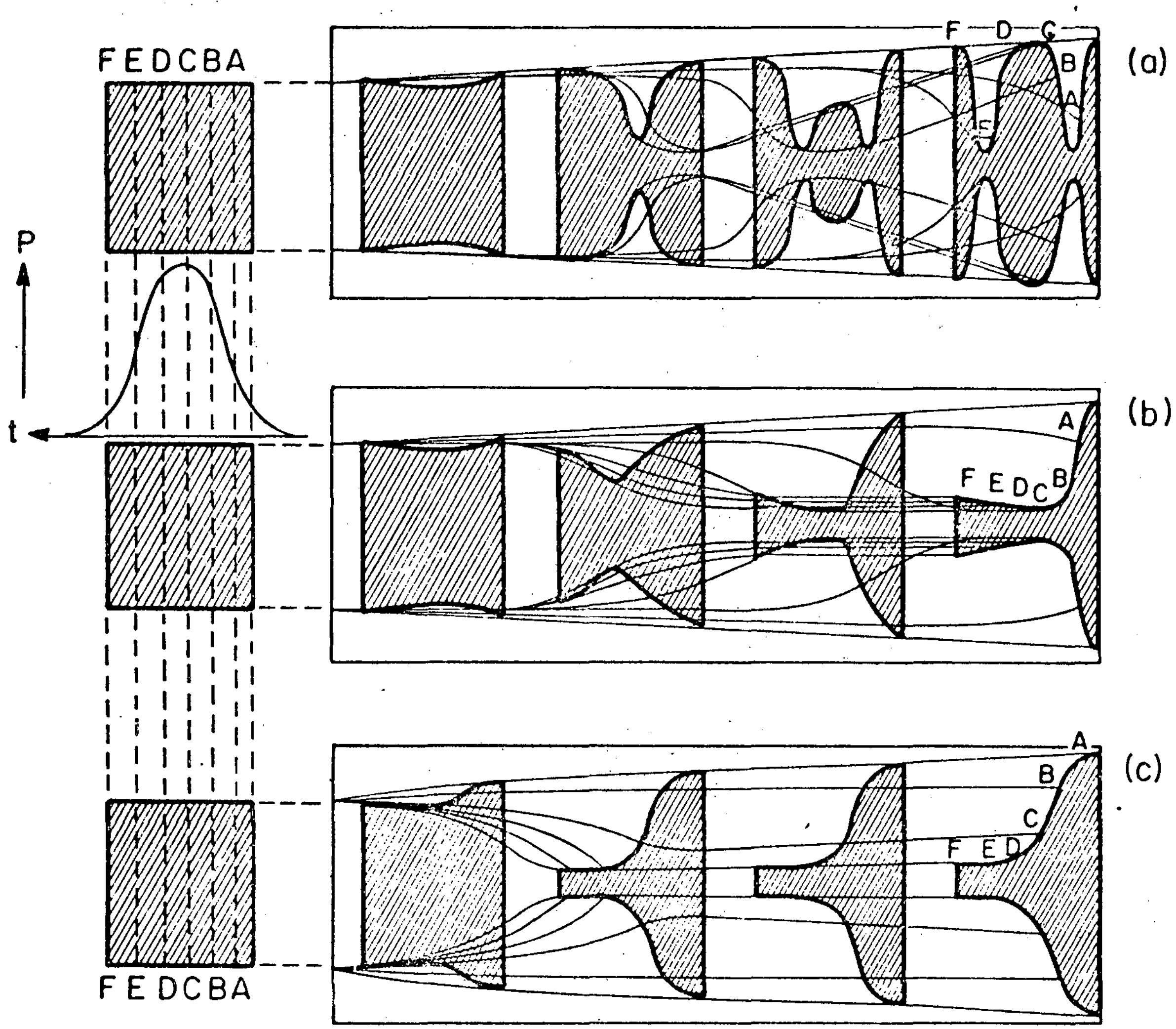

XBL 765-6830

Fig. 1

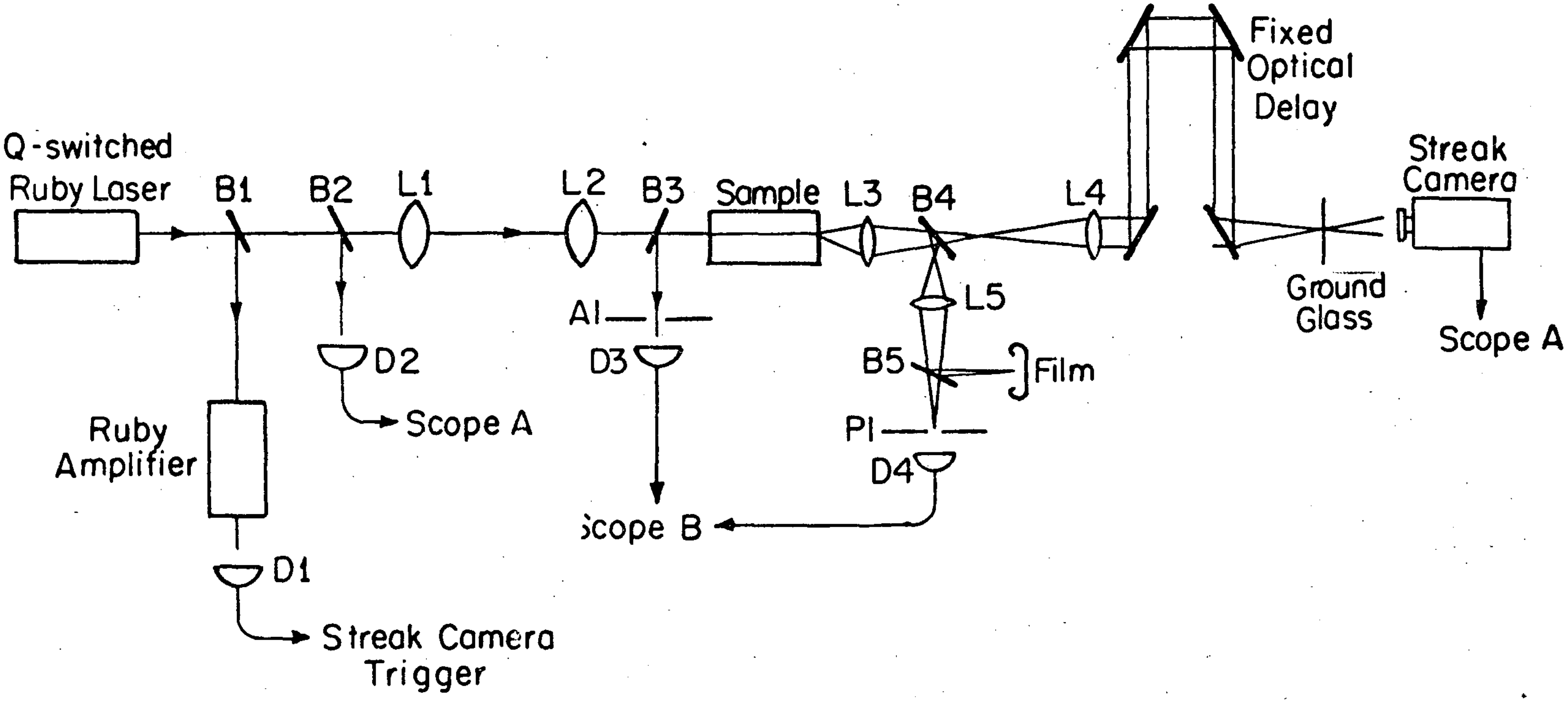

XBL 765-6831

Fig. 2

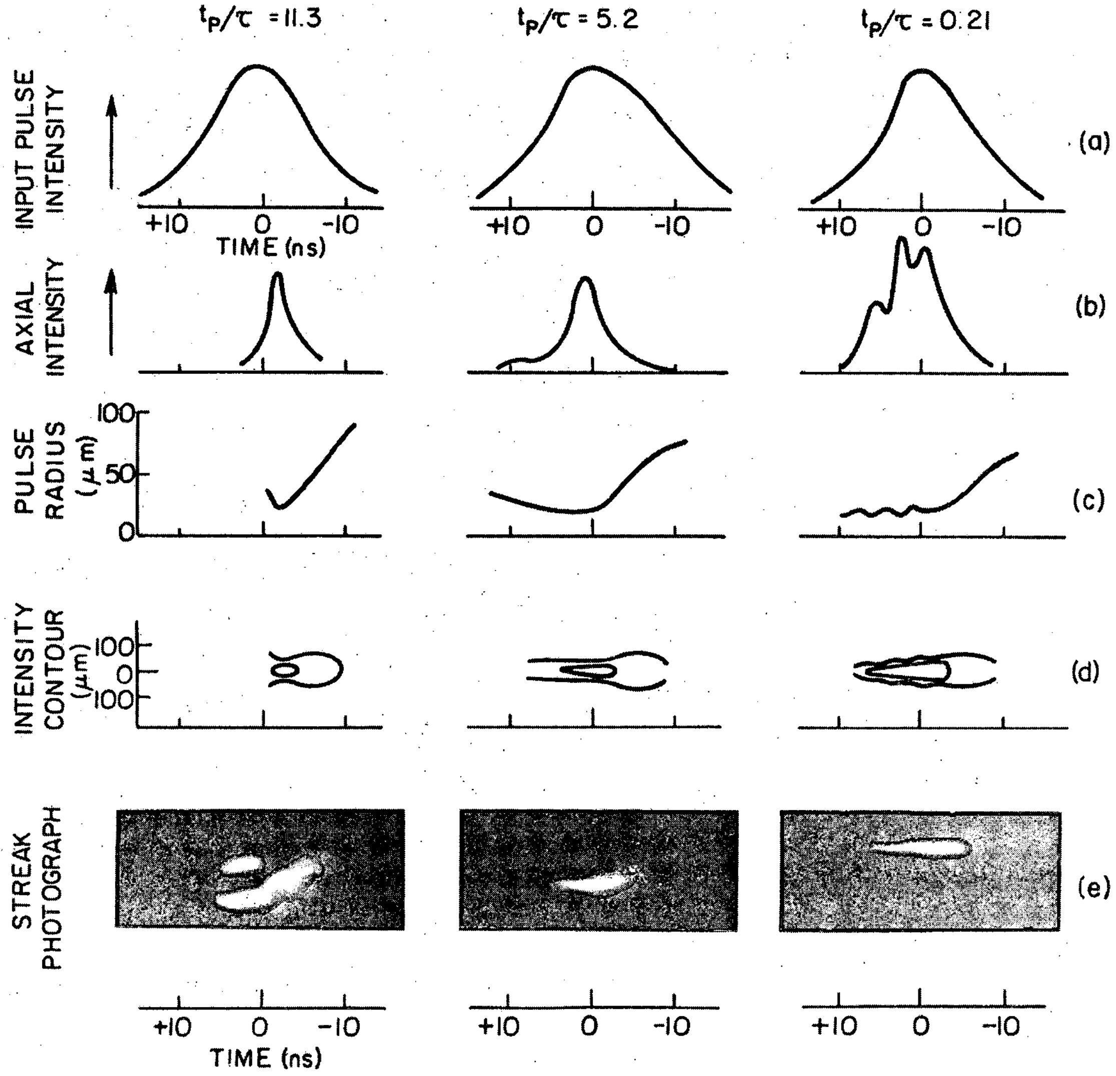

XBB 766-5236

Fig. 3

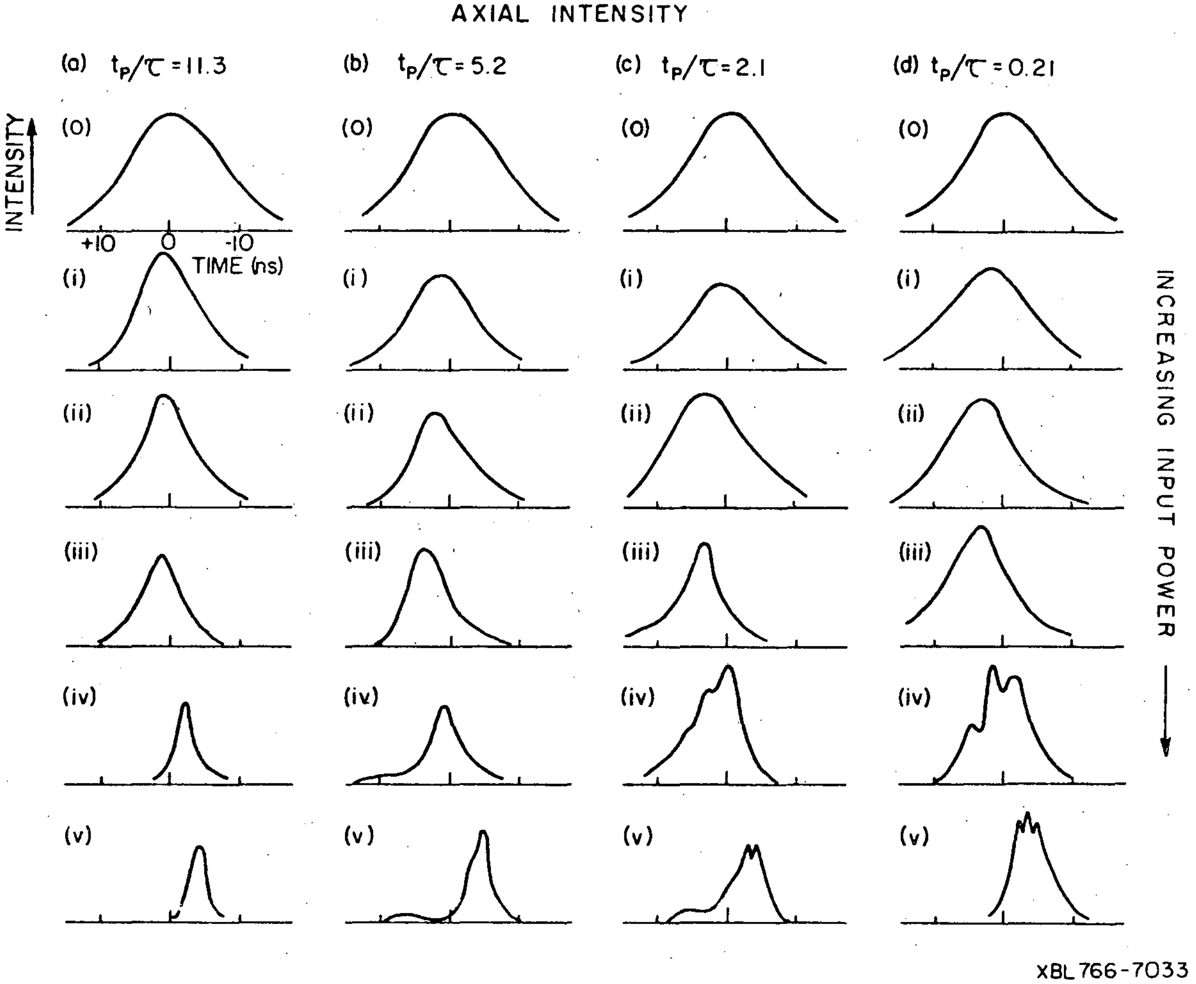
AXIAL INTENSITY
(a) $t_P/\tau = 11.3$
(b) $t_P/\tau = 5.2$
(c) $t_P/\tau = 2.1$
(d) $t_P/\tau = 0.21$
INTENSITY
(o)
(i)
(ii)
(iii)
(iv)
(v)
+10
0
-10
TIME (ns)
INCREASING INPUT POWER
XBL 766-7033

Fig. 4

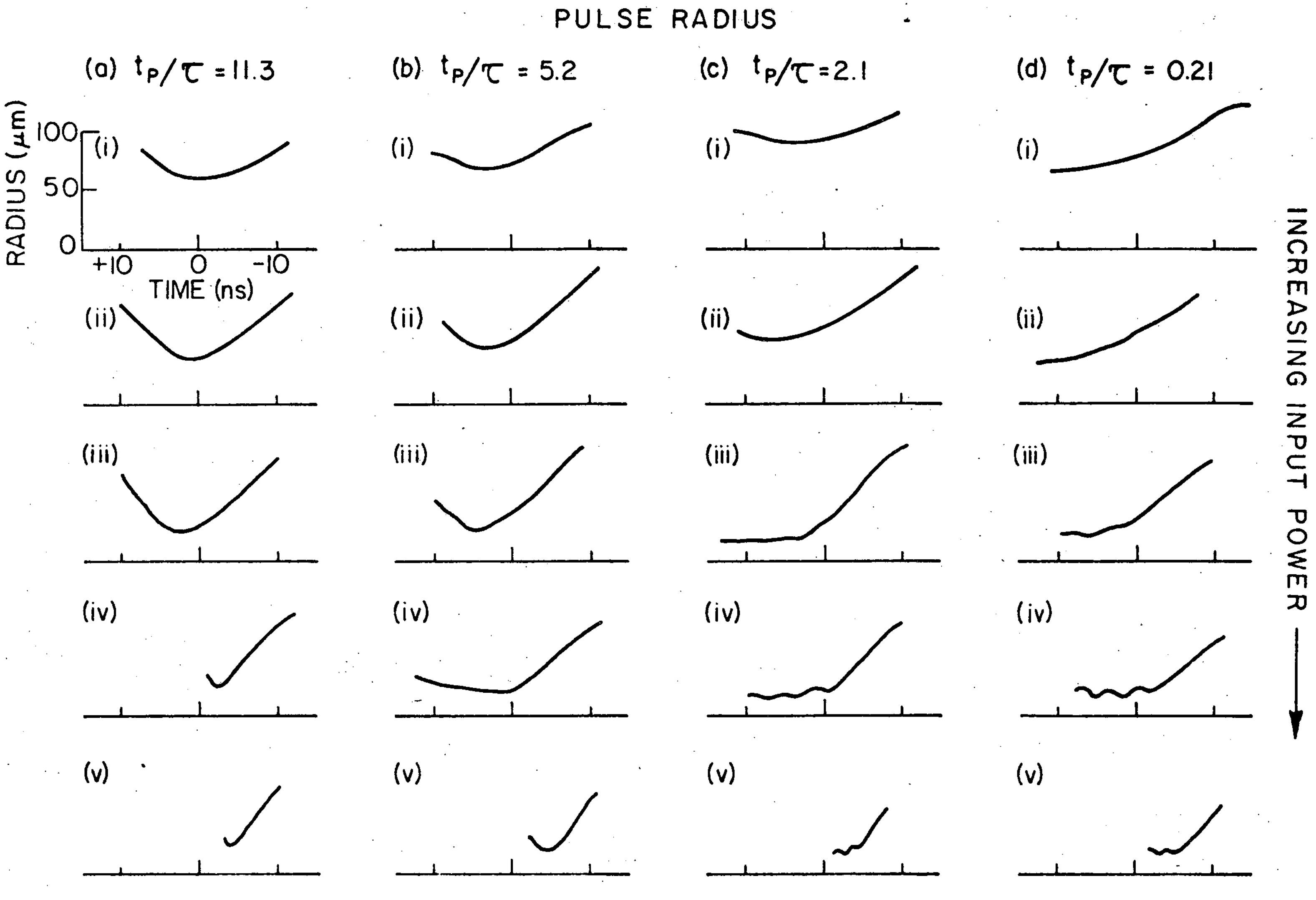

XBL 766-7034

Fig. 5

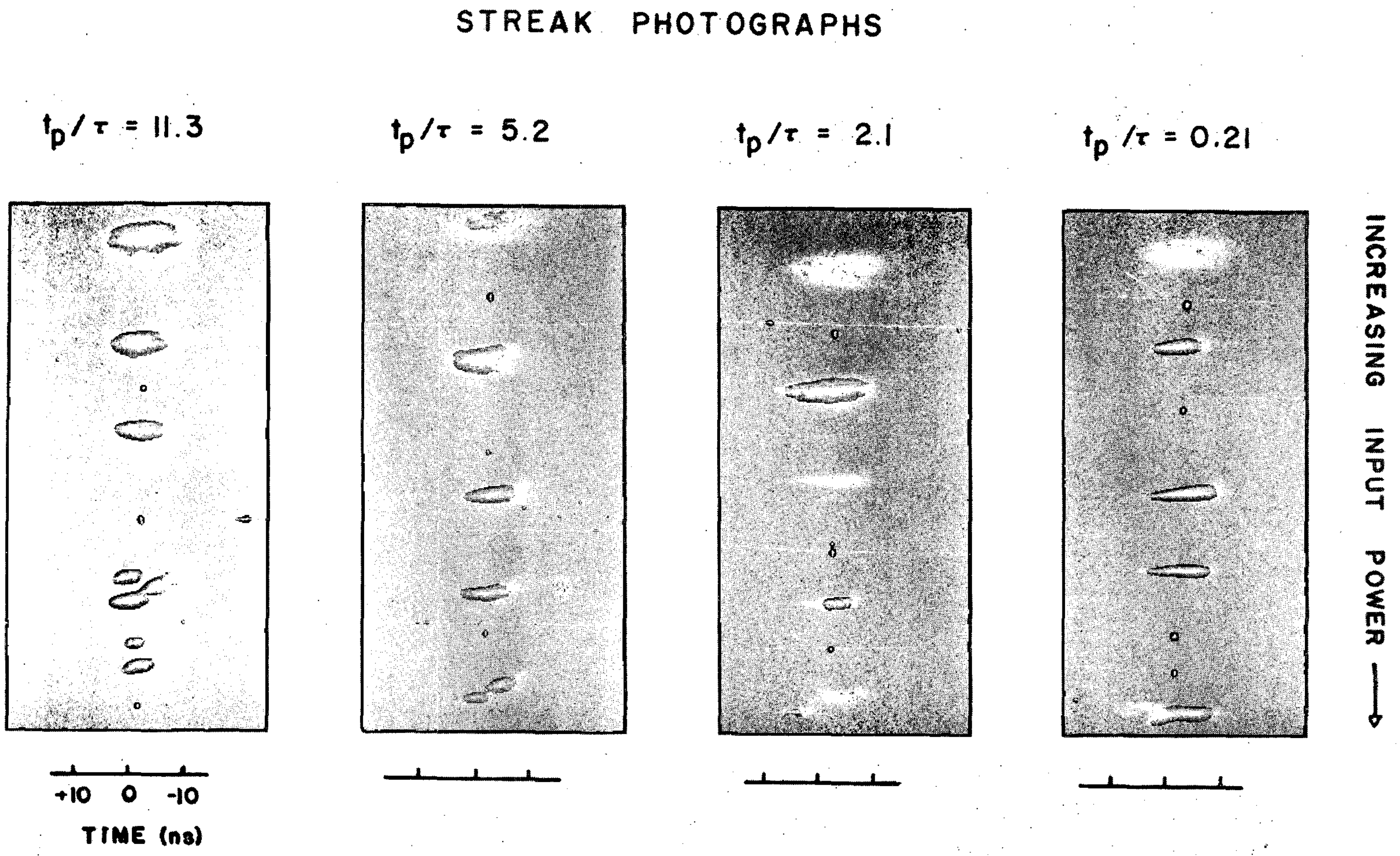

XBB 771-1

Fig. 6

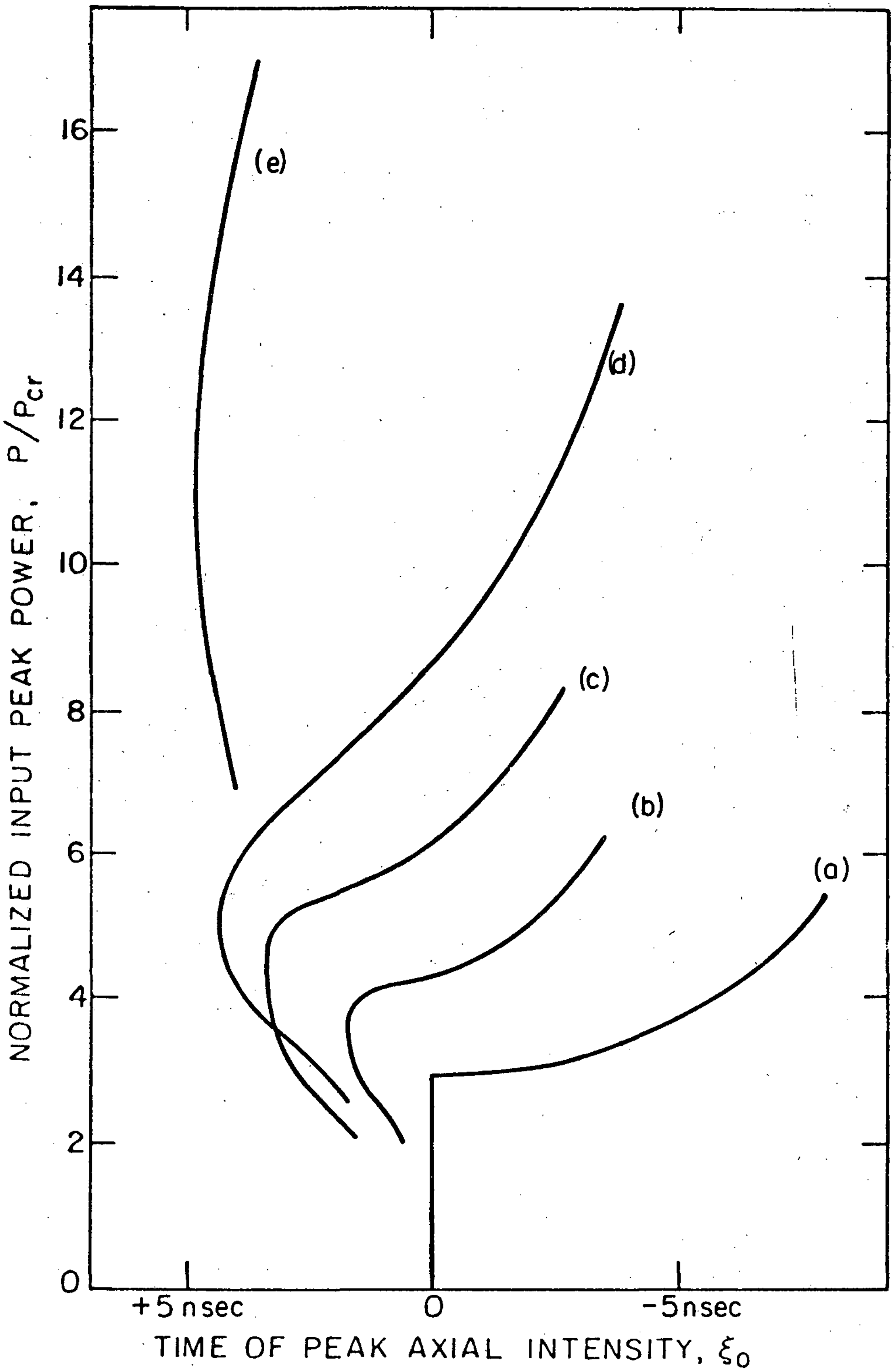

XBL765-6832

Fig. 7

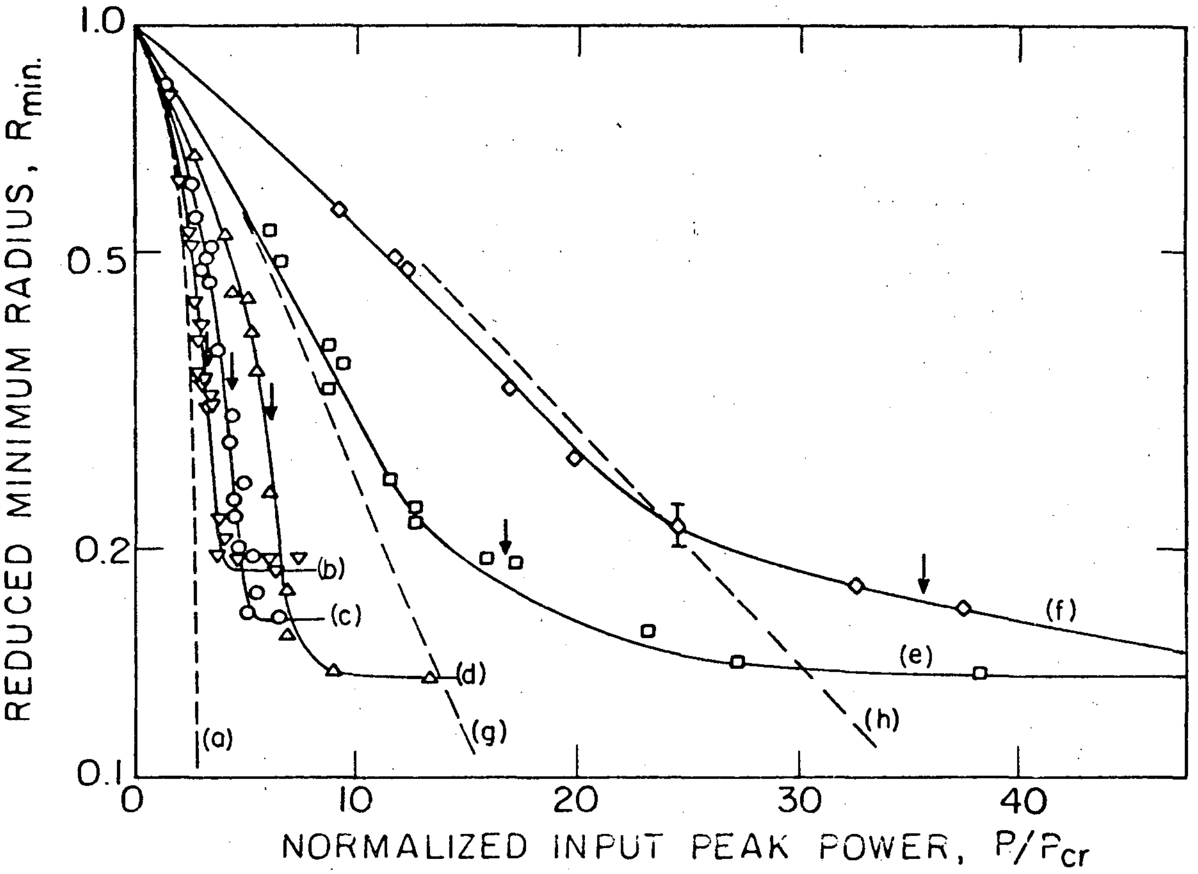

XBL 76 6-7031

Fig. 3

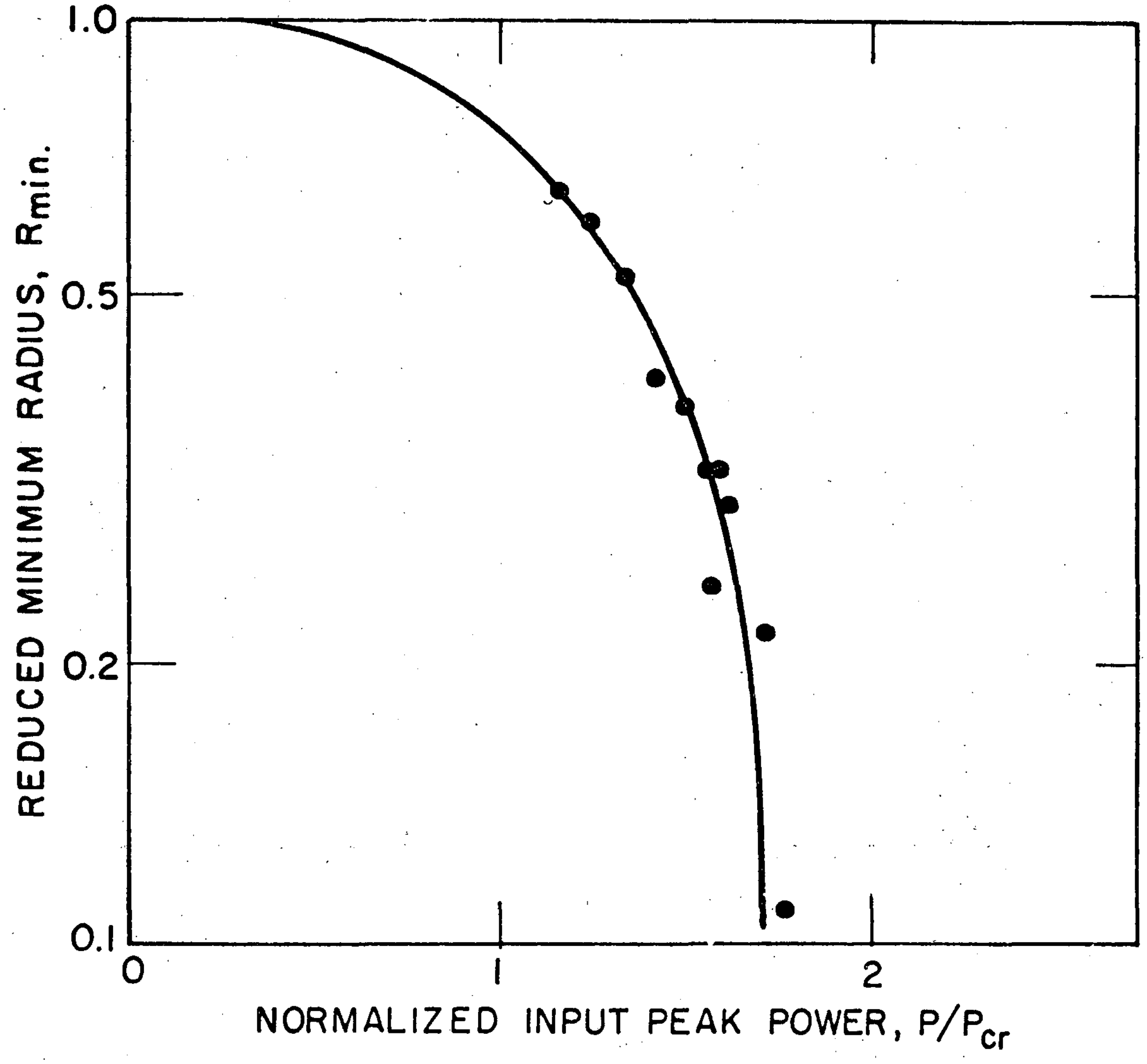

XBL 7612-11,468

Fig. 9

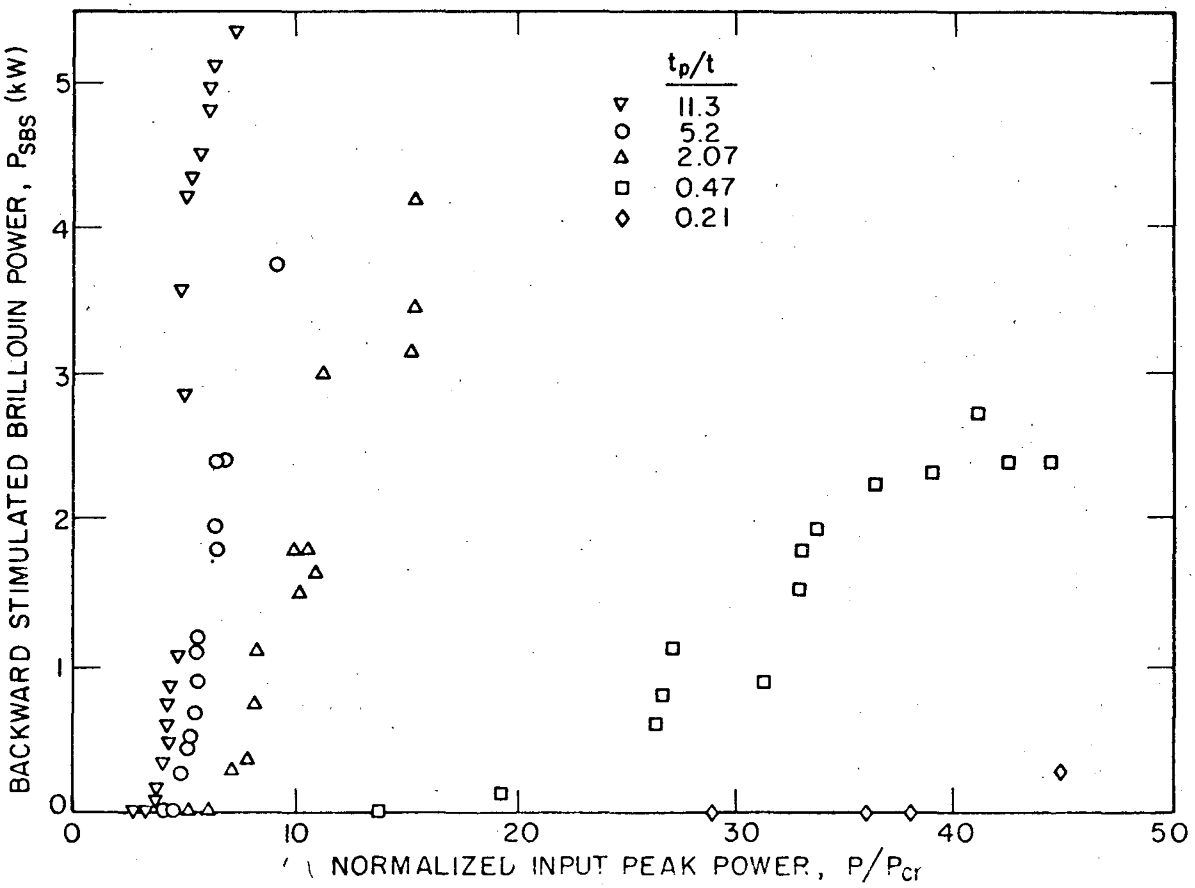

XBL 7612-11,469

Fig. 10

APPENDIX I: DISPERSION OF OPTICAL-FIELD-INDUCED REFRACTIVE INDICES

In the optical Kerr effect, the field-induced refractive indices generally have a very weak dependence on the frequencies of the probe laser and the strong laser. For example, in an isotropic liquid crystalline material we showed in Chapter II Eq. (6) that the optical Kerr constant was

$$B = 2(\omega/nc)\ \Delta\chi(\omega)\ \Delta\chi(\omega')/9a(T - T^*), \tag{1}$$

where ω is the strong laser and ω' is the probe laser. In Eq. (1), we see that B is proportional to $\Delta\chi(\omega)$ and $\Delta\chi(\omega')$ which are very weak functions of frequency in any transparent region of the spectrum.

However, the optical Kerr constant will become strongly frequency dependent if $\omega - \omega' \cong 0$ or if $\omega - \omega' \cong \pm\,\omega_o$ where ω_o is any material resonance frequency (e.g. a Raman frequency).[1-5] This is due to dispersion in the tensor elements of $\chi^{(3)}$. Recent experiments have used this dispersion of optical-field-induced refractive indices to obtain accurate measurements of material resonant frequencies, linewidths, and transition probabilities in liquids and vapors.[4,5,8] These measurements can give information similar to that obtained by the coherent anti-Stokes Raman effect[6-9] without any sensitivity to phase matching conditions.

Recent papers have discussed the theory of this dispersion near Raman resonances ($\omega - \omega' \cong \omega_o$)[4,5]. Here we will examine more closely the case $\omega - \omega' \cong 0$. We will derive this theory from a consideration of the Gibbs free energy density F, using a general expression for the electromagnetic energy density,[10] rather than the expression used in Chapter II. We will allow the optical field to be composed of a number of spectral components ω_n, ω_m, ... , with amplitudes $E_i(\omega_n)$, where the subscripts i or j refer to polarization states. Under these conditions, we obtain:

$$F = F_o + \frac{1}{2} a(T - T^*) \sum_{ij} Q_{ij}Q_{ji} - \sum_{ij} \sum_{nm} \chi_{ij}(\omega_m) \times \left[E_j(\omega_m)E_j^*(\omega_n)e^{i(\omega_m - \omega_n)t - i(\vec{k}_m - \vec{k}_n) \cdot \vec{r}} + \text{c.c.} \right], \tag{2}$$

where we have included the cross terms between different frequency components in the electromagnetic contribution to the free energy density. In Chapter II, we did not include these oscillatory terms, because they averaged to zero for the cases we were considering, and did not affect the Q_{ij}. In Eq. (2) we omit other terms which are higher order in Q_{ij}, as these do not affect the field induced refractive indices.

As before, the equation of motion for the tensorial order parameter is $\nu \partial Q_{ij}/\partial t = - \partial F/\partial Q_{ji}$, which gives:

$$\nu \frac{\partial Q_{ij}}{\partial t} + a(T - T^*)Q_{ij} = f_{ij}(t)$$

$$f_{ij}(t) = \frac{1}{12} \left[\sum_{nm} \Delta\chi(\omega_m)\left(E_j(\omega_m)E_i^*(\omega_n)e^{i(\omega_m - \omega_n)t - i(\vec{k}_m - \vec{k}_n) \cdot \vec{r}} + \text{c.c.}\right) - \frac{1}{3} \delta_{ij} \sum_{knm} \Delta\chi(\omega_m)\left(E_k(\omega_m)E_k^*(\omega_n)e^{i(\omega_m - \omega_n)t - i(\vec{k}_m - \vec{k}_n) \cdot \vec{r}} + \text{c.c.}\right)\right]. \tag{3}$$

We can solve Eq. (3) immediately, obtaining

$$Q_{ij}(t) = \frac{1}{\tau}\int_{-\infty}^{t} \frac{f_{ij}(t')}{a(T - T^*)} e^{-(t - t')/\tau} dt', \tag{4}$$

where the relaxation time is

$$\tau = \frac{\nu}{a(T - T^*)} . \qquad (5)$$

If the frequency amplitudes $E_i(\omega_n)$ are constant for times much longer than τ, then Eq. (4) gives

$$\begin{aligned} Q_{ij}(t) &= \frac{1}{12\tau a(T - T^*)} \Bigg[\sum_{nm} \Delta\chi(\omega_m) \Bigg(E_j(\omega_m) E_i^*(\omega_n) e^{- i(\vec{k}_m - \vec{k}_n) \cdot \vec{r}} \\ &\qquad \times \int_{-\infty}^{o} e^{i(\omega_m - \omega_n)t' - (t - t')/\tau} dt' + \text{c.c.} \Bigg) \\ &\qquad - \frac{1}{3} \delta_{ij} \sum_{knm} \Delta\chi(\omega_m) \Bigg(E_k(\omega_m) E_k^*(\omega_m) e^{-i(\vec{k}_m - \vec{k}_n) \cdot \vec{r}} \\ &\qquad \times \int_{-\infty}^{o} e^{i(\omega_m - \omega_n)t' - (t - t')/\tau} dt' + \text{c.c.} \Bigg) \Bigg] \\ &= \frac{1}{12a(T - T^*)} \Bigg[\sum_{nm} \Delta\chi(\omega_m) \Bigg(\frac{E_j(\omega_m) E_i^*(\omega_n) e^{i(\omega_m - \omega_n)t - i(\vec{k}_m - \vec{k}_n) \cdot \vec{r}}}{1 + i\tau(\omega_m - \omega_n)} \\ &\qquad + \text{c.c.} \Bigg) - \frac{1}{3} \delta_{ij} \sum_{knm} \Delta\chi(\omega_m) \\ &\qquad \times \Bigg(\frac{E_k(\omega_m) E_k^*(\omega_n) e^{i(\omega_m - \omega_m)t - i(\vec{k}_m - \vec{k}_n) \cdot \vec{r}}}{1 + i\tau(\omega_m - \omega_n)} + \text{c.c.} \Bigg) \Bigg] . \\ &= \sum_{nm} Q_{ij}(\omega_m, \omega_n) e^{i(\omega_m - \omega_n)t - i(\vec{k}_m - \vec{k}_n) \cdot \vec{r}} + \text{c.c.} , \qquad (6) \end{aligned}$$

where

$$Q_{ij}(\omega_m, \omega_n) \equiv \frac{\Delta\chi(\omega_m)}{12a(T - T^*)} \left[\frac{E_j(\omega_m) E_i^*(\omega_n) - \frac{1}{3} \delta_{ij} \sum_k E_k(\omega_m) E_k^*(\omega_n)}{1 + i\tau(\omega_m - \omega_n)} \right] . \qquad (7)$$

It is clear from the general expression in Eq. (6) that the order parameter Q_{ij} is only affected by those beat frequencies for which $(\omega_m - \omega_n)\tau \lesssim 1$.

The optical frequency polarization is determined by the applied fields and by the order parameter which results from those fields. For the case of a time-independent order parameter, de Gennes[11] has shown that

$$P_i(\omega') = \chi_{ii}(\omega')E_i(\omega') + \frac{2}{3}\sum_j \Delta\chi(\omega')Q_{ij}\,E_j(\omega'), \tag{8}$$

where $\Delta\chi(\omega')$ is the polarizability anisotropy of a fully ordered liquid crystal (e.g. $Q_{xx} = +1$, $Q_{yy} = Q_{zz} = -\frac{1}{2}$). The polarization in Eq. (8) contains both a linear part $P_i^{(1)}(\omega')$ and a nonlinear part $P_i^{(3)}(\omega')$, which are

$$P_i^{(1)}(\omega') = \chi_{ii}(\omega')E_i(\omega') \tag{9}$$

and

$$P_i^{(3)}(\omega') = \frac{2}{3}\sum_j \Delta\chi(\omega')Q_{ij}\,E_j(\omega'). \tag{10}$$

In our case, we know from Eq. (6) that Q_{ij} is time-dependent. Because of this, we must use a more generalized form of Eq. (10), which is

$$P_i^{(3)}(\omega' = \omega_\ell + \omega_m - \omega_n) = \sum_{j\ell mn}\left[\frac{2}{3}\left(Q_{ij}(\omega_m,\omega_n) + Q_{ij}^*(\omega_n,\omega_m)\right) \times E_j(\omega_\ell)\Delta\chi(\omega')e^{i\vec{r}\cdot(\vec{k}_\ell + \vec{k}_m - \vec{k}_n)}\right] + \text{c.c.}\,, \tag{11}$$

where the sum over ℓ, n, and m is restricted by the condition

$\omega' = \omega_\ell + \omega_m - \omega_n$.

We will be mainly interested in certain special cases where the nonlinear polarization given by Eq. (11) assumes a particularly simple form. For example, in certain cases we will find that $P^{(3)}$ can be written as

$$P_i^{(3)}(\omega') = \sum_j \delta\chi_{ij}(\omega')E_j(\omega'), \tag{12}$$

where the quantity $\delta\chi_{ij}(\omega')$ is independent of the amplitude of $E(\omega')$. If Eq. (12) is satisfied, then the field at ω' can be regarded as a probe of the $\delta\chi(\omega')$ induced by the other applied fields.

We will also find that under certain circumstances, the quantity $\delta\chi_{ij}(\omega')$ will be diagonalizable, giving

$$P_i^{(3)}(\omega') = \delta\chi_i(\omega')E_i(\omega'), \tag{13}$$

where $\delta\chi_i(\omega') \equiv \delta\chi_{ii}(\omega')$. When this happens we can interpret the $P^{(3)}(\omega')$ in terms of a field induced change in the linear optical constants. The linear refractive index $n_i(\omega')$ and the linear absorption coefficient $\kappa_i(\omega')$ have a simple relationship to the linear polarizability $\chi_i(\omega')$

$$\begin{aligned} n_i(\omega') &= Re\,\sqrt{1 + 4\pi\chi_i(\omega')} \\ \kappa_i(\omega') &= Im\,\sqrt{1 + 4\pi\chi_i(\omega')}\ , \end{aligned} \tag{14}$$

where we assume that $\chi_{ii}(\omega') = \delta_{ij}\chi_i(\omega')$ is diagonalized. The 1/e power absorption length is $\ell_i(\omega') = c/2\omega\kappa_i(\omega')$. If Eq. (13) is satisfied we can define

$$\begin{aligned} \delta n_i(\omega') &= (2\pi/n_i(\omega'))\mathit{Re}\ \delta\chi_i(\omega') \\ \delta\kappa_i(\omega') &= (2\pi/n_i(\omega'))\mathit{Im}\ \delta\chi_i(\omega') \end{aligned} \tag{15}$$

where we assume *Re* $\chi_i(\omega') >> $ *Im* $\chi_i(\omega')$, as in a transparent medium. Here positive $\delta\kappa$ corresponds to a field-induced loss, while negative $\delta\kappa$ corresponds to a field-induced gain.

Now we would like to examine the circumstances under which the nonlinear polarization as given by Eq. (11) satisfies Eqs. (12) and (13). We will restrict our attention to the nonlinear polarization at a frequency ω', where we require the amplitude of the field at frequency ω' to be much less than that of any fields of other frequencies. We will evaluate Eq. (11) assuming that only one other frequency ω is present, with $|E(\omega)|^2 >> |E(\omega')|^2$. Also, we will be interested in $|\omega - \omega'|/\omega \lesssim 10^{-3}$, so we have $\Delta\chi \equiv \Delta\chi(\omega) = \Delta\chi(\omega')$. In these limits, Eq. (11) gives

$$\begin{aligned} P_i^3(\omega') &= \sum_j \Bigg\{ \bigg[\frac{2}{3}\Big(Q_{ij}(\omega,\omega) + Q_{ij}^*(\omega,\omega)\Big) E_j(\omega') + \\ &\qquad \frac{2}{3}\Big(Q_{ij}(\omega',\omega) + Q_{ij}^*(\omega,\omega')\Big)\ E_j(\omega)\bigg] \Delta\chi e^{i\vec{k}'\cdot\vec{r}} + \text{c.c.}\Bigg\} \\ &= \frac{(\Delta\chi)^2 e^{i\vec{k}'\cdot\vec{r}}}{18a(T - T^*)} \Bigg[\sum_j \Bigg\{\bigg(-\frac{2}{3} + \frac{1}{1 - i\tau\Delta\omega}\bigg) E_i(\omega')E_j(\omega)E_j^*(\omega) + \\ &\qquad \bigg(1 + \frac{1}{1 - i\tau\Delta\omega}\bigg) E_j(\omega')E_j(\omega)E_i^*(\omega) + \\ &\qquad \bigg(1 - \frac{2}{3}\,\frac{1}{1 - i\tau\Delta\omega}\bigg) E_j(\omega')E_i(\omega)E_j^*(\omega)\Bigg\}\Bigg] + \text{c.c.}, \end{aligned} \tag{16}$$

where $\Delta\omega \equiv (\omega - \omega')$. Examination of Eq. (16) shows that it will automatically satisfy Eq. (12), because we have chosen $|E(\omega)|^2 >> |E(\omega')|^2$. We find that $\delta\chi$ becomes

$$\delta\chi_{xx}(\omega') = \frac{(\Delta\chi)^2}{18a(T - T^*)}\left[\left(\frac{4}{3} + \frac{4}{3}\,\frac{1}{1 - i\tau\Delta\omega}\right)|E_x(\omega)|^2 + \left(-\,\frac{2}{3} + \frac{1}{1 - i\tau\Delta\omega}\right)|E_y(\omega)|^2\right]$$

$$\delta\chi_{xy}(\omega') = \frac{(\Delta\chi)^2}{18a(T - T^*)}\left[\left(1 + \frac{1}{6}\,\frac{1}{1 - i\tau\Delta\omega}\right)\left(E_x^*(\omega)E_y(\omega) + E_x(\omega)E_y^*(\omega)\right) + \right.$$

$$\left.\left(\frac{5}{6}\,\frac{1}{1 - i\tau\Delta\omega}\right)\left(E_x^*(\omega)E_y(\omega) - E_x(\omega)E_y^*(\omega)\right)\right]$$

$$\tag{17}$$

$$\delta\chi_{yx}(\omega') = \frac{(\Delta\chi)^2}{18a(T - T^*)}\left[\left(1 + \frac{1}{6}\,\frac{1}{1 - i\tau\Delta\omega}\right)\left(E_x^*(\omega)E_y(\omega) + E_x(\omega)E_y^*(\omega)\right) + \right.$$

$$\left.\left(\frac{5}{6}\,\frac{1}{1 - i\tau\Delta\omega}\right)\left(E_y^*(\omega)E_x(\omega) - E_y(\omega)E_y^*(\omega)\right)\right]$$

$$\delta\chi_{yy}(\omega') = \frac{(\Delta\chi)^2}{18a(T - T^*)}\left[\left(\frac{4}{3} + \frac{4}{3}\,\frac{1}{1 - i\tau\Delta\omega}\right)|E_y(\omega)|^2 + \left(-\,\frac{2}{3} + \frac{1}{1 - i\tau\Delta\omega}\right)|E_x(\omega)|^2\right].$$

We will examine the diagonalizability of $\delta\chi$ in terms of the most general elliptical polarized basis states for the probe field. We will take

$$\hat{e}_1 = (\cos\Theta)\hat{x} + (\sin\Theta e^{i\alpha})\hat{y}$$

$$\hat{e}_2 = (-\sin\Theta e^{-i\alpha})\hat{x} + (\cos\Theta)\hat{y},$$

where we will choose Θ and α such that $\overleftrightarrow{\delta\chi}$ is diagonalized. Performing the diagonalization, we find immediately that the conditions on Θ and α are:

$$\tan\Theta\, e^{i\alpha} = \frac{-[\delta\chi_{xx} - \delta\chi_{yy}] \pm \sqrt{[\delta\chi_{xx} - \delta\chi_{yy}]^2 + 4\delta\chi_{xy}\delta\chi_{yx}}}{2\delta\chi_{xy}},$$

$$\tan\Theta\, e^{-i\alpha} = \frac{-[\delta\chi_{xx} - \delta\chi_{yy}] \pm \sqrt{[\delta\chi_{xx} - \delta\chi_{yy}]^2 + 4\delta\chi_{xy}\delta\chi_{yx}}}{2\delta\chi_{yx}}. \qquad (18)$$

Clearly these conditions can both be met only if

$$|\delta\chi_{yx}| = |\delta\chi_{xy}|. \qquad (19)$$

If Eq. (19) is satisfied, then we will find that

$$e^{i\alpha} = \pm\left[\frac{\delta\chi_{yx}}{\delta\chi_{yx}}\right]^{1/2} \qquad (20a)$$

$$\tan\Theta = -\left[\frac{\delta\chi_{xx} - \delta\chi_{xy}}{2\sqrt{\delta\chi_{xy}\delta\chi_{yx}}}\right] \pm \sqrt{1 + \left[\frac{\delta\chi_{xx} - \delta\chi_{yy}}{2\sqrt{\delta\chi_{xy}\delta\chi_{yx}}}\right]^2}\,. \qquad (20b)$$

But now Eq. (20b) can only be satisfied if

$$0 = Im\left[\frac{\delta\chi_{xx} - \delta\chi_{yy}}{2\sqrt{\delta\chi_{xy}\delta\chi_{yx}}}\right]$$

$$= Im\left[\frac{(\delta\chi_{xy} - \delta\chi_{yy})(\sqrt{\delta\chi_{xy}\delta\chi_{yx}})^*}{2|\delta\chi_{xy}\delta\chi_{yx}|}\right]. \qquad (21)$$

We see that Eqs. (19) and (21) must both be satisfied if $\overleftrightarrow{\delta\chi}$ is diagonalizable, and then Eqs. (20a) and (20b) can be used to actually diagonalize $\overleftrightarrow{\delta\chi}$. Using Eq. (17) for $\overleftrightarrow{\delta\chi}$, we find that Eq. (19) becomes

$$0 = \left(\frac{\tau\Delta\omega}{1 + [\tau\Delta\omega]^2}\right)\left(E_x^*(\omega)E_y(\omega) + E_y^*(\omega)E_x(\omega)\right)\left(E_x^*(\omega)E_y(\omega) - E_y^*(\omega)E_x(\omega)\right), \qquad (22)$$

and Eq. (21) becomes

$$0 = \left(\frac{\tau\Delta\omega}{1 + [\tau\Delta\omega]^2}\right)\left(|E_x(\omega)|^2 - |E_y(\omega)|^2\right)\left(E_x^*(\omega)E_y(\omega) - E_y^*(\omega)E_x(\omega)\right). \quad (23)$$

Equations (22) and (23) cannot in general both be satisfied, which means that $\overleftrightarrow{\delta\chi}$ cannot in general be diagonalized. However, there are four limiting cases in which both Eqs. (22) and (23) can be satisfied:

(a) First, if $(\omega' - \omega) = 0$, then Eqs. (22) and (23) are automatically satisfied, and $\overleftrightarrow{\delta\chi}$ can be diagonalized according to Eq. (20).

(b) Second, if $|\tau(\omega' - \omega)| >> 1$, we will also have Eqs. (22) and (23) automatically satisfied, and $\overleftrightarrow{\delta\chi}$ will be diagonalizable.

(c) Third, if $|\tau\Delta\omega| \sim 1$, $\left(|E_x(\omega)|^2 - |E_y(\omega)|^2\right) = 0$, and $\left(E_x^*(\omega)E_y(\omega) + E_y^*(\omega)E_x(\omega)\right) = 0$, then the strong beam E( ) will be circularly polarized. We see that $\overleftrightarrow{\delta\chi}$ can be diagonalized for such a strong beam for all values of frequency detuning $(\omega' - \omega)$.

(d) Fourth, if $|\tau(\omega' - \omega) \sim 1$, and $\left(E_x^*(\omega)E_y(\omega) - E_y^*(\omega)E_x(\omega)\right) = 0$, then the strong beam $E(\omega)$ will be linearly polarized. We see from Eqs. (22) and (23) that $\overleftrightarrow{\delta\chi}$ will be diagonalizable over the whole range of frequency $(\omega' - \omega)$.

We see that Eqs. (22) and (23) cannot be satisfied for an elliptically polarized strong beam if $|\tau(\omega' - \omega)| \sim 1$. This means that $\overleftrightarrow{\delta\chi}$ is not diagonalizable for such a strong beam.

We have seen that if the strong beam is circularly or linearly polarized, $\overleftrightarrow{\delta\chi}$ will be diagonalizable. So for these special cases, the effects of the nonlinear polarization can be expressed in terms of $\delta n_i(\omega')$ and $\delta k_i(\omega')$ using Eq. (15). Now we can evaluate these quantities. We will assume a specific optical field geometry with $\vec{k} \parallel + \hat{z}$ and $\vec{k}' \parallel - \hat{z}$.

We are purposely taking the propagation of two beams to be in different directions, so that they will remain distinguishable as $\omega' \to \omega$. We have chosen a specific angle of 180° between $\vec{k}$ and $\vec{k'}$ to avoid cumbersome expressions. It is clear from Eq. (16) that $P^3(\omega')$ has only a weak dependence on this angle, so little loss of generality results from this assumption.

For the specific case of a linearly polarized strong field ω, $\vec{E}(\omega) = \hat{x}\, E_x(\omega)$, we obtain

$$P_x^{(3)}(\omega') = \frac{(\Delta\chi)^2 e^{i\omega' t + ik'z}}{18a(T - T^*)}\, E_x(\omega')\,|E(\omega)|^2 \left[\frac{4}{3} + \frac{4}{3}\left(\frac{1}{1 - i\tau\Delta\omega}\right)\right]$$

$$P_y^{(3)}(\omega') = \frac{(\Delta\chi)^2 e^{i\omega' t + ik'z}}{18a(T - T^*)}\, E_y(\omega')\,|E(\omega)|^2 \left[-\frac{2}{3} + \left(\frac{1}{1 - i\tau\Delta\omega}\right)\right] . \qquad (24)$$

Then Eq. (15) gives

$$\delta n_x = (2\pi/n)\, \frac{(\Delta\chi)^2}{18a(T - T^*)}\, |E(\omega)|^2 \left(\frac{4}{3} + \frac{4}{3}\, \frac{1}{1 + (\tau\Delta\omega)^2}\right)$$

$$\delta n_y = (2\pi/n)\, \frac{(\Delta\chi)^2}{18a(T - T^*)}\, |E(\omega)|^2 \left(-\frac{2}{3} + \frac{4}{3}\, \frac{1}{1 + (\tau\Delta\omega)^2}\right)$$

$$\delta\kappa_x = (2\pi/n)\, \frac{(\Delta\chi)^2}{18a(T - T^*)}\, |E(\omega)|^2 \left(\frac{4}{3}\, \frac{\tau\Delta\omega}{1 + (\tau\Delta\omega)^2}\right) \qquad (25)$$

$$\delta\kappa_y = (2\pi/n)\, \frac{(\Delta\chi)^2}{18a(T - T^*)}\, |E(\omega)|^2 \left(\frac{\tau\Delta\omega}{1 + (\tau\Delta\omega)^2}\right) .$$

We see that each of these quantities has a substantial variation with frequency at $\Delta\omega = \omega - \omega' \cong 0$.

For a circularly polarized strong beam, $\vec{E}(\omega) = E(\omega)\hat{e}_+$, where $\hat{e}_\pm = (\hat{x} \pm i\hat{y})/\sqrt{2}$, we obtain

$$P_+^{(3)}(\omega') = \frac{(\Delta\chi)^2 e^{i\omega' t + ik'z}}{18a(T - T^*)}\left[E_+(\omega')\left(\frac{1}{3} + \frac{1}{3}\,\frac{1}{1 - i\tau\Delta\omega}\right)|E(\omega)|^2\right]$$

$$P_-^{(3)}(\omega') = \frac{(\Delta\chi)^2 e^{i\omega' t + ik'z}}{18a(T - T^*)}\left[E_-(\omega')\left(\frac{1}{3} + 2\,\frac{1}{1 - i\tau\Delta\omega}\right)|E(\omega)|^2\right] . \tag{26}$$

Then Eq. (15) gives

$$\delta n_+(\omega') = \frac{2\pi}{n}\,\frac{(\Delta\chi)^2}{18a(T - T^*)}\,|E(\omega)|^2\left[\frac{1}{3} + \frac{1}{3}\left(\frac{1}{1 + (\tau\Delta\omega)^2}\right)\right]$$

$$\delta n_-(\omega') = \frac{2\pi}{n}\,\frac{(\Delta\chi)^2}{18a(T - T^*)}\,|E(\omega)|^2\left[\frac{1}{3} + 2\left(\frac{1}{1 + (\tau\Delta\omega)^2}\right)\right]$$

$$\delta\kappa_+(\omega') = \frac{2\pi}{n}\,\frac{(\Delta\chi)^2}{18a(T - T^*)}\,|E(\omega)|^2\left[\frac{1}{3}\,\frac{\tau\Delta\omega}{1 + (\tau\Delta\omega)^2}\right]$$

$$\delta\kappa_-(\omega') = \frac{2\pi}{n}\,\frac{(\Delta\chi)^2}{18a(T - T^*)}\,|E(\omega)|^2\left[2\,\frac{\tau\Delta\omega}{1 + (\tau\Delta\omega)^2}\right] . \tag{27}$$

The linear and circular birefringences of Eqs. (25) and (27) can, in fact, both be observed with a linearly polarized probing beam. The circularly polarized strong beam will rotate the plane of polarization of the probe beam. On the other hand, the linear birefringence from a linearly polarized strong beam will make the probe beam become elliptically polarized. We will now calculate the signal which would be observed in an experiment for these two cases. The sample will be placed between crossed polarizers in the probing beam. In addition to calculating the signal for the two limiting cases of linear and circularly polarized strong beams, we will also calculate it for strong beams of general ellipticity. We will define a phase shift Φ, such that $\Phi = 0$ corresponds to linearly polarized light, while $\Phi = \pi/2$ corresponds to $\hat{e}_+$ circularly polarized light. Intermediate values of Φ will correspond to intermediate ellipticities.

We will have the probe beam polarization along one of the axes of the strong beam ellipse, so that the probe beam will be along one of the principle axes of $\delta\chi_{ij}$. For a probe beam $\vec{E}(\omega') = \hat{x}\, E(\omega')e^{i\omega' t + ik' z}$, the strong beam will be $\vec{E}(\omega) = [\hat{x}/\sqrt{2} + \hat{y}\ e^{i\Phi}/\sqrt{2}]E(\omega)e^{i\omega t - ikz}$, and Eq. (16) gives

$$P_x^{(3)}(\omega') = \frac{(\Delta\chi)^2 e^{i\omega' t + ik' z}}{18a(T - T^*)}|E(\omega)|^2 E(\omega') \left[\frac{1}{3} + \frac{7}{6}\left(\frac{1}{1 - i\tau\Delta\omega}\right)\right]$$

$$P_y^{(3)}(\omega') = \frac{(\Delta\chi)^2 e^{i\omega' t + ik' z}}{18a(T - T^*)}|E(\omega)|^2 E(\omega') \left[\cos \Phi\left(1 + \frac{1}{6}\left(\frac{1}{1 - i\tau\Delta\omega}\right)\right)\right.$$

$$\left. + \ i \sin \Phi\left(\frac{5}{6}\,\frac{1}{1 - i\tau\Delta\omega}\right)\right] , \tag{28}$$

This equation gives $P^{(3)}(\omega')$ at a specific point in the medium, in terms of the fields at that point. We can use the EM wave equation to determine the $\vec{E}$ field radiated by this $P^{(3)}(\omega')$. We start from the general wave equation

$$\vec{\nabla} \times \vec{\nabla} \times \vec{E}(\omega', z)\frac{\varepsilon}{c^2}\frac{\partial^2}{\partial t^2}\vec{E}_{(\omega', z)} = \frac{4\pi}{c^2}\frac{\partial^2}{\partial t^2} P^{NL}_{(\omega', z)} \tag{29}$$

where ε is the linear optical frequency dielectric constant and where we now allow the fields to vary in amplitude along the z axis. Assuming that $E(\omega')$ satisfies that slowly varying envelope approximation[13] $|\partial^2 E/\partial z^2| \ll k|\partial E/\partial z|$, and using $\vec{\nabla} \cdot \vec{E} = 0$, we obtain

$$2ik' \frac{\partial}{\partial z} E(\omega', z) = (\omega')^2 \frac{4\pi}{c^2} P_{NL}^{(3)}(\omega', z) \ . \tag{30}$$

This equation can easily be integrated to find $\vec{E}(\omega', z)$ for a given

$P_{NL}^{(3)}(\omega',z)$. As an example, we will consider the solution for a particularly simple geometry, with a sample of length ℓ, and $|E(\omega,z)|^2 = |E(\omega)|^2$ independent of z. The signal is the part of the probe beam transmitted by the crossed polarizer, so the signal intensity is proportional to

$$|E_y(\omega',z = \ell)|^2 = \left(\frac{2\pi\omega'}{nc}\right)^2 \ell^2 |\chi^{(3)}_{\text{effective}}|^2 |E_x(\omega')|^2 |E(\omega)|^4 \quad (31)$$

where we assume $|E_y(\omega',z = \ell)| << |E_x(\omega')|$ and where

$$\chi^{(3)}_{\text{effective}} = \frac{(\Delta\chi)^2}{18a(T - T^*)}\left[\cos\Phi\left(1 + \frac{1}{6}\,\frac{1}{1 - i\tau\Delta\omega}\right) + i\sin\Phi\left(\frac{5}{6}\,\frac{1}{1 - i\tau\Delta\omega}\right)\right] . \quad (32)$$

We then have

$$|\chi^{(3)}_{\text{effective}}|^2 = \left(\frac{(\Delta\chi)^2}{18a(T - T^*)}\right)^2 \left[\cos^2\Phi\left(1 + \frac{13}{36}\,\frac{1}{1 + (\tau\Delta\omega)^2}\right) + \sin^2\Phi\left(\frac{25}{36}\,\frac{1}{1 + (\tau\Delta\omega)^2}\right) + \cos\Phi\sin\Phi\left(-\frac{10}{6}\,\frac{\tau\Delta\omega}{1 + (\tau\Delta\omega)^2}\right)\right] , \quad (33)$$

which we have plotted in Fig. 1 for three different strong beam polarizations.

As discussed in Chapter II, the nonlinear polarization can be described more generally from symmetry considerations.[14] For $\omega \neq \omega'$ and $\vec{E}(\omega) = \hat{x}\,E(\omega)$,

$$P_x^{(3)}(\omega') = 6\left[\chi_{1122}^{(3)}(\omega' = \omega' + \omega - \omega) + \chi_{1212}^{(3)}(\omega' = \omega' + \omega - \omega) + \chi_{1221}^{(3)}(\omega' = \omega' + \omega - \omega)\right]|E(\omega)|^2 E_x(\omega')$$

$$P_y^{(3)}(\omega') = 6\left[\chi_{1122}^{(3)}(\omega' = \omega' + \omega - \omega)\right]|E(\omega)|^2 E_y(\omega'). \qquad (34)$$

For a circularly polarized strong field $\vec{E}(\omega) = \hat{e}_+ E(\omega)$,

$$P_+^{(3)}(\omega') = 6\left[\chi_{1122}^{(3)}(\omega' = \omega' + \omega - \omega) + \chi_{1212}^{(3)}(\omega' = \omega' + \omega - \omega)\right]|E(\omega)|^2 E_+(\omega')$$

$$(35)$$

$$P_-^{(3)}(\omega') = 6\left[\chi_{1122}^{(3)}(\omega' = \omega' + \omega - \omega) + \chi_{1221}^{(3)}(\omega' = \omega' + \omega - \omega)\right]|E(\omega)|^2 E_-(\omega').$$

By comparing Eqs. (18), (20), (28), and (29), we find

$$\chi_{1212}^{(3)}(\omega' = \omega' + \omega - \omega) = \frac{1}{6}\,\frac{(\Delta\chi)^2}{18a(T - T^*)}\left[1 - \frac{2}{3}\,\frac{1}{1 - i\tau\Delta\omega}\right]$$

$$\chi_{1221}^{(3)}(\omega' = \omega' + \omega - \omega) = \frac{1}{6}\,\frac{(\Delta\chi)^2}{18a(T - T^*)}\left[1 + \frac{1}{1 - i\tau\Delta\omega}\right] \qquad (36)$$

$$\chi_{1122}^{(3)}(\omega' = \omega' + \omega - \omega) = \frac{1}{6}\,\frac{(\Delta\chi)^2}{18a(T - T^*)}\left[-\frac{2}{3} + \frac{1}{1 - i\tau\Delta\omega}\right].$$

So we have determined the frequency dependence of all three of the independent elements of the tensor $\chi_{ijk\ell}^{(3)}(\omega' = \omega' + \omega - \omega)$.

References

1. N. Bloembergen and P. Lallemand, Phys. Rev. Lett. 16, 81 (1966).
2. M. Paillette, Ann. Phys. 4, 671 (1969).
3. A. Owyoung, Ph. D. Thesis, Physics Dept., Cal. Tech. (1971)
4. D. Heiman, R. W. Hellwarth, M. D. Levenson, and G. Martin, Phys. Rev. Lett. 36, 189 (1976).
5. P. F. Liao and G. C. Bjorklund, Phys. Rev. Lett. 36, 584 (1974).
6. M. D. Levenson, IEEE J. Quantum Electron. QE-10, 110 (1974).
7. M. D. Levenson and N. Bloembergen, Phys. Rev. B10, 4447 (1974).
8. H. Lotem and R. T. Lynch, Jr., Phys. Rev. Lett. 37, 334 (1976).
9. R. F. Begley, A. B. Harvey, and R. Byer, Appl. Phys. Lett. 25, 387 (1974).
10. See, for example, L. M. Landau and E. M. Lifschitz, Electrodynamics of Continuous Media, Addison Wesley (1960), Chapter 11.
11. P. G. De Gennes, Phys. Lett. 30A, 454 (1969) and Mol. Cryst. Liq. Cryst. 2, 193 (1971).
12. See, for example, L. M. Landau and E. M. Lifschitz, op. cit., Chapter 9.
13. See, for example, N. Bloembergen, Nonlinear Optics, Benjamin, N. Y. (1963), Chapter 4.
14. P. D. Maker and R. W. Terhune, Phys. Rev. 137, A801 (1965).

FIGURE CAPTIONS

Fig. 1. $|\chi^{(3)}_{\text{effective}}|^2$ for transmission of probe beam through crossed polarizers as a function of frequency detuning for different strong beam polarizations: (a) linearly polarized ($\Phi = 0$), (b) elliptically polarized with ellipticity $\varepsilon = \sqrt{2(\sqrt{2} - 1)}$ ($\Phi = \pi/4$), (c) circularly polarized ($\Phi = \pi/2$).

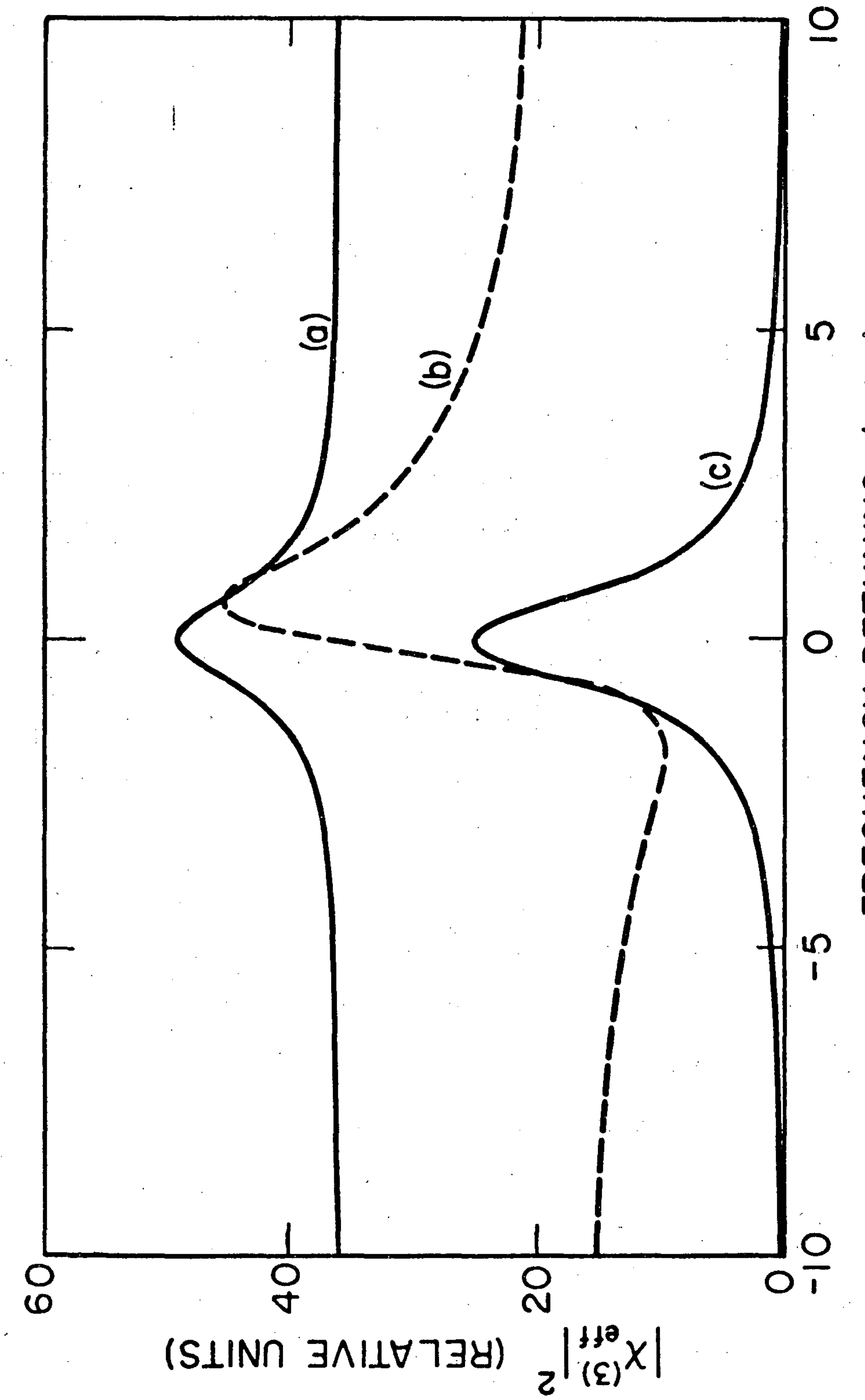

XBL 7611-7709

Fig. 1

APPENDIX II: OPERATION OF THE MODE-LOCKED RUBY LASER

Mode-locked lasers are very useful sources of short, intense laser pulses.[1-5] They can produce pulses with a duration as short as 1 psec. Several review articles discuss the general principles of mode-locking as well as the specific laser systems.[1-5] Here, I will concentrate on the specific system used in my experiments.

In a laser cavity, oscillation can occur upon discrete longitudinal modes, all separated in frequency by $\delta\nu = c/2L$, where L is the length of the laser cavity. The number of modes N which actually oscillate is $N \lesssim \Delta\nu/\delta\nu$, where $\Delta\nu$ is the gain band width of the laser medium. Simple analysis[1-5] shows that the duration of the pulses δt is limited to $\delta t > 1/\Delta\nu$. Frequently, researchers try to obtain pulses which are as short as possible. In order to do this, they must use a medium with a large $\Delta\nu$. For example, in the orange region of the visible spectrum, pulses shorter than 0.5 psec have been reported with organic dye lasers.[5,6]

If the mode-locked laser is properly adjusted, it will produce a train of short pulses, separated in time by 2L/c, one cavity round-trip time. To obtain only one train of pulses, the laser must be operated close to its lasing threshold. Also, there must be no stray reflections which might alter the phases of the laser modes in the cavity. So all optical elements which the laser beam encounters must be tilted to prevent the reflections from traveling back along the laser axis. This applies to components outside of the laser cavity as well as to those inside the cavity. In addition, losses must be avoided in the laser cavity. To obtain the shortest pulses, all optical elements must be tilted at Brewster's angle.

In our experiment, we did not want pulses shorter than about 1 nsec. This was because our time resolution in detecting the optical Kerr signal was limited to several nanoseconds (see Chapter II). If we used pulses much shorter than 1 nsec, we encountered damage problems because of the high peak power of the laser. To obtain 1 nsec long pulses, we used one optical element in the laser cavity at an angle <u>not</u> equal to Brewster's angle. This produced a loss of about 4% from each surface. Since the longitudinal modes of the laser cavity are standing waves, they each have nodes and maxima at different places in the cavity from other modes. A 4% loss at one point in the cavity will thereby affect some modes more than others. Suppose the loss is at a distance L' from one of the mirrors. It will produce a maximum loss for modes with $\nu_n = n\delta\nu = (m + \frac{1}{2})(c/2L')$ where ν_n is the mode frequency and n and m are integers. Modes with such maximum loss will be spaced in frequency by $\delta\nu_{mod} = c/2L(L/L')/(1 - (L/L'))$. This will tend to limit the mode-locked pulses to a length $\delta t > 1/\delta\nu_{mod}$, <u>if</u> the loss at distance L' is large enough to appreciably affect the amplitudes of the various modes.

In our laser, the dye cell was the optical element which was not at Brewster's angle. It was tilted at an angle of about 1.7° to the laser beam. An aperature A-1 (see Fig. 1) of 2mm diameter prevented the reflections from the dye cell from entering the ruby rod. The cavity length L was about 85 cm, and distance between the dye cell and the front mirror M-2 was about 75 cm, giving $\delta\nu_{mod} \cong 10\ c/2L$. This would tend to limit the laser pulse length to $\delta t > 0.57$ nsec since the cavity round-trip time was $2L/c = 5.7$ nsec. In practice, we observed pulses with a duration of about 1 nsec.

Aside from the tilt of the dye cell, the laser cavity was the same as would be used for the generation of ultrashort pulses. The ruby rod was Brewster-cut, and the mirrors were both flat, with reflectivities of 99% (M-1) and 50% (M-2). To use the laser, the cavity was first aligned using reflections of the He-Ne beam from M-1 and M-2. This was done with only methanol in the dye cell, to check the free-running lasing threshold. This threshold was a sensitive indication of how well the cavity was aligned. Then the cryptocyanine was added to the methanol and the output laser pulse shape was observed using detector D (ITT - FW 114A photodiode) and the scope (Tektronix 519). If the dye concentration were too low, the laser intensity would not drop to zero between the pulses in the train, or more than one train of pulses would be present. On the other hand, if the dye were too concentrated, the pulse train became shorter and consisted of about 4 pulses rather than 10 or more. Once the laser was aligned and the dye concentration was optimized, it would give good trains of 1 nsec pulses for several days without adjustment. It did need to be always operated close to its lasing threshold. Also, it was sensitive to changes in the room temperature, which could easity degrade the alignment of the mirrors M-1 and M-2.

In our experiment, we wanted to use a single 1 nsec pulse rather than a series of such pulses. So we used a Pockels cell to switch out a single pulse. Outside the laser cavity, the light passed through a crossed polarizer (P-1) and analyzer (P-2). Between them was a Pockels cell (Lasermetrics EOM 704). These optical components were all slightly tilted, so back-reflected laser light was blocked by A-2. This was essential to avoid feedback into the laser cavity which would give multiple trains of pulses. Initially, there was no voltage on the Pockels cell, so that the laser light polarization remained constant passing through the cell. Then it was rejected by the second Glan-Thompson (P-2), and was focused by the lens into the spark gap.

The spark gap was used to generate a laser-triggered high voltage pulse to drive the Pockels cell. Such a laser-triggered spark gap is currently the best source of fast-rising high voltage pulses.[7-10] General properties of these devices have been covered in a review article by Guenther and Bettis.[7] One electrode of the spark gap is connected to a high voltage power supply. When the laser pulse hits the electrodes, it ionizes some of the electrode surface, due to thermionic emission and avalanche breakdown. The resulting electrons are accelerated by the strong electric field between the electrodes, resulting in avalanche ionization of the gas. A highly conducting plasma fills the gap between the two electrodes, connecting them electrically.

If the spark gap is optimized, it will switch on electrically a very short time after the arrival of the laser pulse. The delay time will be reduced if the laser pulse provides a larger number of initial electrons. This will happen if the laser is focused to a small spot on the surface of one electrode, rather than being focused at a point above the electrode surface. Also, more initial electrons will of course be created by higher power laser pulses. The delay time has been found to vary as $\exp(-P/P_o)$ when the laser power is varied.[9,10] This exponential dependence results from the exponential growth of the number of free electrons as the plasma expands to fill the space between the electrodes. Delay times less than 1 nsec have been reported for laser pulse energies of 10 mJ.

The delay time is also strongly affected by the voltage V between the two electrodes. The fastest delay times require that V be $> 0.9\ V_b$ where V_b is the static breakdown threshold. In fact, experiments show that the delay time increases by about a factor of 10 if V is reduced from 0.9 V_b to 0.6 V_b.[8,10]

Our laser-triggered spark gap is of the design of Alcock et al.[9] Electrically, it has a 50 Ω coaxial geometry. The two electrodes are stainless steel disks. The front electrode (E-1) has a 2 mm diameter hole in it, through which the laser light is focused onto the surface of the second electrode (E-2). The space between the electrodes is filled with Argon gas, which is known to produce low jitter in the spark gap delay times.[8] The rear electrode is held in a threaded sleave so that the distance between the two electrodes can be varied. The sleave is sealed with an o-ring so that the Argon won't leak out.

In our spark gap, the leakage rate of the Argon was quite low. We used a pressure of 100 lb./in^2, which we monitored with a pressure gauge permanently installed on the spark gap. The change in pressure was negligible over periods of up to 1 month if the spark gap were properly assembled. We used a bias voltage of 6 kV, and an electrode spacing of about 2 mm. The light was focused just at the surface of the electrode E2 using the 2 cm lens. This focusing adjustment was quite critical to obtain low delay time and low jitter. Since we had about 200 μJ per mode-locked pulse, the energy density in the focus reached $200\ \mu J/(\pi \times (10^{-3}\ cm)^2) \cong 200\ J/cm^2$, and the power density reached about 200 GW/cm^2. This resulted in good low jitter triggering of the spark gap. After a few weeks of use, the electrode surface of E-1 would become pitted, resulting in less reproducible operation. When this happened, we would replace this electrode.

When the spark gap started to conduct, a square voltage pulse would travel along the coaxial line to the Pockels cell. This coaxial line was terminated at the Pockels cell, to avoid reflections. The length of the voltage pulse was determined by the length of the delay line ℓ between the 1 MΩ resistor and the spark gap. The pulse arriving at the Pockels cell had a voltage V/2 and a duration 2ℓ. We normally used ℓ = 2.5 nsec and $V/2 = V_{1/2}$ where $V_{1/2}$ = 3kV was the half-wave voltage of our Pockels cell. Because of the long charging time (RC >> 1 μsec) of the spark gap, it would fire only once per mode-locked train.

By adjusting the length of the cable between the spark gap and the Pockels cell, the Pockels cell would switch the polarization of only one single mode-locked pulse. This single pulse would pass through P2, and go on to the rest of the experiment. The neutral density filters F were adjusted so that the spark gap triggered just before the peak of the mode-locked train. Then one of the largest mode-locked pulses would be switched out by the Pockels cell. In actual use, we found this system to be a reliable source of single 1 nsec long ruby laser pulses.

References

1. A. J. DeMaria, W. H. Glenn, Jr., M. J. Brienza, and M. E. Mack, Proc. IEEE 57, 2 (1969).
2. P. W. Smith, Proc. IEEE 58, 1342 (1970).
3. M. A. Duguay, J. W. Hansen, and S. L. Shapiro, IEEE J. Quant. Electron. QE-6, 725 (1970).
4. R. C. Greenhow and A. J. Schmidt, Adv. Quant. Electron. 2, 157 (1974).
5. C. V. Shank and E. P. Ippen in Dye Lasers, ed. F. P. Schäfer, Springer-Verlag (1973).
6. E. P. Ippen and C. V. Shank , Appl. Phys. Lett. 27, 488 (1975).
7. A. H. Guenther and J. R. Bettis, Proc. IEEE 59, 689 (1971).
8. F. Deutsch, Brit. J. Appl. Phys., Ser 2, 1, 1711 (1968).
9. A. J. Alcock, M. C. Richardson, and K. Leopold, Rev. Sci. Instrum. 41, 1028 (1970).
10. K. Schildbach and D. Basting, Rev. Sci. Instrum. 45, 1015 (1974).

FIGURE CAPTIONS

Fig. 1. Ruby laser with pulse switching Pockels cell. M-1, 99% dielectric mirror; M-2, 50% dielectric mirror; A-1, A-2 aperatures; P-1, P-2, Glan polarizers; D, ITT fast photodiode; B, beam splitter; W, spark gap window; E-1, E-2, spark gap electrodes; G, pressure gauge; F, neutral density filters.

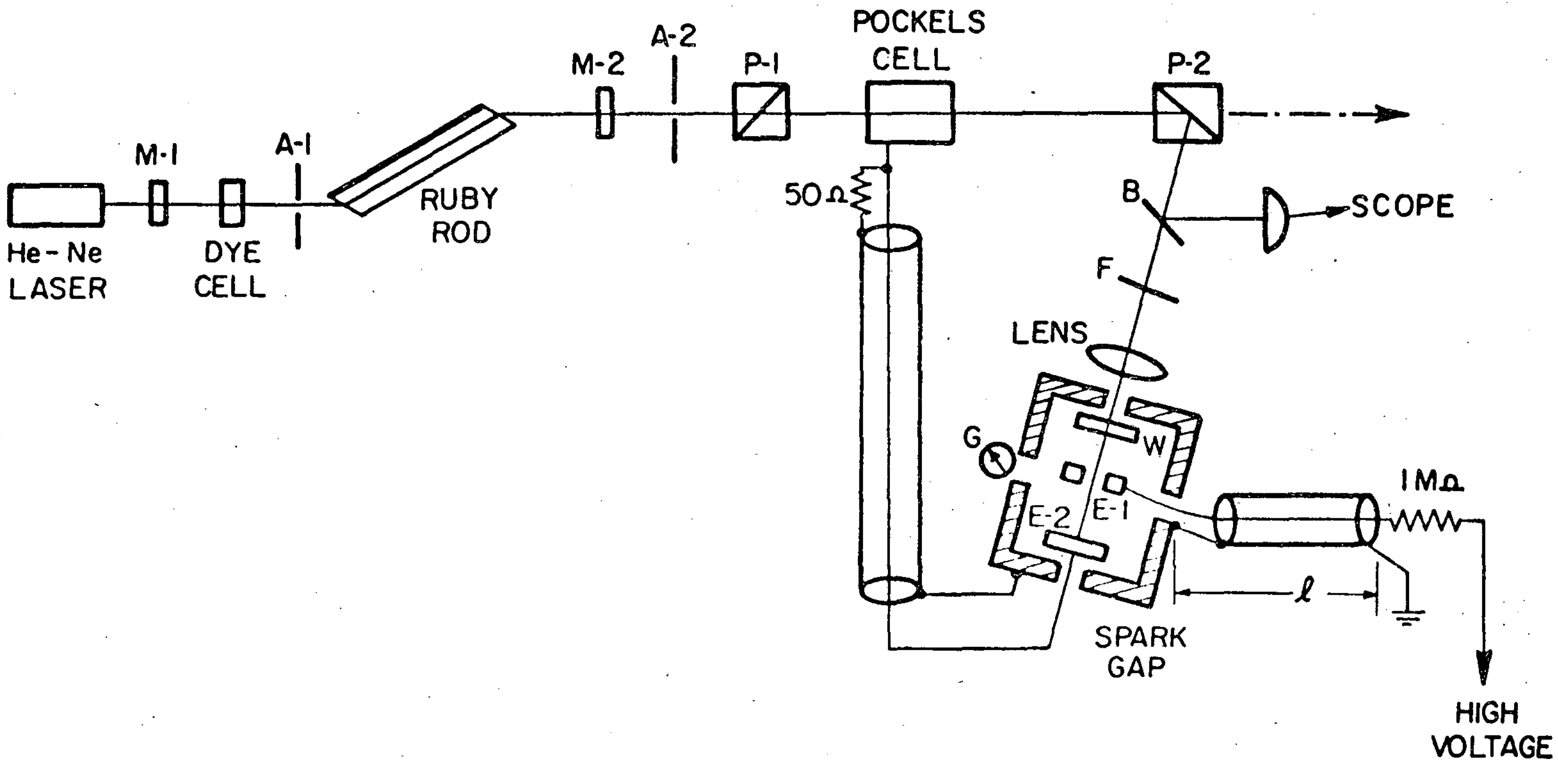

XBL 7611-7778

Fig. 1

ACKNOWLEDGEMENTS

I would like to thank the following people for their contributions to this work:

Professor Y.R. Shen, for his guidance and encouragement during the entire course of my research;

Professor George Wong, for introducing me to the study of nonlinear optics in liquid crystals;

Dr. Nabil Amer and Don Bethune, for sharing their enthusiasm and insight with me;

And my wife, Krista, for helping me throughout these years with her understanding and her love.

This work was performed under the auspices of the National Science Foundation and the Energy Research and Development Administration.

TECHNICAL INFORMATION DIVISION
LAWRENCE BERKELEY LABORATORY
UNIVERSITY OF CALIFORNIA
BERKELEY, CALIFORNIA 94720